PTB bericht
Wissenschaftliche Veröffentlichungen

Diss-27
März 2026

Dissertation

Melina Filzinger

Searching for variations of fundamental constants and ultralight dark matter with optical clocks

ISSN 2941-1297
ISBN 978-3-944659-59-6

DOI 10.7795/110.20260227

Melina Filzinger

Searching for variations of fundamental constants and ultralight dark matter with optical clocks

Dissertation

PTB-Diss- 27

Braunschweig, 02. März 2026

ISSN 2751-6598
ISBN 978-3-944659-59-6

DOI 10.7795/110.20260227

Empfohlene Zitierweise/recommended citation

Filzinger, M., 2026. *Searching for variations of fundamental constants and ultralight dark matter with optical clocks*. Dissertation, Gottfried Wilhelm Leibniz Universität Hannover. Braunschweig: Physikalisch-Technische Bundesanstalt. PTB-Bericht Diss-27. ISBN 978-3-944659-59-6. Verfügbar unter: https://doi.org/10.7795/110.20260227

Herausgeber:
Physikalisch-Technische Bundesanstalt
ISNI: 0000 0001 2186 1887

Presse und Öffentlichkeitsarbeit

Bundesallee 100
38116 Braunschweig

Telefon: (05 31) 592-93 21
Telefax: (05 31) 592-92 92
www.ptb.de

Searching for variations of fundamental constants and ultralight dark matter with optical clocks

Von der Fakultät für Mathematik und Physik
der Gottfried Wilhelm Leibniz Universität Hannover

zur Erlangung des Grades
Doktorin der Naturwissenschaften
Dr. rer. nat.

genehmigte Dissertation von

Melina Filzinger, M.Sc.

2026

https://doi.org/10.7795/110.20260227

Referent: Priv. Doz. Dr. Ekkehard Peik
Korreferent: Prof. Dr. Piet O. Schmidt
Korreferentin: Prof. Dr. Tracy Northup

Tag der Promotion: 14.11.2025

https://doi.org/10.7795/110.20260227

Abstract This thesis reports on frequency comparisons with optical clocks based on trapped ions, and their application to probing variations of fundamental constants, with a focus on searches for ultralight dark matter (UDM). The work was carried out at the Physikalisch-Technische Bundesanstalt (PTB).

An existing optical clock based on a single $^{171}Yb^+$ ion is operated with high availability over several years. Two atomic transitions are probed in an interleaved fashion: An electric octupole (E3) transition, which is highly sensitive to possible variations of the fine-structure constant, and an electric quadrupole (E2) transition. Including the resulting measurement data with that previously obtained in our group further improves the best constraints on a linear drift of the fine-structure constant α to $(1/\alpha)(\mathrm{d}\alpha/\mathrm{d}t) = 1.8(2.5) \times 10^{-19}/\mathrm{yr}$, and its coupling to the gravitational potential Φ of the sun to $(c^2/\alpha)(\mathrm{d}\alpha/\mathrm{d}\Phi) = -2.4(3.0) \times 10^{-9}$, reducing uncertainties by about a factor of four. The same data, along with that from a comparison between the $^{171}Yb^+$ E3 clock and a Sr lattice clock, is analysed for the oscillatory signatures associated with small hypothetical couplings between UDM and normal matter. Leveraging the high α-sensitivity of both frequency ratios, more than an order-of-magnitude improvement in limits on a scalar UDM coupling to photons is achieved over a wide range of dark matter masses. UDM couplings to the nuclear sector are investigated with optical clocks for the first time, by considering the effect an oscillating nuclear charge radius would have on the E3/E2 frequency ratio. It is further demonstrated that space- and time-separated clock comparisons provide sensitivity to dark matter even for oscillators with identical sensitivities to fundamental constants, while also offering access to unique dark matter signatures and complementary UDM couplings.

A new dual-species apparatus for combining $^{171}Yb^+$ and $^{88}Sr^+$ ions enables the realization of a multi-ion clock based on the $^2S_{1/2} \rightarrow {}^2D_{5/2}$ transition in $^{88}Sr^+$ with up to ten ions. A fractional systematic uncertainty of 5.3×10^{-19} is obtained for the multi-ion clock, comparable to the current best single-ion clocks. A frequency comparison between the new optical clock based on $^{88}Sr^+$ and the single-ion $^{171}Yb^+$ clock operating on the $^2S_{1/2}(F = 0) \rightarrow {}^2F_{7/2}(F = 3)$ E3 transition yields an unperturbed frequency ratio of 0.6926711632159660399(20). With a fractional uncertainty of 2.9×10^{-18}, this is the most accurate determination of any physical constant to date. The data obtained with multiple $^{88}Sr^+$ ions is compatible with that obtained using a single $^{88}Sr^+$ ion, but offers a significantly improved instability. This establishes multi-ion clocks as a robust platform for next-generation tests of fundamental physics.

https://doi.org/10.7795/110.20260227

https://doi.org/10.7795/110.20260227

Publications

This thesis is based in part on the following manuscripts and publications:

- M. Filzinger, S. Dörscher, R. Lange, J. Klose, M. Steinel, E. Benkler, E. Peik, C. Lisdat, N. Huntemann: *Improved limits on the coupling of ultralight bosonic dark matter to photons from optical atomic clock comparisons*, Phys. Rev. Lett. **130**, 253001 (2023).
- A. Banerjee, D. Budker, M. Filzinger, N. Huntemann, G. Paz, G. Perez, S. Porsev, M. Safronova: *Oscillating nuclear charge radii as sensors for ultralight dark matter*, Phys. Rev. Lett. **135**, 223001 (2025).
- M. Filzinger, A. R. Caddell, D. Jani, M. Steinel, L. Giani, N. Huntemann, B. M. Roberts: *Ultralight Dark Matter Search with Space-Time Separated Atomic Clocks and Cavities*, Phys. Rev. Lett. **134**, 031001 (2025).
- M. Filzinger, et al.: *A multi-ion optical clock with a* 5×10^{-19} *uncertainty*, manuscript in preparation.

A full list of publications is provided at the end of this document.

https://doi.org/10.7795/110.20260227

https://doi.org/10.7795/110.20260227

Contents

https://doi.org/10.7795/110.20260227

https://doi.org/10.7795/110.20260227

1 Introduction

This work presents high-precision optical frequency comparisons and their use in searches for variations of fundamental constants. The motivation behind this approach is explained in section 1.1, followed by a brief introduction to the experimental platform, namely optical clocks based on trapped ions, in section 1.2. An overview over the results in this thesis can be found in section 1.3.

1.1 Motivation

Fundamental constants are deeply embedded into the formalism we use to describe nature. At the same time, they remain elusive: While their values can be measured, they – by definition – cannot be predicted from any more fundamental principles. What is considered a *fundamental* constant depends on what is considered a fundamental theory. For example, new constants may be added as new phenomena are discovered, or their number might be reduced if it is found that two distinct phenomena can be described by a common underlying theory. In this sense, what we consider fundamental constants is a reflection of our understanding of physics, and its limitations [1, 2].

This work focuses on experimental searches for variations of fundamental constants. While the term "variation of constants" is an obvious oxymoron, it may be understood as shorthand for the fact that observing a variation of a parameter that was previously considered constant indicates the need for *new physics*, a more fundamental theory that includes the observed dynamics. This makes searches for the variation of fundamental constants important tests of the theories we are currently using to describe nature. Even if such an experimental search finds no variation of a constant, it yields information on the domain of validity of our current most fundamental descriptions of nature, and constrains new theories. A more in-depth discussion on the role of constants in fundamental physics can be found for example in [3].

https://doi.org/10.7795/110.20260227

Currently, our best understanding of nature has two main ingredients: general relativity describes gravity, and the standard model of particle physics categorizes the known particles and describes their other interactions. Both of these are extremely well-tested experimentally across a wide range of different length scales [4–8]. However, there are strong indications that these descriptions are incomplete. One striking example is the fact that many independent observations point towards the *majority* of matter in our universe being so-called "dark" matter. This elusive type of matter owes its name to the fact that so far no interactions – besides gravity – between "normal" matter and dark matter have been found. The nature of dark matter cannot be explained by any of the particles in the standard model, at least within our current understanding of physics. Some approaches towards solving this mystery are associated with temporal variations of what are currently considered fundamental constants [9, 10]. Searches for such signatures of dark matter will be the focus in chapter 3 of this thesis.

To search for the variation of fundamental constants experimentally, we need to perform measurements that are sensitive to their values. Here, dimensionless constants play an important role, since their values are independent of the chosen units of measurements. It was realized as early as 1956 that theories predicting a variation of the fine-structure constant would lead to a variation of atomic spectra [11], which can be tested experimentally. Broadly speaking, there are two main approaches to the search for signatures of the variations of fundamental constants in atomic spectra: Astrophysical observations are used to search for variations on a cosmological time scale, while precision laboratory experiments aim at testing for variations during the time spanned by the measurements [12–15]. This work focuses on the latter approach (see [16] for a review), and more specifically on measurements involving optical clocks based on trapped ions.

Optical atomic clocks are the most accurate measurement instruments developed to date, with several systems now featuring fractional systematic uncertainties on the order of 1×10^{-18} [17–22], which makes them well-suited to investigate tiny, previously unnoticed effects. Optical clocks based on trapped ions offer a particularly high degree of control, as a single, trapped ion in vacuum closely resembles the ideal of an unperturbed reference oscillator. Recently, trapped ion optical clocks have even reached systematic uncertainties in the mid-10^{-19} range [23, 24]. However, the amount of information that can be obtained from a single ion in a given time is fundamentally limited by quantum projection noise, often making long measurement times necessary. To overcome this limitation, chapter 5 demonstrates clock operation

https://doi.org/10.7795/110.20260227

with up to 10 ions, and shows that this approach reduces measurement times without sacrificing precision compared to the best single-ion clocks.

The unparalleled precision of optical atomic clocks can be combined with the use of atomic transitions that feature high sensitivities to possible variations of a specific constant. A particular focus in this thesis will be on utilizing their sensitivities to changes of the fine-structure constant α, which depend on relativistic contributions to the transition energies [25]. The sensitivity of a specific transition frequency to small fractional changes of the fine-structure constant can be calculated numerically with relativistic N-body calculations [26, 27]. The ratio of two optical atomic frequencies ν_1 and ν_2 can magnify small fractional changes of the fine-structure constant according to

$$\frac{\Delta(\nu_1/\nu_2)}{\nu_1/\nu_2} = -\Delta K_\alpha \frac{\Delta\alpha}{\alpha}\,, \tag{1.1}$$

for a suitable choice of transitions, such that the magnitude of their differential sensitivity ΔK_α to changes of α is larger than one. This magnification is particularly large for many frequency ratios involving optical clocks based on $^{171}\mathrm{Yb}^+$, which as shown in chapter 2, makes this species a compelling choice for improved searches for variations of the fine-structure constant.

Throughout this thesis, the sensitivities of optical transition frequencies to the variations of constants and the experimental realizations of these transition frequencies in optical clocks come together to enable improved searches for signatures of new physics. To this end, it's helpful to take a brief look at the basic principles behind optical atomic clocks, and their relevant properties.

1.2 Optical clocks based on trapped ions

The basic principle of an optical atomic clock is illustrated in Figure 1.1: A laser is used to periodically interrogate a narrow atomic transition, often called the clock transition. The laser is pre-stabilized to an optical cavity in order to reduce its linewidth. This allows for longer coherent interrogation times on the atomic transition, corresponding to an increased frequency resolution. Based on the interrogation of the atom(s), a discriminator signal is generated that is fed back to the laser for closed-loop control of its frequency. This way, the laser is steered to reproduce the characteristic frequency of the atomic transition.

https://doi.org/10.7795/110.20260227

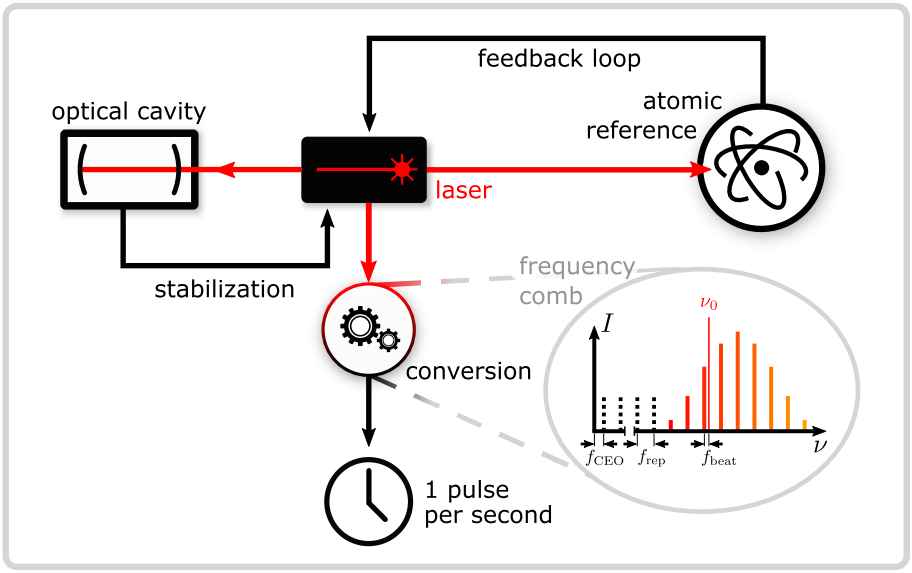

Figure 1.1: Basic principle of an optical atomic clock. Figure adapted from [30].

As optical signals cannot directly be processed electronically, a frequency comb acts as a clockwork [28, 29], for example allowing one to produce a one-pulse-per-second "clock" output derived from the laser radiation. The frequency comb provides a discrete spectrum of equally spaced frequencies in the optical regime (the comb "teeth"). The frequencies have a spacing f_{rep} and the lowest frequency has an offset of f_{CEO} to zero. Measuring the beat frequency f_{beat} between the laser frequency ν_0 and the mth comb tooth, the frequency of the laser can be extracted according to

$$\nu_0 = f_{\mathrm{CEO}} + m f_{\mathrm{rep}} + f_{\mathrm{beat}} \tag{1.2}$$

from the electronically processable radio-frequency signals.

Any high-performance atomic clock is characterized by two main properties: its systematic uncertainty and its frequency instability. The systematic uncertainty describes how well the unperturbed atomic transition frequency can be realized. Since the completely unperturbed atom or ion at rest is an idealization, the measured frequency of the local oscillator can never perfectly reproduce the shift-free atomic transition frequency. Frequency shifts affecting an atomic clock need to be assessed and corrected for. Together with their uncertainties, all relevant frequency shifts are summarized in an uncertainty budget that provides an estimate for the clock's accuracy.

The extremely low fractional systematic uncertainties of optical clocks are partially due to their large base frequencies: Frequency shifts that are independent of the

https://doi.org/10.7795/110.20260227

transition frequency naturally contribute a smaller fractional amount relative to a frequency on the order of hundreds of THz, compared to e.g. frequencies in the GHz range, which are typical for microwave atomic clocks. On the other hand, there are frequency shifts that *do* scale with the transition frequency, such as the Doppler shift, which results from the relative motion of the atomic reference with respect to the interrogating radiation. Technological advances enabling a high level of control over external and internal degrees of freedom in atoms and ions, such as laser cooling and state detection, were therefore crucial for the development of high-precision optical clocks [31].

Measurements of a clock's absolute frequency rely on a comparison with a clock that realizes the SI unit second. The current definition of the second is based on an atomic hyperfine transition in the microwave regime, and due to technical limitations of microwave atomic clocks, the best realizations of the second [32–34] are limited to systematic uncertainties of about 1×10^{-16}. As optical clocks have now reached systematic uncertainties more than two orders of magnitude below this level, a future redefinition of the second will likely be based one one or several optical transitions [35]. In the meantime, it is particularly attractive to measure dimensionless frequency ratios of optical clocks, thereby circumventing the limitations currently imposed on absolute frequency measurements.

Next to its systematic uncertainty, the second important property of an atomic clock is its frequency instability. It can be obtained from a series of successive measurements and is typically characterized by the Allan deviation [36]

$$\sigma_y(\tau) = \sqrt{\frac{1}{2M-1}\sum_{k=1}^{M-1}(y_{k+1}-y_k)^2}\,, \tag{1.3}$$

where y_i are measurement results that have been averaged over the duration τ, with the total dataset consisting of M such measurement results. The behavior of the Allan deviation can indicate the dominant scaling of the measurement noise. White frequency noise (frequency-independent power spectrum) results in a $\sigma_y(\tau) \propto 1/\sqrt{\tau}$ scaling. For an ideal optical atomic clock, this is the typical noise observed on timescales larger than the time constant associated with the clock's feedback loop.

Uncertainty and instability are connected insofar as a clock's instability dictates the averaging time necessary to achieve a certain statistical uncertainty, for example equal to its systematic uncertainty, in a measurement. The systematic uncertainty

https://doi.org/10.7795/110.20260227

sets an upper bound for a clock's expected long-term stability, or reproducibility, if all relevant effects have been considered correctly. If effects that remain constant over time contribute to the systematic uncertainty, for example due to limited knowledge of atomic parameters, the reproducibility is even better than the systematic uncertainty.

A single trapped ion in ultrahigh vacuum is a conceptually simple system that closely resembles the ideal of an unperturbed reference. Due to their electric charge, ions can be trapped in radiofrequency traps that provide confinement around a field-free saddle point of an oscillating potential, ensuring that the transition frequency is only minimally perturbed by the trap. Laser cooling enables reaching the so-called Lamb–Dicke regime, where the ion's motion is constrained to a region smaller than the laser wavelength used for clock interrogation. In this case, the resulting spectroscopic line is free of the linear Doppler shift. More information on trapped ions and associated experimental techniques can for example be found in [37, 38].

Ideally, the instability of a trapped-ion optical clock is limited by quantum projection noise, leading to a scaling of [39]

$$\sigma_y(\tau) = \frac{\kappa}{C}\frac{1}{\nu T}\sqrt{\frac{T+T_d}{N\tau}}\,. \tag{1.4}$$

Here, κ is a constant of order unity that depends on the details of the interrogation scheme, C denotes the contrast, ν the transition frequency, T the coherent interrogation time, T_d the dead time spent for example on state preparation and detection, and N the number of uncorrelated atoms interrogated simultaneously.

The achievable coherent interrogation time T is limited either by the radiative lifetime of the transition's excited state, or by technical limitations such as finite laser coherence. Since a single ion remains trapped for many interrogations, there is typically no dead time associated with ion loading. Efficient state preparation and detection enable reaching a dead time T_d well below the coherent interrogation time T, such that it does not contribute significantly to the cycle time $T + T_d$. Simultaneously interrogating multiple trapped ions instead of just a single one offers an avenue towards improving the instability of an ion clock: Ideally, one can gain the same amount of information that is usually obtained through N interrogations of a single ion, via a single interrogation of N ions. This approach is pursued in chapter 5 of this thesis.

https://doi.org/10.7795/110.20260227

1.3 Overview over results in this work

The work presented here sits at the intersection of fundamental physics and frequency metrology. While the next two chapters steer towards the former, the two chapters after that focus on advancing optical clocks based on trapped $^{171}Yb^+$ and $^{88}Sr^+$ ions further, which paves the path towards even better searches for the variation of constants. The remainder of this thesis is structured as follows:

Chapter 2: "$^{171}Yb^+$ as a sensor for variations of the fine structure constant" introduces key properties of the $^{171}Yb^+$ ion, with a focus on the two relevant optical reference transitions. Experimental techniques for measuring the ratio of the two transition frequencies, which is highly sensitive to possible variations of the fine-structure constant, are introduced. The key results are improved limits on local position invariance from long-term measurements of this optical frequency ratio, which can also be found in the supplemental material of [40].

Chapter 3: "Searching for ultralight dark matter" discusses different aspects of ultralight dark matter searches with optical frequency comparisons. Ultralight dark matter describes a well-motivated class of dark matter models consisting of bosons that are so light they behave like a classical coherent wave. The chapter starts out with an introduction to relevant aspects of dark matter, and particularly ultralight dark matter. Since small hypothetical couplings between this type of dark matter and the standard model content are associated with oscillations of fundamental constants, measurement data is analysed for such oscillations, considering the sensitivities of the measurements to the fundamental constants. The high fine-structure sensitivity of the $^2S_{1/2} \rightarrow {}^2F_{7/2}$ electric-octupole transition in $^{171}Yb^+$ is leveraged in two optical clock comparisons that yield improved bounds on the strength of an ultralight dark matter coupling to photons. Most of these results can also be found in [40], though additional details are provided here. Additionally, the fact that optical atomic clock comparisons are sensitive also to couplings of ultralight dark matter to quarks and gluons is considered and utilized for the first time, using $^{171}Yb^+$ as an example. Most of the content of this section is also part of the publication [41]. Furthermore, the effects of space- and time-separation in optical frequency comparisons are investigated in an approach that is complementary to the analysis of typical co-located frequency comparisons and retains sensitivity to dark matter couplings even for a comparison of equal oscillators. These results are also published in [42].

https://doi.org/10.7795/110.20260227

Chapter 4: "A new optical clock experiment for $^{171}Yb^+$ and $^{88}Sr^+$ ions" describes the setup and characterization of a new experimental apparatus that combines $^{88}Sr^+$ and $^{171}Yb^+$ ions. The motivation behind combining these two ion species towards improved searches for the variation of fundamental constants is introduced. Key components are described and characterized, with a focus on properties that are relevant for the operation of the system as an optical clock.

Chapter 5: "An optical clock based on multiple $^{88}Sr^+$ ions" contains the first results obtained with the new experimental apparatus. Some of the work presented in this chapter builds upon our previous results obtained with a different apparatus, reported in [43]. An optical clock based on the $^2S_{1/2} \rightarrow {}^2D_{5/2}$ transition in $^{88}Sr^+$ is established, and clock operation with up to 10 ions is achieved. Systematic effects associated with clock operation based on multiple ions are analysed. The fractional systematic uncertainty of the multi-ion clock is evaluated as 5.3×10^{-19}. The results of an optical frequency comparison between this clock and the $^{171}Yb^+$ single-ion clock introduced in chapter 2 are presented. The content of this chapter is also in preparation for a separate publication, titled *A multi-ion optical clock with a* 5×10^{-19} *uncertainty.*

Chapter 6 summarizes this thesis and discusses implications of the results for future tests of fundamental physics.

https://doi.org/10.7795/110.20260227

2 ^{171}Yb$^+$ as a sensor for variations of the fine structure constant

Experiments with trapped ^{171}Yb$^+$ have been pursued since 1982 [44], and at PTB since the beginning of the 1990s. At first, the focus was precision microwave spectroscopy of the ground state hyperfine transition [45, 46], but with the advent of laser cooling and spectroscopy, its potential as a reference for an optical clock came into focus [47, 48]. This chapter will introduce the relevant atomic properties of ^{171}Yb$^+$ as well as the key experimental components and techniques we employ to realize optical clocks based on the $^2S_{1/2}(F = 0) \rightarrow {}^2D_{3/2}(F = 2)$ electric quadrupole and $^2S_{1/2}(F = 0) \rightarrow {}^2F_{7/2}(F = 3)$ electric octupole transitions with a single trapped ion to measure the ratio of their frequencies. Combining measurement data obtained in this fashion with earlier measurements of the same frequency ratio performed in our group, we are able to improve the previously obtained limits on slow variations of the fine-structure constant, which may be considered a test of local position invariance.

2.1 The ^{171}Yb$^+$ ion

There are many reasons that make ^{171}Yb$^+$ a compelling choice for building an optical clock. Its relatively large mass leads to low ion velocities for a given temperature, corresponding to low motional frequency shifts. The ^{171}Yb$^+$ isotope features a nuclear spin of 1/2, which results in a simple hyperfine structure and transitions between $m_F = 0$ Zeeman sublevels that are insensitive to magnetic field fluctuations at first order. ^{171}Yb$^+$ ions can be stored in a Paul trap for long periods of time, and we typically keep a single ion for several months. In case of a chemical reaction

https://doi.org/10.7795/110.20260227

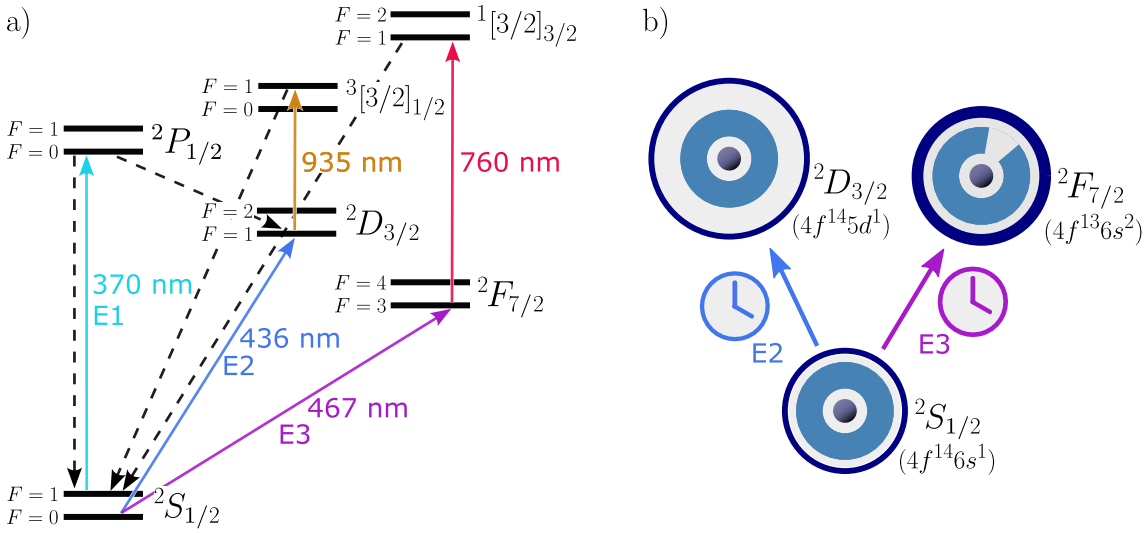

Figure 2.1: Relevant level scheme of $^{171}Yb^{+}$. a) An electric dipole (E1) transition at 370 nm is used for Doppler cooling and detection. An electric quadrupole (E2) transition at 436 nm and an electric octupole (E3) transition at 467 nm are used as reference transitions for optical clocks. A repump transition at 935 nm clears out the E2 excited state, also facilitating closed-cycle Doppler cooling. An electric quadrupole repump transition at 760 nm is used to depopulate the E3 excited state. b) Cartoon picture of electron orbitals involved in the two clock transitions. While in the E2 transition a valence electron is excited, in the E3 transition a hole is formed in the low-lying f-shell, close to the heavy nucleus. The different character of the excited states can yield an intuitive understanding of the very different properties of the two transitions.

with a background-gas molecule, the resulting molecule is photodissociated with the cooling or clock lasers.

Figure 2.1 provides an overview over the relevant optical transitions in $^{171}Yb^{+}$. An electric dipole transition at 370 nm with a natural linewidth of $\gamma = 2\pi \times 19.60(5)$ MHz [49] allows for Doppler cooling and state detection at an accessible wavelength. The hyperfine structure results in coherent population trapping at low magnetic fields [50], and we typically use magnetic fields of a few hundred µT during detection. The ion offers three narrow optical transitions originating from the ground state, which may each act as the reference transition of an optical clock: Two electric quadrupole (E2) transitions at 411 nm and 436 nm, as well as an electric octupole (E3) transition at 467 nm. Since we only employ the latter two in our lab, the $^2S_{1/2} \rightarrow {}^2D_{5/2}$ transition at 411 nm is not depicted, and electric quadrupole, or E2, transition always refers to the $^2S_{1/2} \rightarrow {}^2D_{3/2}$ transition in the following. A repump transition at 935 nm is used to clear out the $^2D_{3/2}$ state after excitation, and to

https://doi.org/10.7795/110.20260227

	$^2S_{1/2} \leftrightarrow {}^2D_{3/2}$	$^2S_{1/2} \leftrightarrow {}^2F_{7/2}$
Type	Electric quadrupole	Electric octupole
Excited state lifetime	53(2) ms [51]	1.58(8) yrs [52]
Quadrupole moment	$1.95(1)\, ea_0^2$ [56]	$-0.0297(5)\, ea_0^2$ [56]
2nd-order Zeeman sensitivity	$52.10(2)\,\mathrm{mHz/\mu T^2}$ [57]	$-2.082(2)\,\mathrm{mHz/\mu T^2}$ [30]
α-sensitivity	1.00 [27]	−5.95 [27]

Table 2.1: Selected properties of the employed optical reference transitions in $^{171}Yb^{+}$.

facilitate closed-cycle photon scattering during detection. An electric quadrupole repump transition at 760 nm is used to depopulate the E3 excited state. All employed transitions are at experimentally convenient wavelengths at which diode lasers have been commercially available for decades.

The two employed transitions in $^{171}Yb^{+}$ have different characteristics owing to their different multiplicity: The E2 transition has an excited state lifetime of 53(2) ms [51], corresponding to a natural linewidth of 3 Hz, while the highly forbidden E3 transition has a natural lifetime of 1.58(8) years [52], corresponding to a nHz natural linewidth. For realizing an optical clock, the intermediate E2 excited state lifetime limits the coherent interrogation time and ultimately the achievable instability in the case of a single ion. This is not the case for a clock based on the E3 transition, where the coherent interrogation time is solely determined by technical limitations, such as finite laser coherence or ion heating. However, the extremely narrow natural linewidth also brings experimental challenges: A high intensity of hundreds of $\mathrm{W/cm^2}$ is needed to drive Rabi pulses of tens of ms, resulting in AC Stark shifts of well above 100 Hz. Experimental techniques have been developed for controlling this shift: Specific pulse sequences such as hyper-Ramsey spectroscopy [53] and autobalanced Ramsey spectroscopy [54], as well as the excitation in the intensity minimum of a vortex beam [55] do offer shift suppression and immunity to intensity fluctuations, but also add experimental complexity.

The excited state electronic structures of the E2 and E3 transitions differ significantly: They are characterized by a single $6d$ electron for the $^2D_{3/2}$ state and a single hole in the otherwise filled $4f$ shell for the $^2F_{7/2}$ state. Consequently, the excited state lifetime is not the only difference between the two transitions, with some relevant properties summarized in Table 2.1. The E2 transition is generally more sensitive to external perturbations. The known relative sensitivities between the transitions can be used to calculate time-resolved corrections for a clock operating on the E3 transition based on results from interrogating the E2 transition in the

https://doi.org/10.7795/110.20260227

same ion. Here, the clock operating on the E2 transition might be seen as ancillary to the more stable and accurate clock based on the E3 transition.

The heavy nucleus of $^{171}Yb^{+}$ makes large relativistic contributions to the transition energies plausible. In fact, the E3 transition frequency features a sensitivity of $K_\alpha = -5.95$ to variations of α [27] – the largest in any currently operational optical clock, though higher-sensitivity clocks, for example based on neutral ytterbium [58] are being developed. With a large and opposite-sign sensitivity of $K_\alpha = 1.00$ [27] the E2 transition is a suitable partner for optical frequency comparison with high α-sensitivity.

2.2 The single-ion optical clock experiment Yb1

The experimental apparatus referred to as Yb1 is based on a traditional Paul trap with a ring and two endcap electrodes, located in a quartz glass cell with Brewster-cut windows. The trap has been under vacuum since the mid-1990s, with frequent updates to the surrounding experiment in the subsequent years. A single-layer of mu-metal around the glass cell provides magnetic shielding. To load an ion, atom flux is generated from an oven, and a laser beam at 399 nm is used for photoionization inside the trapping volume. Ion fluorescence is imaged onto either a photomultiplier tube or an EMCCD camera, depending on the setting of a flip mirror. Typically, a single ion remains trapped for several months in this apparatus. Excess micromotion is monitored via the photocorrelation technique, using the photons accumulated for cooling and detection during clock operation. Every few days, the compensation field is adjusted manually by minimizing residual changes of the ion position that are associated with lowering the trap potential. Currently, the system is routinely running on both the E3 and E2 transitions in an interleaved fashion, with about 75% of the combined cycle time spent on the E3 transition, and 25% on the E2 transition. The system is extremely robust, producing valid data at least 80% of the time over months. This high availability, together with its demonstrated long-term stability at the low-10^{-18} level makes the apparatus an invaluable resource and an attractive reference for optical clock comparisons at PTB and beyond.

Just within the past few years, the system has acted as a reference for our newer optical clock setups based on $^{171}Yb^{+}$ and $^{88}Sr^{+}$ ions, as well as the transportable $^{171}Yb^{+}$ optical clock opticlock, and for investigations of the clock transitions in the

https://doi.org/10.7795/110.20260227

$^{173}Yb^+$ isotope in our group. Within PTB, Yb1 has been compared to the In^+-Yb^+ Coulomb crystal clock [21], and acted as a reference for investigations of isotope shifts in Yb^+ [59] and Ca^{14+} [60], as well as for measurements of excited-state magnetic properties in Ca^{14+} [61]. Additionally, the system has contributed to international optical clock comparison campaigns [62].

The systematic uncertainty for Yb1 operating on the E3 transition has previously been evaluated as 2.7×10^{-18} [63], and on the E2 transition as 33×10^{-18} [64].

2.3 Measuring the E3/E2 frequency ratio

The frequency ratio ν_{E3}/ν_{E2} has been measured in our group since 2016. For most of this time, two different experimental setups, each based on a single $^{171}Yb^+$ ion, were used to realize the frequency ratio: Yb1 was mostly acting as the clock based on the E2 transition, while the now decommissioned apparatus Yb2 was realizing ν_{E3}. Since autumn of 2020, the frequency ratio has been realized by the single apparatus Yb1 via the method of *interleaved interrogation*. Here, a single ion is interrogated on both the E3 and E2 transitions in an alternating fashion.

Key components involved in this optical frequency comparison are depicted in Figure 2.2. As described previously in [64], the E2 probe laser frequency is stabilized with fixed ratio $1/R_0$ to that of the E3 probe laser at a frequency comb. The servo running on the E3 transition steers the probe laser directly, while the servo running on the E2 transition steers a local offset Δf_2 via an AOM close to the ion trap, which is recorded and can be used to calculate the frequency ratio via

$$\frac{\nu_{E3}}{\nu_{E2}} = R_0 \left(1 + \frac{\Delta f_2}{\nu_{E2}} + \frac{\Delta\nu_{E2}}{\nu_{E2}} - \frac{\Delta\nu_{E3}}{\nu_{E3}}\right), \tag{2.1}$$

where the systematic frequency corrections $\Delta\nu_{E3}$ and $\Delta\nu_{E2}$ can be obtained from the respective uncertainty budgets. The low-10^{-18} uncertainty of the clock based on the E3 transition is negligible for the frequency ratio, since the clock based on the E2 transition currently has a much higher systematic uncertainty of 33×10^{-18}.

The E3 transition is probed using Rabi-controlled hyper-Ramsey spectroscopy [22] with a dark time of 500 ms, while we use standard Rabi interrogation with 42 ms long pulses for the E2 transition, because of its short 53 ms excited-state lifetime [51]. The E2 transition frequency is averaged over three mutually perpendicular directions of

https://doi.org/10.7795/110.20260227

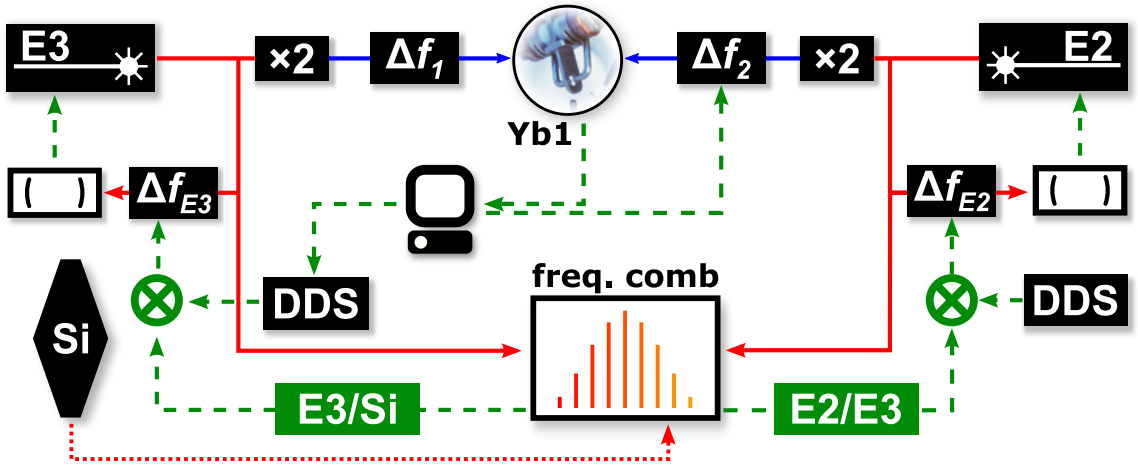

Figure 2.2: Key components in the measurement of $\nu_{\mathrm{E3}}/\nu_{\mathrm{E2}}$ via interleaved interrogation. Optical paths are depicted by red and blue lines; electric signals by dashed green lines. The E3 and E2 clock lasers are stabilized to optical cavities and their light is frequency doubled before being sent to the ion trap. The short-term stability of an ultrastable silicon cavity (Si) [65] is transferred via a frequency comb to the E3 clock laser [66]. The E2 laser frequency is controlled to provide a constant frequency ratio relative to the E3 laser at a frequency comb via the frequency offset Δf_{E2}, thereby inheriting the Si short term stability from the E3 laser. Spectroscopy of the E3 clock transition steers the corresponding laser frequency via direct digital synthesis (DDS) generating the frequency offset Δf_{E3}, while the frequency of the E2 laser is corrected by an additional offset to Δf_2 directly before the ion trap. For simplicity, only one frequency comb is depicted, even though recently two frequency combs are involved in the measurement: one for locking the E3 clock laser to the light from the Si cavity, and a different one for locking of the E2 laser to the E3 laser. Phase-coherent links between the two frequency combs are provided by the light from the Si cavity and the E3 clock laser light. Figure adapted from [64].

the applied magnetic field, which suppresses tensorial shifts such as the quadrupole shift [67]. While we use the first order Zeeman-insensitive $m_F = 0 \rightarrow m_F = 0$ transitions as the basis for both optical clocks, we periodically probe the $m_F = 0 \rightarrow m_F = 2$ component of the E2 transition to determine the magnetic field strength for all three settings using the known linear Zeeman coefficient of $8.388(1)\,\mathrm{kHz}/\mu\mathrm{T}$ [57]. The result is used to calculate a time-resolved correction for the second-order Zeeman shift on the E2 $m_F = 0 \rightarrow m_F = 0$ transition. Similarly, we calculate a dynamical correction of the shift due to black-body radiation based on measurements with resistive temperature sensors. Since most other parameters are kept constant during clock operation, the reproducibility of ν_{E2} is expected to be much smaller than its uncertainty. The dynamic correction of the second-order Zeeman shift leads to a

https://doi.org/10.7795/110.20260227

Effect	$\Delta\nu_{E2}/\nu_{E2}$ [64] (10^{-18})	u_{E2}/ν_{E2} [64] (10^{-18})	r_{E2}/ν_{E2} [64] (10^{-18})	r_{E2}/ν_{E2} (10^{-18})
Blackbody radiation	−495	27	3	3
Quadrupole	0	14	14	1
Second-order Zeeman (rf)	0	10	1	1
Second-order Zeeman (dc)	463	6	6	< 1
Second-order Stark	−2.0	2	2	2
Second-order Doppler	−1.0	1	1	1
Servo	0	1	1	1
Total	−35	33	16	4

Table 2.2: Frequency shifts $\Delta\nu_{E2}$, with corresponding uncertainties u_{E2} and reproducibilities r_{E2} for the single-ion clock Yb1 operating on the E2 transition.

reproducibility of $< 1 \times 10^{-18}$ for this shift. Since the quadrupole shift in our system remains constant over time at the 1×10^{-16} level, and as we suppress this shift by at least a factor of 100 with our averaging scheme [56], we estimate the reproducibility of the remaining quadrupole shift to 1×10^{-18}. We estimate the total fractional reproducibility of ν_{E2} in our system as 4×10^{-18}, a significant improvement over the previously reported value of 16×10^{-18} [64].

Table 2.2 summarizes the uncertainty budget, with past and present contributions to the reproducibility of the Yb1 clock running on the E2 transition. Time-resolved corrections of the second-order Zeeman shift and the quadrupole shift are calculated for the clock running on the E3 transition based on the result from the interrogations of the E2 transition, so that both $\Delta\nu_{E2}$ and $\Delta\nu_{E3}$ may be time-dependent. In practice, the time-resolved corrections of $\Delta\nu_{E3}$ are so small that we have not used them in evaluations of optical frequency ratios to date.

Figure 2.3 shows the Allan deviation of 2.03×10^7 s (235 days) of measurement data of the frequency ratio ν_{E3}/ν_{E2} taken over a period of about 26 months between MJD 59097 (September 5, 2020) and MJD 59900 (November 11, 2022). The fractional measurement instability of $1.0 \times 10^{-14}/\sqrt{\tau(\mathrm{s})}$ is limited by the clock running on the E2 transition. In addition to the limited natural linewidth of this transition, the much longer interrogation on the E3 transition acts as dead time for the clock running on the E2 transition. A more equal duty cycle could be obtained by following each cycle of the clock running on the E3 transition by multiple cycles of the clock running on the E2 transition, however not without sacrificing the instability of the

https://doi.org/10.7795/110.20260227

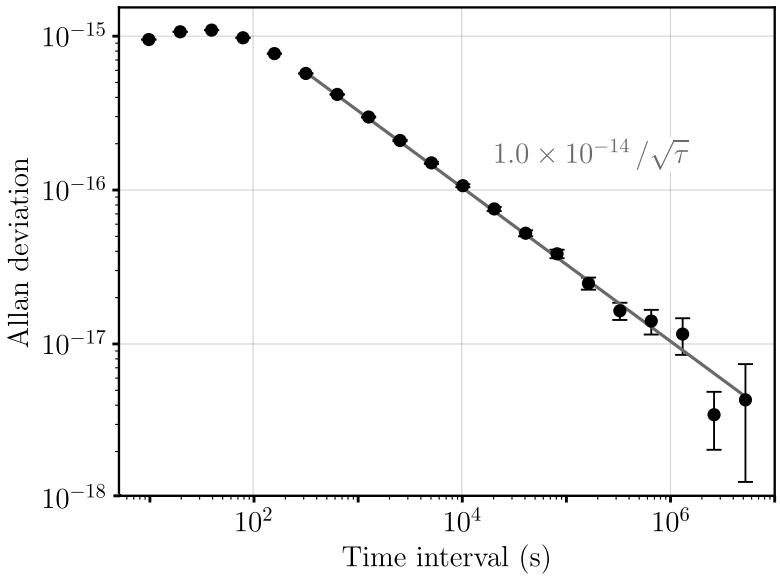

Figure 2.3: Instability of the frequency ratio ν_{E3}/ν_{E2}, as characterized by the Allan deviation. The plot is based on 2.03×10^7 s (or 235 days) of data taken over a period of about 26 months between MJD 59097 (September 5, 2020) and MJD 59900 (November 11, 2022). The solid line is a fit with the $1/\sqrt{\tau}$ scaling expected for white noise. The fractional statistical uncertainty obtained from extrapolating the fit result to the total measurement duration is 2.3×10^{-18}.

clock running on the E3 transition, which is about $1 \times 10^{-15}/\sqrt{\tau(\mathrm{s})}$, as obtained from frequency comparisons with a more stable optical lattice clock [68]. Despite the limited instability of the measurement in its current configuration, Figure 2.3 shows that by accumulating enough data we can reach a low-10^{-18} statistical uncertainty, demonstrating exceptional long-term stability of our measurements of this frequency ratio over an order of magnitude below the systematic uncertainty.

2.4 Improved limits on local position invariance

Local position invariance states that the result of any non-gravitational experiment is independent of the position in space and time [69]. To test this important building block of the Einstein equivalence principle, we can search for variation in precise measurements of optical frequency ratios over extended periods of time. In particular, we can use the large sensitivity of the ratio ν_{E3}/ν_{E2} to potential variations of the fine-structure constant to investigate its constancy. The simplest possible variation would be a linear drift of the fine structure constant over time. Using the annual variation of the Sun's gravitational potential $\Phi(t)$ on Earth due to the ellipticity of

https://doi.org/10.7795/110.20260227

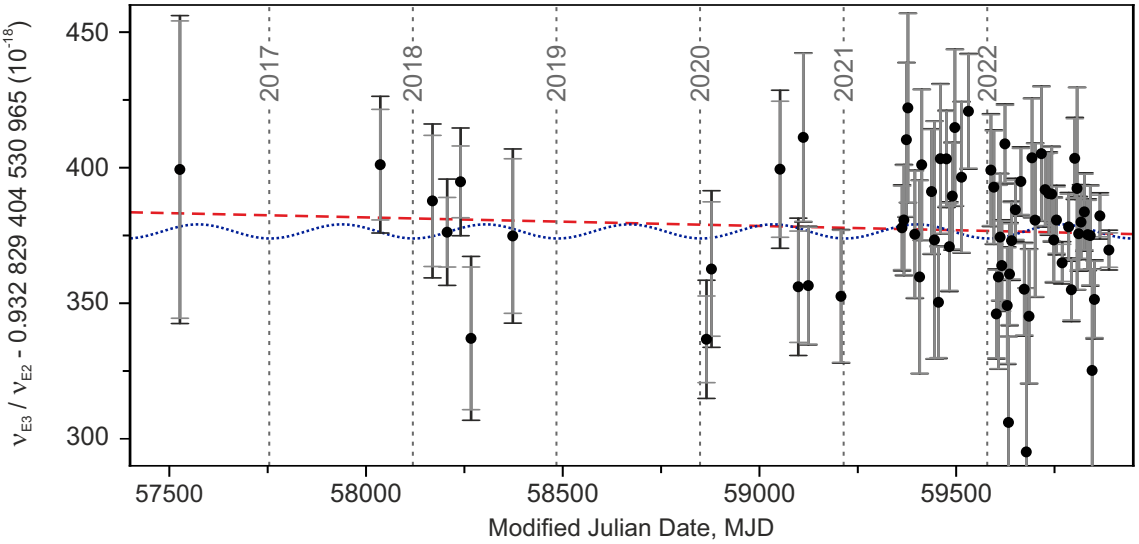

Figure 2.4: Ratio of the frequencies ν_{E3} and ν_{E2} of the E3 and the E2 transition in $^{171}Yb^+$ measured between MJD 57527 (May 19, 2016) and MJD 59900 (November 11, 2022). The gray error bars show the statistical uncertainties. For the black error bars, a fractional uncertainty has been added in quadrature to take into account the reproducibility of systematic shifts over the measurement period. The dashed red line and the dotted blue line are fits to the data in search for a linear temporal drift and a dependence on the gravitational potential, respectively.

the Earth's orbit enables investigation of a possible coupling of α to gravity, which would lead to an oscillation with a period of the anomalistic year (≈ 265.25 days).

Previous optical frequency comparisons of ν_{E3} and ν_{E2} in our group found the strictest limits on a linear temporal variation of the fine-structure constant α and its coupling to the gravitational potential of the sun [64]. Including the new data in the same analysis allows us to further improve these limits. Figure 2.4 shows both the previously published measurement results of the frequency ratio ν_{E3}/ν_{E2} between May 2016 (MJD 57527) and August 2020 (MJD 59081), as well as new measurement data starting from September 2020. The increased amount of data from 2021 and 2022 compared to earlier years is due to increased measurement activity as well as improvements in clock availability during measurements. The dashed red line and the dotted blue line are fits to all data of a linear temporal drift and a sinusoidal modulation with a period of about 365.25 days respectively. Taking into account the statistical uncertainties and reproducibility, the fits result in a reduced χ^2 of 1.2 and 1.1, respectively. We find a linear drift of

$$\frac{1}{\nu_{E3}/\nu_{E2}} \frac{d(\nu_{E3}/\nu_{E2})}{dt} = -1.2(1.8) \times 10^{-18}/\text{yr} \tag{2.2}$$

https://doi.org/10.7795/110.20260227

in our measurements of the frequency ratio $\nu_{\mathrm{E3}}/\nu_{\mathrm{E2}}$, corresponding to

$$\frac{1}{\alpha}\frac{\mathrm{d}\alpha}{\mathrm{d}t} = 1.8(2.5) \times 10^{-19}/\mathrm{yr}\,. \tag{2.3}$$

For a possible coupling to the gravitational potential Φ of the sun, the best fit to all data yields

$$\frac{c^2}{\alpha}\frac{\mathrm{d}\alpha}{\mathrm{d}\Phi} = -2.4(3.0) \times 10^{-9}\,. \tag{2.4}$$

Both values are compatible with zero and improve the previous best limits [64] by about a factor of four in the uncertainty.

Notably, the limits presented above encompass only two possible forms of variation that could be present in the data. It might be worthwhile to also search for other types of variations, especially if they are theoretically well-motivated. In the next chapter, we will see that oscillations of the fine-structure constant may be caused by ultralight dark matter, with the oscillation frequency corresponding to the (unknown) dark matter mass. This motivates searching not just for sinusoidal variations of one specific frequency and phase as above, but for oscillations with all possible frequencies in our recent measurement data of $\nu_{\mathrm{E3}}/\nu_{\mathrm{E2}}$.

https://doi.org/10.7795/110.20260227

3 Searching for ultralight dark matter

The nature of dark matter is one of the biggest open questions in today's physics. While there are many well-documented effects dark matter has on "normal" matter via gravity, non-gravitational interactions with standard model matter remain elusive and are thus likely to be very small. We can search for the effects of such small interactions with precise measurements, for example comparisons of optical atomic clocks, in order to improve our understanding of the nature of dark matter.

This chapter starts out with a brief introduction to dark matter, and particularly ultralight dark matter – consisting of bosons that are so light they behave like a classical coherent wave – following the excellent reviews [70–73] and theses [74, 75]. I will be focusing on simple examples and those dark matter properties that are relevant to the experiments considered here.

Then, section 3.3 presents a dark matter search based on two optical frequency comparisons involving $^{171}Yb^{+}$. By searching for oscillations of fundamental constants with these precision measurements, we investigate small, hypothetical couplings of ultralight dark matter to "normal" (i.e. standard model) matter. Leveraging the large sensitivity of the E3 transition to changes of the fine-structure constant enables us to improve limits on a scalar dark matter coupling to photons by more than an order of magnitude over a wide range of dark matter masses.

Section 3.4 extends the usual way of analyzing optical frequency comparisons for ultralight dark matter couplings by explicitly considering the effect an oscillating nuclear charge radius would have on the E3/E2 optical frequency ratio in $^{171}Yb^{+}$. This enables us to investigate dark matter couplings with the nuclear sector via a comparison of electronic transition frequencies for the first time.

In section 3.5 we consider a dark matter search based on frequency comparisons between oscillators which are far apart – either spatially or temporally – and show

https://doi.org/10.7795/110.20260227

that this approach not only retains dark matter sensitivity for oscillators with equal sensitivity to fundamental constants, but also yields unique dark matter signatures and access to complementary couplings.

Since no dark matter was detected in the scope of this thesis, the key results throughout this chapter will be exclusion plots - limits on the strengths of ultralight dark matter couplings derived from experiment.

3.1 Why do we think there is dark matter?

One of the earliest and arguably the most prominent clue towards the existence of dark matter (DM) came from the measurement of galaxy rotation curves [76, 77] - the rotational velocity v of stars within a galaxy as a function of their distance r from its center. These curves allow to deduce information on the mass distribution within galaxies. For a star orbiting at a radius R larger than the radius containing most of the luminous matter with a total mass M, its' centripetal acceleration is simply given by

$$\frac{v^2}{R} = \frac{G_N M}{R^2}\,. \tag{3.1}$$

One would therefore expect a scaling of $v \propto \sqrt{r}$ outside of the radius containing most luminous matter, if it alone was responsible for the gravitational attraction of the outermost stars in galaxies. Surprisingly, rotation curves are actually found to be mostly flat in this region, i.e. the rotational velocity is largely independent of the distance from the galactic center. This can be explained if the mass distributions of galaxies are dominated by a spherical halo of dark matter extending far beyond the luminous matter: For a total mass $M(R) \propto R$, which could be obtained if the mass distribution is dominated by a dark matter density scaling as $\rho_{DM}(r) \propto 1/r^2$, one indeed obtains v independent of R. However, dark matter is not necessary to explain the "flat" galaxy rotation curves: The observations can also be explained by modified Newtonian dynamics (MOND) theories, which are based on modifying the force of gravitational attraction for very small accelerations [78].

Of course, galaxy rotation curves are not the only type of evidence that point towards the existence of dark matter. On even larger scales, compelling dark matter evidence comes from studies of gravitational lensing effects, i.e. measuring the distortion patterns of faraway luminous objects to learn about the mass distribution in the foreground [80]. Mapping out the mass distribution of the Bullet Cluster, a

https://doi.org/10.7795/110.20260227

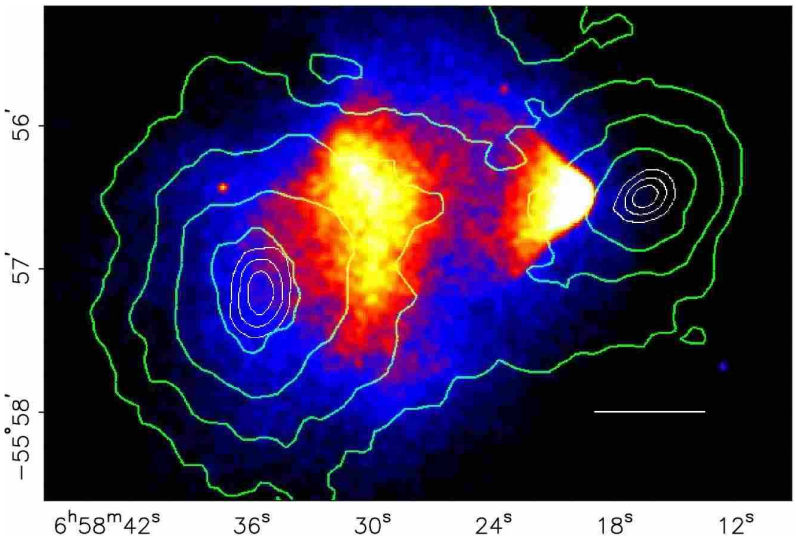

Figure 3.1: Image of the bullet cluster taken from [79]. The intensity of x-ray emission from hot gas is shown as the background heatmap, with red indicating higher emission. The green contour plot depicts the mass distribution as deduced from gravitational lensing, with the mass increasing from outer to inner contours. The white bar indicates 200 kpc at the distance of the cluster. The distribution of matter deduced from x-ray emission and that from gravitational lensing are different.

pair of merged clusters of galaxies, via gravitational lensing and comparing it with the distribution of baryonic matter obtained via x-ray detection showed that the cluster's luminous matter is clumped much more closely than its total mass [79]. As illustrated in Figure 3.1, the luminous matter is found concentrated around two far-apart locations, while the mass distribution inferred via gravitational lensing is dilute and distributed over a larger volume. The understanding is that as the two clusters merged, the baryonic matter of each heated up as a result of collisions, while dark matter passed through largely unaffected. Similar effects have since been observed for other galaxy clusters [81]. These types of observations allow placing an upper limit on possible non-gravitational self-interactions of dark matter.

Nowadays a plethora of largely independent observations exist that paint a consistent picture with dark matter making up more than 80% of matter in the universe. Together, they offer some constraints on the properties of dark matter:

- Dark matter must be stable, or extremely long-lived, since it has played a role throughout cosmological history, and is still present today.
- It is not one of the standard model particles, at least not without introducing some physics beyond the standard model.

https://doi.org/10.7795/110.20260227

- Self-interactions are small, i.e. dark matter doesn't scatter. This is needed to explain the observations from the bullet cluster and similar clusters.
- It is non-relativistic.
- It must be electrically neutral or infinitesimally charged, since otherwise it would interact electromagnetically.

Additionally, there is a lower limit on the DM mass, depending on its spin statistics:

- For fermionic dark matter models, Fermi statistics demand for only one DM particle to occupy any quantum state. At the same time, the escape velocity of a galaxy limits the speed dark matter particles can have while still being bound in the galactic halo. This sets a lower limit on the mass of any fermionic DM, if it is to make up a significant fraction of the observed DM density. For our galaxy, one finds a lower mass limit of about 10 eV (see [72] for a derivation). In dwarf galaxies, a limit on the order of 100 eV is obtained [82]. Dark matter with a smaller mass is therefore necessarily bosonic.
- For bosonic dark matter models, a lower limit on the dark matter mass is obtained when demanding that the deBroglie wavelength of a single particle is not larger than the size of a small galaxy. Otherwise, the boson can not account for the observed dark matter structures, if it is to make up all or a significant amount of DM. This is the case for a mass on the order of $10^{-22}\,\mathrm{eV}/c^2$, corresponding to a deBroglie wavelength of about 1000 ly. A more quantitative and slightly tighter limit of $2.2 \times 10^{-21}\,\mathrm{eV}/c^2$ was recently obtained in [83].

The properties of dark matter in our galaxy are particularly important for experimental searches that depend on the local presence of dark matter here on Earth. Like other spiral galaxies, the milky way displays a flat rotation curve at large distances. As mentioned above, the simplest way of reproducing this curve is via a radially symmetric dark matter halo with a density profile that scales as $\rho(r) \propto 1/r^2$. For this simple dark matter distribution, also known as the Standard Halo model (SHM) [84], it can be shown that the velocity distribution is Maxwellian [85], with a velocity dispersion $\Delta v \approx 290\,\mathrm{km/s}$. This velocity distribution is truncated at the escape velocity $v_{\mathrm{esc}} \approx 544\,\mathrm{km/s}$, which is the speed above which objects are no longer gravitationally bound in the galaxy. Our solar system moves through the dark matter halo with relative velocity of $v \approx 220\,\mathrm{km/s}$ with respect to the galactic rest

https://doi.org/10.7795/110.20260227

frame. For dark matter sensors on Earth, the dark matter velocity is additionally modulated by Earth's rotation about its axis, and its orbit around the sun.

Within the standard halo model, a dark matter energy density of $\rho_{\mathrm{DM}} \approx (0.3 - 0.4)\,\mathrm{GeV/cm^3}$ is obtained at the radius of the sun in our galaxy [86–89]. However, the resolution of this model is not at the level of our solar system, and there are no measurements of the "local" dark matter density on Earth. While we will assume the dark matter density from the standard halo model in the dark matter searches presented here, it is important to keep in mind there might be over- or under-densities of dark matter in our solar system that lead to different local values of ρ_{DM}. In particular, a gravitationally bound dark matter halo around the sun and/or the earth could lead to an increased local dark matter density [90–92].

What we don't know about dark matter is essentially everything else: Possible dark matter masses span over 40 orders of magnitude. Additionally we are lacking any information on the microscopic make-up of dark matter such as its spin, and about any possible non-gravitational interactions with the standard model content. It is important to note that that dark matter does not need to consist of one thing, but could be made up of several different types of particles forming a dark sector analogous to the plethora of particles forming the "light" sector described by the standard model.

With so many things unknown, where does one best start looking, and what types of dark matter models make sense to pursue? Broadly speaking, dark matter models that can solve some other problem in physics, in addition to explaining dark matter, offer added motivation for their theoretical and experimental pursuit. Furthermore, certain types of dark matter are popular because they seem *plausible* to physicists: In addition to being compatible with astrophysical observations, they might have a particularly simple theoretical description and a plausible production mechanism. Arguably these criteria are fulfilled for a class of dark matter models falling within the umbrella term of ultralight dark matter – meaning they span the very low end of the range of possible dark matter masses. See [72] for a recent review including detailed motivations for different types of ultralight dark matter. Within the scope of this thesis, it is sufficient to note that ultralight dark matter is a relatively simple and viable explanation for dark matter that *we can search for with the type of experiments we do*, namely optical frequency comparisons.

https://doi.org/10.7795/110.20260227

3.2 Ultralight dark matter

Ultralight dark matter (UDM) concerns dark matter with a mass in the range between about $1\,\mathrm{eV}/c^2$ and $10^{-23}\,\mathrm{eV}/c^2$. We have already seen that dark matter in this mass range is necessarily bosonic (scalar or pseudoscalar). The deBroglie wavelength $\lambda_{\mathrm{dB}} = h/mv$ of a particle with mass $m \lesssim 1\,\mathrm{eV}/c^2$ and velocity $v \approx 10^{-3}c$ is larger than about 1 mm, meaning that to obtain the observed dark matter energy density of about $0.4\,\mathrm{GeV/cm^3}$, more than 10^5 particles are needed within one deBroglie volume of λ_{dB}^3. A consequence of these high occupation numbers that ultralight dark matter would need to have in our galaxy is that it makes sense to use a classical, collective coherent-wave description rather than a description in terms of individual particles for this type of dark matter. While heavier types of dark matter are often searched for by aiming to detect the momentum imparted in a collision of individual DM particles with normal matter, this becomes impossible for ultralight dark matter. It is therefore both necessary and useful to exploit the coherent, oscillatory nature of this type of dark matter in any attempts to detect it.

Let's start by considering a scalar field of mass m_ϕ, with interactions that are small enough for it to be described by the classically oscillating, non-relativistic solutions to the equations of motion for a free massive particle:

$$\phi(t, \boldsymbol{x}) = \phi_0 \cos\left(\omega t - \boldsymbol{k}\cdot\boldsymbol{x} + \theta\right), \tag{3.2}$$

where $\omega \approx 2\pi\, m_\varphi c^2/h$ is determined by the Compton frequency, $k \approx m_\varphi v$, with $v \sim 10^{-3}\, c$ the dark matter velocity, and θ is an unknown phase that is assumed to be random.

We will follow the notation from [9, 93] in defining the dimensionless field φ, which is related to ϕ via

$$\varphi \equiv \sqrt{\frac{4\pi G}{c\hbar}}\phi = \frac{\sqrt{4\pi}}{M_{pl}}\phi\,, \tag{3.3}$$

where $M_{pl} \approx 2.18 \times 10^{-8}\,\mathrm{kg} \approx 1.2 \times 10^{19}\,\mathrm{GeV}/c^2$ is the Planck mass.

Under the assumption that the field saturates the dark matter, its (dimensionless) amplitude is

$$\varphi_0 \equiv \sqrt{\frac{4\pi G\hbar^2}{c^6}}\,\frac{\sqrt{2\rho_{DM}}}{m_\varphi} \approx 7 \times 10^{-16}\left(\frac{10^{-15}\,\mathrm{eV}/c^2}{m_\varphi}\right) \tag{3.4}$$

https://doi.org/10.7795/110.20260227

for a local dark matter energy density of $\rho_{\mathrm{DM}} \approx 0.4\,\mathrm{GeV/cm^3} \approx 6.4 \times 10^{-5}\,\mathrm{J/m^3}$.

The dark matter particles are assumed to be virialized within the gravitational potential of the galaxy, leading to a Maxwell distribution of their velocities in the SHM. The spread $\Delta v \approx 10^{-3}c$ of the dark matter velocity distribution in our galaxy leads to a spread of the observed energies $\Delta E \approx 1/2\, m\Delta v^2$ and correspondingly of the observed angular frequencies:

$$\frac{\Delta\omega}{\omega} = \frac{\Delta E}{E} \approx \frac{\Delta v^2}{2c^2} \tag{3.5}$$

Here, $\Delta v^2 \approx \left(10^{-3}c\right)^2$, which means that on the order of 10^6 oscillations are observable before phase differences between the contributing dark matter particles become of the order one. This corresponds to a finite coherence time

$$\tau_{\mathrm{coh}} \approx \frac{h}{m_\varphi \Delta v^2} \approx 10^6 \frac{h}{m_\varphi c^2}\,, \tag{3.6}$$

which is important to consider in UDM searches that run for extended periods of time.

Additionally, within one class of velocities that are reasonably similar, many DM particles with different random phases $\theta \in [0, 2\pi)$, that are assumed to be uniformly distributed, interfere. Understanding the overall collective field as the sum over all contributing dark matter particles (assumed to have the same mass), one can obtain a Rayleigh distribution for the probability to sample a specific amplitude [94]. The amplitude of the overall (collective) oscillation therefore varies stochastically on the time scale of the coherence time. For measurements extending over many coherence times, the time-averaged amplitude of the field corresponds to $\varphi_0 \propto \sqrt{\rho_{DM}}/m_\varphi$, as denoted in Equation 3.4. For times shorter than the coherence length however, the experiment does not sample the full distribution of possible DM amplitudes. In this case, the stochasticity needs to be considered when interpreting measurement results, and leads to a re-scaling of coupling limits compared to those obtained using the deterministic amplitude φ_0 [95].

We have seen that UDM acts as a coherent wave with an oscillation frequency determined by its mass, as well as characteristic coherence and statistical properties. In the following, we will explore how this type of dark matter can effect experiments, and specifically atomic clocks, by causing minute oscillations of fundamental constants.

https://doi.org/10.7795/110.20260227

We can consider some hypothetical (small) linear couplings of UDM to the standard model fields, adding terms to the Lagrangian density of the form [9, 96]:

$$\mathcal{L}_{int} = \varphi \left[\frac{d_e}{4\mu_0} F_{\mu\nu}F^{\mu\nu} - \frac{d_g}{2\widetilde{g}_3} G^{a\mu\nu}G^a_{\mu\nu} - \sum_{f=e,u,d} \left(d_{m_f} + \gamma_q d_g \right) m_f \bar{\psi}_f \psi_f \right] . \tag{3.7}$$

Here, F is the electromagnetic tensor, μ_0 the vacuum permeability, G^a is the gluon tensor, $\widetilde{g}_3$ is the effective QCD coupling, γ_q is the anomalous dimension giving the mass running of QCD-coupled Fermions, and ψ_f are the electron e and light quark u, d fields. The d factors are dimensionless coupling constants.

Note that the normalization Equation 3.3 implies that the couplings d are suppressed by the Planck scale, such that $d = 1$ implies a small effect compared to the standard model couplings.

If, following [9], we compare the terms in this interaction Lagrangian with their corresponding standard model terms, we will see that each coupling imprints the effect of the oscillating scalar field onto a fundamental constant. Using the electron mass as an example, we can write down the term containing m_e from Equation 3.7 together with the standard model term containing the electron mass ($-m_e\bar{\psi}_e\psi_e$), yielding

$$-m_e(1 + \varphi d_{m_e})\bar{\psi}_e\psi_e \, , \tag{3.8}$$

and we can identify $m_e \to m_e(1+\varphi d_{m_e}) = m_e(1+d_{m_e}\varphi_0\cos(\omega t+\delta))$, where we used δ to denote the (unknown) overall phase of the collective UDM oscillation at some point in space. All in all, we obtain oscillations of the following five parameters (see [9] for details)

$$\begin{aligned} \alpha(t) &= \alpha \left[1 + d_e\varphi_0 \cos(\omega t + \delta)\right] \\ m_f(t) &= m_f \left[1 + d_{m_f}\varphi_0 \cos(\omega t + \delta)\right] , \quad f = e, u, d \\ \Lambda_{\mathrm{QCD}}(t) &= \Lambda_{\mathrm{QCD}} \left[1 + d_g\varphi_0 \cos(\omega t + \delta)\right] \end{aligned} \tag{3.9}$$

where Λ_{QCD} is the quantum chromodynamics (QCD) mass scale. It can be convenient to define the coupling d_q to the mean of the up and down quark masses $\hat{m} = (m_u + m_d)/2$, yielding

$$\hat{m}(t) = \hat{m} \left[1 + d_q\varphi_0 \cos(\omega t + \delta)\right] , \tag{3.10}$$

https://doi.org/10.7795/110.20260227

with

$$d_q = \frac{m_u d_{m_u} + m_d d_{m_d}}{m_u + m_d} \,. \tag{3.11}$$

Oscillations of the heavier quark masses are suppressed at the energy scales of nuclear physics $\sim 200 - 300\,\mathrm{MeV}$.

Since these oscillations of fundamental constants would have an effect on experiments, we can search for them with the tools we have available, for example optical or microwave atomic clocks, but also other oscillators such as lasers locked to ultrastable cavities, as well as different types of experiments.

In general, any oscillator frequency ν can be sensitive to several of the oscillating parameters, leading to variations $\Delta\nu$ of the form

$$\frac{\Delta\nu}{\nu} = \sum_X d_X K_X \,\varphi \equiv d_{\mathrm{eff}}\,\varphi, \tag{3.12}$$

where K_X is the sensitivity of the particular frequency to variation in the fundamental constant $X \in \{\alpha, m_e, m_u, m_d, \Lambda_{\mathrm{QCD}}\}$, and we defined the effective coupling d_{eff} for convenience.

Which couplings exactly are probed, and with what sensitivities, depends on the type of experiment. At the simplest level, atomic transition frequencies depend on the fundamental constants via the Rydberg constant $R_\infty \propto \alpha^2 m_e$, with some relativistic corrections $F_{rel}(Z\alpha)$, where Z denotes the nuclear charge. With that in mind, we can write for some optical atomic transition frequency ω_{opt}:

$$\omega_{opt} \propto R_\infty F_{rel}(Z\alpha) \propto \alpha^{2+K_{rel}} m_e \,, \tag{3.13}$$

corresponding to an effective coupling

$$d_{\mathrm{eff}}^{opt} = (2 + K_{rel}) d_e + d_{m_e} \,. \tag{3.14}$$

Here, the relativistic sensitivity coefficient K_{rel} can be obtained from calculations. Note that, as pointed out in [97], the α sensitivity $2 + K_{rel}$ is unit-dependent, which however is no longer the case for the *differences* in sensitivities that are relevant when considering frequency *ratios*.

In addition to the sensitivities to α and m_e, there is also a weaker dependence on the nuclear degrees of freedom via the dependence of the transition frequency on the nuclear charge radius and nuclear mass, i.e. the field shift and mass shift. This

https://doi.org/10.7795/110.20260227

dependence is usually neglected, and we will explore its significance and magnitude in more detail in section 3.4 for the example of $^{171}Yb^{+}$.

For hyperfine transition frequencies ω_{MW}, which result from the interaction of the electron magnetic moment with the field generated by a nuclear spin, and typically lie in the microwave range, the dependence is as follows [98, 99]

$$\omega_{\mathrm{MW}} \propto R_\infty \left[\alpha^2 F_{rel}(Z\alpha)\right] \left(\mu \frac{m_p}{m_e}\right) , \tag{3.15}$$

where μ is the dimensionless magnetic moment. The proton mass mainly depends on the nuclear binding energy and therefore Λ_{QCD}, with the quark masses contributing less than 1%, which means it is justified to write $m_p \to m_p(1 + d_g\varphi)$. The nuclear magnetic moment however, depends on $\hat{m}/\Lambda_{\mathrm{QCD}}$, so that we obtain an overall effective coupling of

$$d_{\mathrm{eff}}^{\mathrm{MW}} = (4 + K_{rel})\, d_e + 2d_{m_e} - d_g + \kappa_q(d_q - d_g) , \tag{3.16}$$

where the coefficient κ_q depends on the specific nucleus and can be obtained from calculations [98, 99].

The lengths of solid bodies depend on the fine-structure constant and electron mass via the Bohr radius a_{B} [100, 101]. When stabilizing a laser to an optical cavity, length changes of the cavity spacer are translated into frequency changes of the laser, which can be measured with high precision in optical frequency comparisons. For a laser stabilized to an optical cavity, we thus obtain

$$\omega_{\mathrm{cav}} \propto 1/a_{\mathrm{B}} \propto m_e\alpha , \tag{3.17}$$

and the corresponding effective coupling

$$d_{\mathrm{eff}}^{\mathrm{cav}} = d_{m_e} + d_e . \tag{3.18}$$

Note that the frequency ratio between two of these oscillators, A and B, typically only retains sensitivity to the dark matter field, if the oscillators depend differently on the fundamental constants and therefore feature *different* effective field couplings

$$\frac{\Delta(\nu^A/\nu^B)}{\nu^A/\nu^B} = \varphi_0\, \Delta d \cos(\omega t + \delta), \tag{3.19}$$

https://doi.org/10.7795/110.20260227

where $\Delta d = d^A_{\text{eff}} - d^B_{\text{eff}}$. From this, it follows immediately that

- Any sensitivity to variations of the electron mass cancels completely when comparing two oscillators of the same type.
- When comparing a hyperfine transition frequency to an optical transition frequency, d_{m_e} appears in the combination $\left|d_{m_e} - d_g\right|$. The effects of these two couplings may cancel each other if they are of equal magnitude.
- When comparing two optical clocks (i.e. two clocks based on transitions between states of the gross electronic structure), only the difference in the relativistic sensitivity coefficient K_{rel} between the two transitions determines the sensitivity of the measurement to variations of the fine-structure constant.

We will see in section 3.5 how sensitivity can be retained even for equal effective couplings in the case of large space- or time separation between the oscillators, and in particular how this enables to circumvent the first two points and find limits on d_{m_e} alone.

For now, let's focus on the last point and remember from chapter 2 that the ${}^2S_{1/2}(F = 0) \leftrightarrow {}^2F_{7/2}(F = 3)$ electric-octupole (E3) optical clock transition in ${}^{171}\text{Yb}^+$ features large relativistic sensitivity K_{rel}, making many frequency ratios involving this transition very sensitive to variations of α. Searching for oscillations in these frequency ratios therefore corresponds to searching for the UDM coupling d_e with high sensitivity. With this in mind, it makes sense to analyse such highly sensitive measurements for oscillations as a search for ultralight dark matter.

This type of analysis can also be recast in terms of quadratic couplings of scalar or pseudoscalar (axion-like) UDM [41, 102, 103]. Here, we focus on scalar dark matter and the linear couplings introduced above for simplicity and conciseness.

3.3 Data analysis and results

We have seen that we can search for ultralight dark matter couplings by analyzing the data from optical frequency comparisons for oscillations. Here, we use two frequency comparisons for such a search: We start out by analyzing the recent $\nu_{\text{E3}}/\nu_{\text{E2}}$ measurement data presented in section 2.3. Additionally, we analyse a measurement of the ratio $\nu_{\text{E3}}/\nu_{\text{Sr}}$ between the E3 transition frequency and the ${}^1S_0 \leftrightarrow {}^3P_0$ transition frequency in ${}^{87}\text{Sr}$, which we obtained by comparing the Yb^+ single-ion

https://doi.org/10.7795/110.20260227

clock running on the E3 transition to the Sr3 lattice clock at PTB. Ignoring – for now – a weak dependence on nuclear UDM couplings, we have $\Delta d = \Delta K_\alpha \, d_e$ and we can see that the two frequency ratios act as probes for oscillations of the fine structure constant and therefore a coupling d_e to photons:

$$\frac{\Delta(\nu_{\mathrm{E3}}/\nu_X)}{\nu_{\mathrm{E3}}/\nu_X} = \varphi_0 \, \Delta K_\alpha \, d_e \cos(\omega t + \delta) \,, \tag{3.20}$$

where $X \in \{\mathrm{E2}, \mathrm{Sr}\}$ and the differential sensitivity ΔK_α has been calculated to be 6.95 for $\nu_{\mathrm{E3}}/\nu_{\mathrm{E2}}$ and 6.01 for $\nu_{\mathrm{E3}}/\nu_{\mathrm{Sr}}$ [27].

3.3.1 Analysis of $\nu_{\mathrm{E3}}/\nu_{\mathrm{E2}}$ measurement data

We analyse about 20×10^6 s (or 235 days) of data of the frequency ratio $\nu_{\mathrm{E3}}/\nu_{\mathrm{E2}}$ taken over a period of about 26 months between MJD 59097 (September 5, 2020) and MJD 59900 (November 11, 2022). More specifically, we analyse the local offset $\delta\nu_{\mathrm{E2}}/\nu_{\mathrm{E2}}$, which contains contributions from local frequency steering, but we neglect small time-resolved shift corrections on ν_{E2}. These are the only time-dependent contributions to $\nu_{\mathrm{E3}}/\nu_{\mathrm{E2}}$ (c.f. section 2.3) via Equation 2.1. The raw data used in the analysis is shown in Figure 3.2.

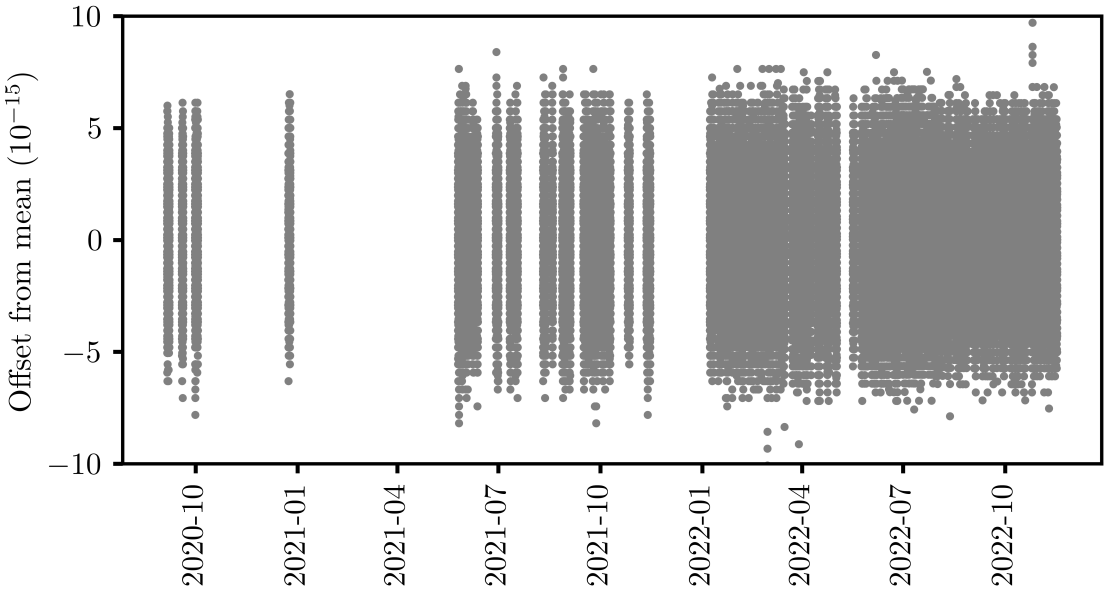

Figure 3.2: Raw data used to search for oscillations in $\nu_{\mathrm{E3}}/\nu_{\mathrm{E2}}$. A total of about 2.03×10^7 s (235 days) of data taken over a period of about 26 months is analysed. The sampling period is 10 s, and an overall offset is subtracted. The data corresponds to that shown in Figure 2.4 for this time period.

https://doi.org/10.7795/110.20260227

We are looking for oscillations of the form

$$S_\omega \sin(\omega t) + C_\omega \cos(\omega t)\,. \tag{3.21}$$

Since we do not know the dark matter mass, and therefore the corresponding oscillation frequency, we are interested in performing a broadband search, extracting the amplitude $A_\omega \equiv \sqrt{S_\omega^2 + C_\omega^2}$ for the widest possible range of angular frequencies ω. The analysis follows closely the approach detailed in [93, 104].

To handle the gapped experimental data, we first estimate the power at different frequencies using the Lomb-Scargle formalism, a method for the spectral analysis of unevenly sampled data [105, 106]. This approach is equivalent to fitting the model Equation 3.21 explicitly to the data for each frequency and constructing a periodogram from the χ^2 goodness of fit:

$$P_\omega = \frac{1}{2}\left[\chi_0^2 - \chi^2(\omega)\right]\,, \tag{3.22}$$

where χ_0^2 is obtained from the non-varying reference model ($S \equiv C \equiv 0$). Using the Lomb-Scargle formalism as implemented in the astropy python package [107] instead of standard fitting routines speeds up the computation significantly. For evenly sampled data, the periodogram P_ω reduces to that obtained from a standard discrete Fourier transform. We extract the modulation amplitude from the periodogram via

$$A_\omega = \sqrt{4\,P_\omega / N_0}\,, \tag{3.23}$$

with N_0 the number of datapoints.

The highest frequency in our analysis is 0.005 Hz, limited by the $\approx$ 200 s servo time of the optical clocks: For shorter times the laser frequencies are not yet fully determined by the atomic reference, and their stabilization to the same ultrastable optical cavity leads to common-mode rejection of signals. This time scale is also visible as a characteristic "servo bump" in the Allan deviation, c.f. Figure 3.5.

For a dataset with T the time between the beginning of the first measurement and the end of the last measurement, the Lomb-Scargle statistics are not valid for frequencies around $1/T$ and below, i.e. when signals no longer complete a whole oscillation cycle within the range of the data. Since we do not know the phase of an expected signal, we cannot rule out being close to an antinode of the oscillation. In this case, the amplitude increases with $1/\omega^2$ going to lower frequencies. To realize this

https://doi.org/10.7795/110.20260227

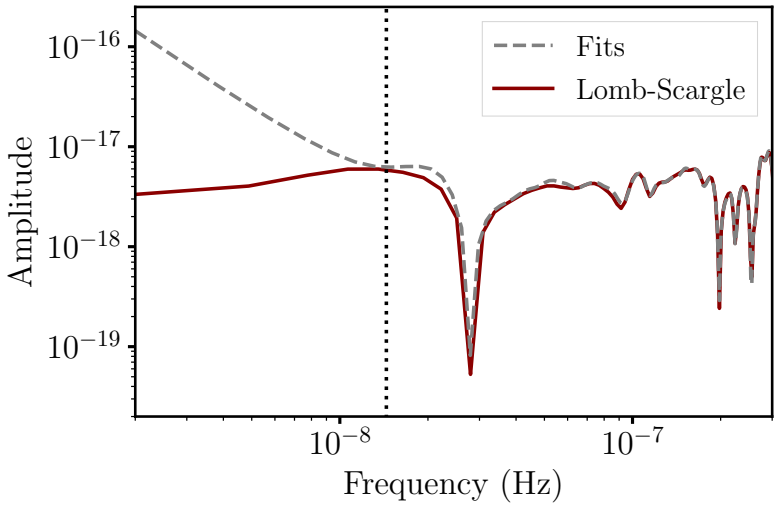

Figure 3.3: Comparison of oscillation amplitudes extracted from the dataset shown in Figure 3.2 with least-square fits (dashed grey) and the Lomb-Scargle periodogram (dark red) for small frequencies. The dotted vertical line denotes the inverse of the total measurement period. We use the fit results for frequencies below 10^{-7} Hz, and the Lomb-Scargle periodogram for larger frequencies.

consideration in our analysis, we extract the oscillation amplitude using a standard least-square fit of Equation 3.21 in this frequency range, additionally allowing a constant offset for each frequency. We check the agreement of both methods in a frequency range around $1/T \approx 1.4 \times 10^{-8}$ Hz. The amplitudes extracted from both methods in this frequency range are depicted in Figure 3.3. While both methods agree very well for frequencies $\gtrsim 1/T$, they diverge for smaller frequencies, with the fit results showing the $1/\omega^2$ scaling that is wanted in a reasonable approach, while the Lomb-Scargle result remains flat. We use the fit results for frequencies below 10^{-7} Hz, and the Lomb-Scargle results for larger frequencies. The pronounced dips visible in the amplitude spectrum are stochastic fluctuations that are compatible with white noise. We verify that both types of analysis reproduce the amplitudes of known test signals.

After having obtained the spectrum of our data, it is time to asses the statistical significance of any peaks it may contain. In other words, we need to ask: At which magnitude (power or amplitude) do we consider a peak a detection, and are there any such detections present in our spectrum, or is it fully explained by the expected measurement noise? It is common to answer this question based on a 5% detection threshold. When finding a peak above this threshold, and interpreting it as a detection, the probability of it being a false detection is less than $p_0 = 5\%$. Here, we need to account for the fact that extreme values become more likely as

https://doi.org/10.7795/110.20260227

one considers a larger number of independent samples (look-elsewhere effect) [105, 108].

The probability for a number of independent events to occur results from multiplication of the events' individual probabilities. It follows that for n_{ind} independent sample frequencies in our spectrum the detection threshold P_{th} we are looking for has to fulfill:

$$\mathrm{Prob}(P_\omega < P_{\mathrm{th}}) = (1 - p_0)^{1/n_{\mathrm{ind}}} \quad \forall\omega \tag{3.24}$$

We estimate the number of independent frequencies to be $n_{\mathrm{ind}} \approx f_{\mathrm{max}} T$, where $f_{\mathrm{max}} = 1/(200\,\mathrm{s}) = 0.005\,\mathrm{Hz}$, and obtain $n_{\mathrm{ind}} \approx 3.5 \times 10^5$. For $\omega/2\pi \gg 1/T$ and pure Gaussian white noise, the power at a given frequency follows an exponential probability distribution [105] with the corresponding cumulative distribution

$$\mathrm{Prob}(P_\omega \leq P) = 1 - \mathrm{e}^{-P/\sigma^2}\,, \tag{3.25}$$

where σ is the standard deviation of the (Gaussian) noise distribution. From this, together with Equation 3.24, the analytic expression for the detection threshold

$$P_{\mathrm{th}} = -\ln\left(1 - (1 - p_0)^{1/n_{\mathrm{ind}}}\right)\,\sigma^2 \tag{3.26}$$

follows directly, and we use $p_0 = 5\%$, as is convention. To obtain the standard deviation σ for our data, we extrapolate the fit to the Allan deviation to our sampling time of 10 s and obtain $\sigma(\tau = 10\,\mathrm{s}) \approx 3.3 \times 10^{-15}$. Note that in principle, we could also choose a detection threshold that is not frequency-independent, yet still fulfills Equation 3.24. However, in the case of white noise we have no reason to treat the different sample frequencies differently, except for the expected $P_\omega \propto 1/\omega^2$ scaling when $\omega/2\pi < 1/T$. Details on the extraction of the detection threshold for these small frequencies will be left to the next section, for now it's sufficient to note that the detection threshold shows the same $1/\omega^2$ scaling as the spectrum itself.

We do not find any peaks exceeding the detection threshold and conclude that there is no statistically significant sinusoidal modulation present in our measurement. It is useful to find an upper bound on the extracted amplitudes. Commonly, the upper bound at 95% confidence is employed. We obtain this bound on the oscillation amplitude at each frequency by assuming the extracted amplitude is a real signal and generating 1000 datasets by adding a randomly generated offset to each datapoint. The offset is drawn from a Gaussian distribution according to the observed white

https://doi.org/10.7795/110.20260227

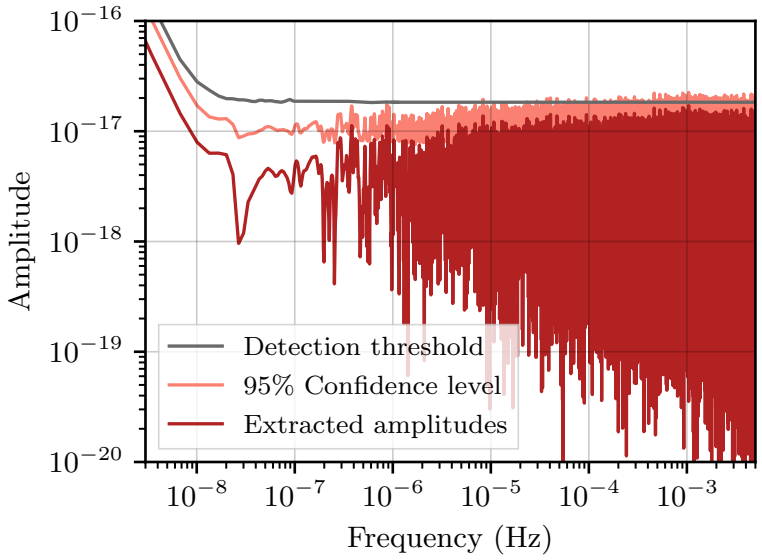

Figure 3.4: Amplitude spectrum of the ν_{E3}/ν_{E2} measurement data with the corresponding upper 95% confidence level and 5% detection threshold. See text for details.

noise. These datasets are then evaluated as described above, and taking the 95th percentile of the resulting distribution yields the upper 95% confidence level [93, 104, 109]. Due to the large amount of data, these computations were performed on the PTB high-performance-computing cluster.

The results of this analysis for the ν_{E3}/ν_{E2} measurement data, including the amplitude spectrum, detection threshold, and 95% confidence level, are presented in Figure 3.4. Our analysis yields largely frequency-independent amplitude constraints below 2×10^{-17} for frequencies $> 1/T$.

We have seen in section 2.3 that our measurement instability of the frequency ratio ν_{E3}/ν_{E2} in $^{171}Yb^+$ was limited by the short interrogation time on the E2 transition, and the limited duty cycle of the corresponding clock during interleaved interrogation. The clock running on the E3 transition is much more stable due to its 500 ms interrogation time and more favourable duty cycle. It therefore makes sense to investigate the full potential of the $^{171}Yb^+$ E3 clock to search for oscillations of the fine-structure constant by comparing it to a more stable clock with suitable α-sensitivity. A good candidate is an optical lattice clock based on the $^1S_0 \leftrightarrow {}^3P_0$ transition in ^{87}Sr.

https://doi.org/10.7795/110.20260227

3.3.2 Comparison with Sr lattice clock

We analyse data from a short measurement campaign comparing the $^{171}Yb^+$ E3 single-ion clock to the Sr3 lattice clock at PTB in the spring of 2022. Details on the lattice clock apparatus can be found in [110]. The measurement setup used for the comparison is described in [68]. The α-sensitivity of the the $^1S_0 \leftrightarrow {}^3P_0$ transition in ^{87}Sr is close to zero [27], yielding a differential sensitivity of 6.01 for ν_{E3}/ν_{Sr}, which is only slightly smaller that of ν_{E3}/ν_{E2}.

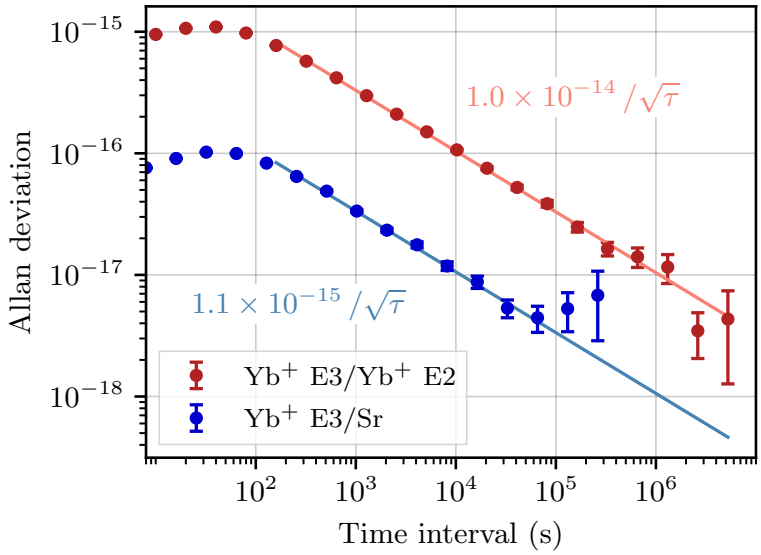

Figure 3.5: Instability of both frequency ratio measurements as characterized by the Allan deviation. The solid lines are fits to the Allan deviation with the $1/\sqrt{\tau}$ scaling expected for white noise. Deviations from this scaling are apparent for the ν_{E3}/ν_{Sr} measurements at long averaging times, see text for details.

The measurement features a fractional instability of $1.1 \times 10^{-15}/\sqrt{\tau(\mathrm{s})}$, limited by the quantum projection noise of the single-ion clock. The instability as characterized by the Allan deviation is shown in Figure 3.5, with that of the ν_{E3}/ν_{E2} data analysed in the previous section included for comparison. Deviation from the expected white noise behaviour is visible for averaging times above about 10^5 s. We include this behaviour in the data analysis: While we assumed pure white noise with an amplitude extracted from the fit to the Allan deviation for the ν_{E3}/ν_{E2} data, for the ν_{E3}/ν_{Sr} data we *additionally* add random walk noise ($1/\omega^2$ power spectrum) with an amplitude of 9×10^{-18}, reproducing the increase of the Allan deviation we observe at long averaging intervals. From the measurements presented so far, the cause of this excess noise cannot be identified. Even though the ratio ν_{E3}/ν_{E2}

https://doi.org/10.7795/110.20260227

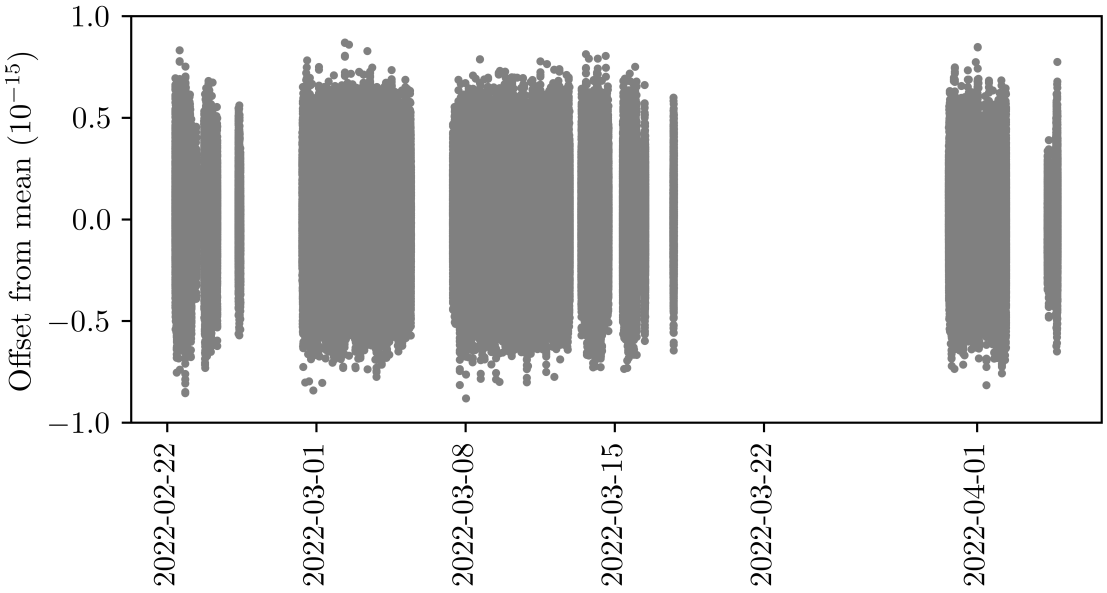

Figure 3.6: Raw data used to search for oscillations in $\nu_{\mathrm{E3}}/\nu_{\mathrm{Sr}}$. A total of about 1.2×10^6 s (14.2 days) of data taken over a period of about 41 days is analysed. The sampling period is 1 s, and an overall offset is subtracted. Note the factor 10 increased scale of the y-axis compared to Figure 3.2

shows white-noise behavior over very long averaging times, the effects of technical problems could theoretically be common-mode suppressed by the fact that the same ion is interrogated for both clocks involved, and the laser for interrogation of the E2 transition is frequency-stabilized to that used for the E3 transition. However, repeated comparisons of both the $^{171}\mathrm{Yb}^+$ E3 clock and the Sr lattice clock with a third independent clock based on $^{115}\mathrm{In}^+$ ions paint a clearer picture [21]: Comparisons of $^{171}\mathrm{Yb}^+$ E3 with the In^+ clock have demonstrated a repeatability at the low 10^{-18} level over more than two years, while comparisons of both clocks with the Sr lattice clock show excess scatter at long times. This makes it plausible that the excess noise observed here can also be attributed to the lattice clock.

In total, we evaluate about 343 hours, or 14.2 days, of measurement data of $\nu_{\mathrm{E3}}/\nu_{\mathrm{Sr}}$ taken over a period of about $T = 41$ days. The raw data at a 1 s sampling is depicted in Figure 3.6. We follow almost exactly the analysis detailed in the previous section, with the only exception caused by the slightly more complicated noise model: Due to the additional noise, the probability distribution of the estimated power spectrum, and the corresponding detection threshold, are no longer known analytically. The detection threshold can in principle be obtained directly from Monte-Carlo (MC) sampling of noise, similar ot the 95% confidence levels, but without including the real signal. However, this would require an extremely large number of samples that

https://doi.org/10.7795/110.20260227

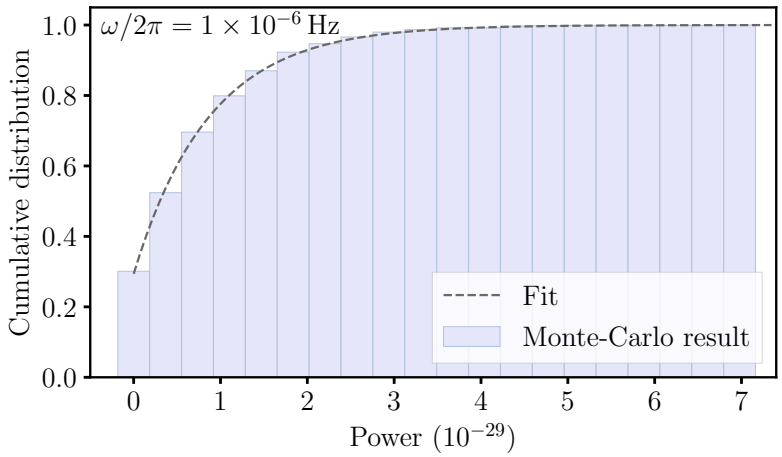

Figure 3.7: Determination of detection threshold for $\omega/2\pi = 1\times10^{-6}$ Hz. The histogram shows the cumulative probability distribution of the power obtained from 1000 Monte-Carlo samples. The dashed line shows the result of a fit of $1 - e^{-a(P-P_0)}$, which allows extracting a detection threshold of $P_{\text{th}} = 8.8\times10^{-29}$, corresponding to an amplitude of 1.7×10^{-17}. Since this detection threshold corresponds to the $1 - (3 \times 10^{-6})$th percentile of the distribution, it cannot be accessed directly from a computationally feasible number of Monte-Carlo samples.

is not computationally feasible: Even for the comparatively short data set of $\nu_{\text{E3}}/\nu_{\text{Sr}}$, $0.95^{1/n_{\text{ind}}} \approx 1-(3\times10^{-6})$, with $n_{\text{ind}} = 1.8\times10^3$ estimated as before, meaning that on the order of 10^6 Monte-Carlo samples are necessary to obtain the detection threshold directly from the corresponding percentile of the probability distribution. A variety of approaches to this problem have been developed in different fields and for different statistics [111–113]. Here, we make use of the fact that an exponential distribution still yields a good fit to the probability distribution of the estimated power at a given frequency, *when allowing for a constant offset*, and extract the threshold based on such a fit for a smaller number of MC samples. Convergence of the obtained results is at the few-percent-level already for $N = 1000$ MC samples, and the quality of the fit to the results of the MC sampling is good throughout the parameter space considered, even for small frequencies and including the random-walk noise component. To determine the detection threshold, we thus fit the cumulative of an exponential distribution to a histogram of the cumulative extracted power P, and determine the detection threshold based on the resulting fit parameters, then calculate the corresponding amplitude.

As an example, Figure 3.7 depicts the cumulative sum of the power histogram resulting from sinusoidal fits to $N = 1000$ datasets of pure noise for $\omega/2\pi = 1.0\times10^{-6}$ Hz.

https://doi.org/10.7795/110.20260227

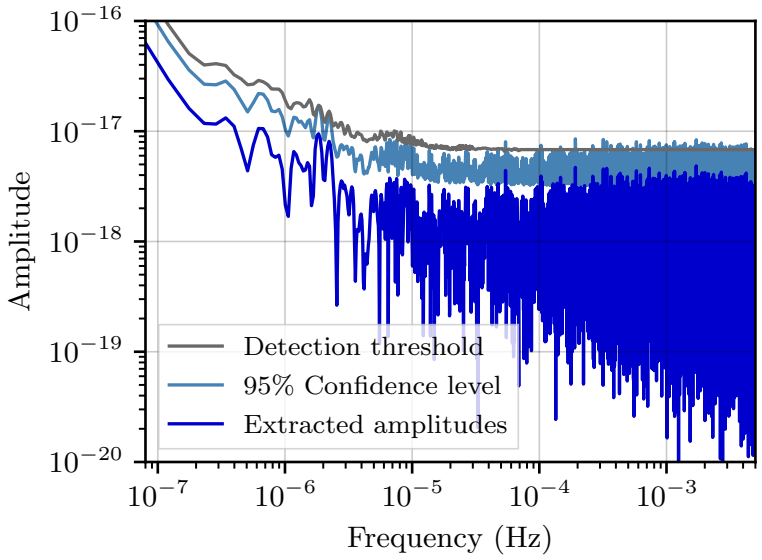

Figure 3.8: Amplitude spectrum of the ν_{E3}/ν_{Sr} measurement data with the corresponding upper 95% confidence level and 5% detection threshold. See text for details.

The detection threshold is extracted from the depicted fit of the form $1 - e^{-a(P-P_0)}$, and yields $P_{th} = 8.8 \times 10^{-29}$, or equivalently a threshold amplitude of 1.7×10^{-17}. Note that the histogram alone (without the fit) would not allow to access the detection threshold for this number of samples.

We confirm the agreement of this method with the analytical detection threshold (c.f. Equation 3.24) for intermediate frequencies, and rely on the analytic result for large frequencies $\gg 1/T$, also in the case of ν_{E3}/ν_{E2}. For ν_{E3}/ν_{Sr}, we rely on the analytic result only for frequencies larger than 4×10^{-5} Hz, where the $1/\omega^2$ noise component is negligible and the measurement is dominated by white noise. For determination of both the 95% confidence levels and the detection threshold, the random walk noise component is generated on a continuous dataset first, which is then gapped in accordance with the timestamps of our measurement.

The full amplitude spectrum with the corresponding 95% confidence level and the detection threshold is shown in Figure 3.8. The random walk noise leads to an $1/\omega$ scaling visible in the amplitude spectrum at intermediate frequencies between approximately $10^{-5} - 10^{-6}$ s, which corresponds to the deviation from white noise visible in the Allan deviation (Figure 3.5). For even smaller frequencies $< 1/T \approx 3 \times 10^{-7}$ Hz, we additionally see the expected $1/\omega^2$ scaling. The visible structure of the detection threshold at low frequencies results from the specific distribution

https://doi.org/10.7795/110.20260227

of sampling gaps in our data. The $\nu_{\mathrm{E3}}/\nu_{\mathrm{Sr}}$ amplitude spectrum does not show any statistically significant peaks. The corresponding 95% confidence level offers almost a factor 3 stricter amplitude constraints than that of the $\nu_{\mathrm{E3}}/\nu_{\mathrm{E2}}$ data for frequencies above the mid-10^{-6} Hz range due to the better instability of this measurement.

It is important to note that the limits on oscillation amplitudes depicted in Figure 3.4 and Figure 3.8, though they are presented in the context of ultralight dark matter here, are purely a result of data analysis and therefore *model-independent*. The amplitude limits can be used to constrain any model that predicts oscillations of the analysed optical frequency ratios. Keeping that in mind, let's take a look at the specific implications these results have for a coupling d_e of UDM to photons.

3.3.3 Coupling limits

Assuming the field φ with one specific mass m_φ comprises all of the dark matter, we can translate our limits on the amplitude A_ω of a sinusoidal modulation with frequency $\omega/2\pi$ in our data to limits on the absolute value of the scalar coupling d_e by combining Equation 3.4 and Equation 3.20:

$$|d_e| = \frac{\omega A_\omega}{\Delta K_{rel}} \sqrt{\frac{c^2}{8\pi G \rho_{DM}}} \,. \tag{3.27}$$

The limits deduced from the 95% confidence levels shown in Figure 3.4 and Figure 3.8 are depicted in the exclusion plot Figure 3.9. We reproduce previous limits in this mass range from the literature for reference. The total time spanned by our measurements of $\nu_{\mathrm{E3}}/\nu_{\mathrm{E2}}$ is $T \approx 2\,\mathrm{years}$, while the shortest coherence time, corresponding to the largest investigated mass $m_\varphi \approx 2 \times 10^{-17}\,\mathrm{eV}$, is about 6 years. Therefore, we do not account for finite coherence. We incorporate the effect of stochastic fluctuations of the dark matter amplitude by re-scaling our limits with a factor of 1/3 (c.f. section 3.2). This factor has also been applied to all data shown in Figure 3.9 that originally neglected stochastic fluctuations. The slope visible in many of the depicted limits from atomic clock comparisons results from the proportionality to ω and therefore the dark matter mass (c.f. Equation 3.27) that is obtained for frequency-independent amplitude limits. A characteristic change in slope happens for dark matter masses corresponding to the inverse of the total duration spanned by a measurement, with amplitude limits scaling as $1/\omega^2$ for small frequencies, yielding coupling limits that scale as $1/\omega$.

https://doi.org/10.7795/110.20260227

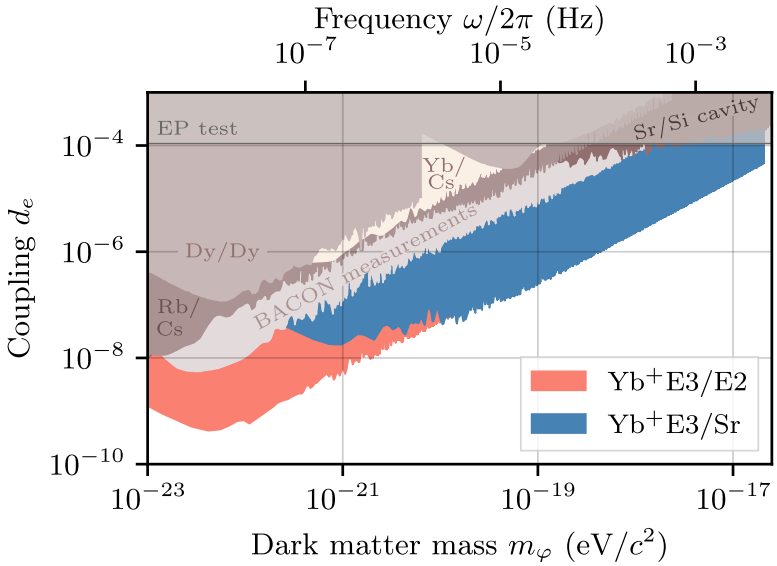

Figure 3.9: Exclusion plot for the coupling of ultralight bosonic dark matter to photons. The limits deduced from our measurements of ν_{E3}/ν_{E2} (ν_{E3}/ν_{Sr}) are shown in light pink (light blue) based on the 95% confidence levels in Figure 3.4 (Figure 3.8). Also included are previous limits reproduced from the literature: Those based on tests of the Equivalence Principle (EP test) [114, 115], the radiofrequency spectroscopy of different isotopes of dysprosium (Dy/Dy) [104], the frequency comparison of microwave atomic clocks with rubidium and cesium (Rb/Cs) [93], the comparison of a strontium lattice clock and a silicon cavity (Sr/Si) [109], several optical clock comparisons from the Boulder atomic clock optical network (BACON) [116], as well as the comparison of an Yb lattice clock with a Cs fountain (Yb/Cs) [117].

Our constraints of $|d_e|$ based on the measurements of ν_{E3}/ν_{Sr} are about a factor of 3 more stringent than those based on ν_{E3}/ν_{E2} for masses above $10^{-20}\,\mathrm{eV}/c^2$. For smaller masses, the long-term measurement of ν_{E3}/ν_{E2} yields tighter limits. Our combined results yield more than an order of magnitude improvement over all previous bounds for masses ranging from the mid-10^{-23} to the mid-$10^{-18}\,\mathrm{eV}/c^2$ range.

As discussed in section 3.2, the assumption that the field of mass m_φ makes up all of the dark matter needs to be relaxed for masses below $\approx 10^{-22}\,\mathrm{eV}/c^2$, corresponding to a de Broglie-wavelength the size of a small galaxy, which is not considered in any of the depicted limits. This is why we only show limits for masses above $10^{-23}\,\mathrm{eV}/c^2$, even though our amplitude limits extend to smaller frequencies. Note also that we assumed the ambient dark matter energy density of $\rho_{DM} \approx 0.4\,\mathrm{GeV/cm^3}$ predicted by the standard halo model, but local over- or underdensities are theoretically possible. Of the depicted limits, only those based on tests of the equivalence principle do not depend on the local dark matter density.

https://doi.org/10.7795/110.20260227

In summary, we have utilized the high sensitivity of the $^{171}Yb^{+}$ E3 transition to variations of the fine structure constant in two optical clock comparisons to substantially improve constraints on the coupling of ultralight bosonic dark matter to photons. While the E3 transition offers the highest sensitivity to α variations in currently operational optical clocks, a potential future nuclear optical clock based on thorium [118, 119], would offer much higher sensitivity, and could potentially investigate a coupling several orders of magnitude below the limits presented here. A clock based on neutral ytterbium [58], as well as certain species of highly charged ions [120, 121] could also offer improved sensitivity. On the other hand, already with the sensitivities employed in this work, improved searches can be conducted, for example with a yearslong frequency comparison between a clock based on the E3 transition and a highly stable partner clock that features a small or opposite-sign sensitivity to α-variations. Additionally, the stability of the clock based on the E3 transition can be improved by achieving longer coherent interrogation times and/or interrogating multiple ions simultaneously. Experimental steps towards these improvements are realized within a new optical clock apparatus and will be discussed in chapter 4.

https://doi.org/10.7795/110.20260227

3.4 Effects of nuclear couplings

So far, we have considered comparisons between two optical clocks to be only sensitive to variations of the fine-structure constant. However, optical atomic transition frequencies do depend on the nucleus. In the simplest picture, the electronic transitions are affected by the finite mass of the nucleus (mass shift) and its finite charge radius r_N (field shift). It therefore makes sense to ask ourselves if we can utilize these effects and investigate couplings of UDM to quarks and gluons with optical clock comparisons. Typically, these couplings are investigated using measurements involving atomic hyperfine transitions [93, 109, 117, 122] or molecular vibrational transitions [123]. In comparison, we expect smaller contributions of nuclear effects to the involved transition frequencies in our case, and therefore lower sensitivities to UDM-nuclear couplings. However, the exquisite precision and ongoing improvements in optical clock comparisons make it worthwile to consider dark matter searches even via sub-leading effects.

Investigating the effects of the nucleus on optical atomic transitions is well-established in the context of King plots [124]. There, changes in the frequencies of several narrow optical transitions between different isotopes are analysed for deviations from the standard scaling of the mass and field shifts. This approach has yielded fruitful results for the understanding of nuclear effects and set bounds on a hypothetical boson coupling neutrons and electrons [59, 125–128]. While electronic transitions typically change by several GHz when going from one isotope to another, the effects we consider here are for a single isotope and therefore much smaller. Also, while we know that electronic frequencies change between isotopes, their oscillation due to dark matter couplings is hypothetical and depends on the local presence of ultralight dark matter with specific interactions.

To demonstrate this new approach, we will use our previously presented measurements of $\nu_{\mathrm{E3}}/\nu_{\mathrm{E2}}$ in $^{171}\mathrm{Yb}^{+}$ (c.f. section 2.3) as an example, and derive limits on UDM-nuclear couplings from the limits on oscillation amplitudes in Figure 3.4. To obtain the sensivity of this frequency ratio to the UDM-nuclear couplings, we need to know the sensitivites of the involved transitions on changes to the nuclear charge radius and mass, and we need to know how these nuclear properties depend on changes of the fundamental constants (the quark masses and QCD mass scale). The main ideas and overall results will be outlined in the following, with details on the calculations, which were performed by others, left to the original publication [129].

https://doi.org/10.7795/110.20260227

The total electronic energy E_{tot} of an atomic state contain the energies associated with the mass shift (MS) and the field shift (FS). They can be parameterized as

$$E_{\text{MS}} \simeq K_{\text{MS}} \frac{1}{m_A} \propto \frac{1}{A} \text{ and } E_{\text{FS}} \simeq K_{\text{FS}} \left\langle r_N^2 \right\rangle \propto A^{2/3}\,, \tag{3.28}$$

where K_{MS} and K_{FS} are the mass-shift and field-shift constants and the mass m_A of an atom with atomic mass number A is largely determined by the mass m_N of the nucleus.

The variation of the total electronic energy associated with the nuclear degrees of freedom can be written as [130]:

$$\left.\frac{\Delta E_{\text{tot}}}{E_{\text{tot}}}\right|_{\text{nuc}} \simeq -\frac{E_{\text{MS}}}{E_{\text{tot}}} \frac{\Delta m_N}{m_N} + \frac{E_{\text{FS}}}{E_{\text{tot}}} \frac{\Delta \left\langle r_N^2 \right\rangle}{\left\langle r_N^2 \right\rangle}\,. \tag{3.29}$$

For heavy nuclei, the second term dominates, as is the case for $^{171}\text{Yb}^+$ considered here. Calculations show that the MS is 30 times smaller than the FS for the $E3$ transition and 300 times smaller for the $E2$ transition. For this reason, we concentrate on the field shift in the following.

Then, by comparing two electronic transition frequencies ν_A and ν_B of a heavy atom, we obtain

$$\frac{\Delta(\nu_A/\nu_B)}{(\nu_A/\nu_B)} = K_{A,B} \frac{\Delta \left\langle r_N^2 \right\rangle}{\left\langle r_N^2 \right\rangle}\,, \tag{3.30}$$

where we defined

$$K_{A,B} \equiv \frac{K_{\text{FS}}^{\nu_A} \left\langle r_N^2 \right\rangle}{\nu_A} - \frac{K_{\text{FS}}^{\nu_B} \left\langle r_N^2 \right\rangle}{\nu_B}\,. \tag{3.31}$$

This discussion can be extended to transitions in two different atomic species when allowing for two different charge radii.

The FS coefficients K_{FS} are calculated for the E2 and E3 transitions in a state-of-the-art variational approach to be $K_{\text{FS}}^{\nu_{\text{E2}}} = -15\,\text{GHz/fm}^2$ and $K_{\text{FS}}^{\nu_{\text{E3}}} = 40\,\text{GHz/fm}^2$, with an estimated uncertainty of $12-15\%$. Using the calculated FS coefficients and $\langle r_N \rangle \approx 5.3$ fm [131], we obtain

$$K_{\text{E3,E2}} = \left(\frac{K_{\text{FS}}^{\nu_{\text{E3}}}}{\nu_{\text{E3}}} - \frac{K_{\text{FS}}^{\nu_{\text{E2}}}}{\nu_{\text{E2}}} \right) \left\langle r_N^2 \right\rangle \simeq 2.4 \times 10^{-3}\,. \tag{3.32}$$

https://doi.org/10.7795/110.20260227

When considering the dependence of the nuclear charge radius on the oscillating fundamental constants, it is useful to first note that the mean squared nuclear charge radius of heavy elements is dominated by the distribution of protons within the nucleus rather than the charge structure of individual nucleons [132] (see also [133] and references therein). The distribution of protons is characterized by two effects that control the typical internucleon distance scale: The first is associated with the finite size of individual nucleons, while the second results from the internucleon-interactions, which are related to pion-exchange processes. Taking both effects into account, we can parametrize the dependence of $\langle r_N^2 \rangle$ as

$$\frac{\Delta \langle r_N^2 \rangle}{\langle r_N^2 \rangle} \approx \alpha \frac{\Delta \Lambda_{\mathrm{QCD}}}{\Lambda_{\mathrm{QCD}}} + \beta \frac{\Delta m_\pi^2}{m_\pi^2}, \tag{3.33}$$

where we introduced the coefficients α and β, which are of order unity, and m_π denotes the pion mass. The variation of $m_\pi^2 \propto \Lambda_{\mathrm{QCD}} \hat{m}$ [134] can be related to d_g and $d_{\hat{m}}$ as

$$\frac{\Delta m_\pi^2}{m_\pi^2} = \left(d_g + d_{\hat{m}}\right) \varphi(t)\,. \tag{3.34}$$

We obtain the following overall dependence of an optical frequency ratio in a heavy atom or ion on the scalar UDM-nuclear couplings:

$$\frac{\Delta(\nu_A/\nu_B)}{(\nu_A/\nu_B)} = K_{A,B} \left[(\alpha+\beta) d_g + \beta d_{\hat{m}}\right] \varphi(t) \tag{3.35}$$

Values of $\alpha \approx -1.1$ and $\beta \approx -0.34$ are obtained from a mean-field approach with an estimated uncertainty of 30%.

The exclusion plots for the scalar UDM couplings d_g to gluons and $d_{\hat{m}}$ to the quark masses resulting from the amplitude limits found for $\nu_{\mathrm{E3}}/\nu_{\mathrm{E2}}$ (c.f. Figure 3.4) and the considerations outlined above are shown in Figure 3.10. For reference, we reproduce other limits in this mass range from the literature. Our limits are competitive compared to other spectroscopic limits [93, 109, 117], but importantly rely on a completely different effect, which makes our search complementary to previous results. For reference, we also plot the much weaker limits derived from the mass shift. This effect is suppressed here, but it can be used instead of the field shift to probe the nuclear degrees of freedom with optical clocks based on light elements.

Note that in [136] a slightly larger and positive value of β is obtained from extending the previously calculated dependence of the charge radius on the fundamental

https://doi.org/10.7795/110.20260227

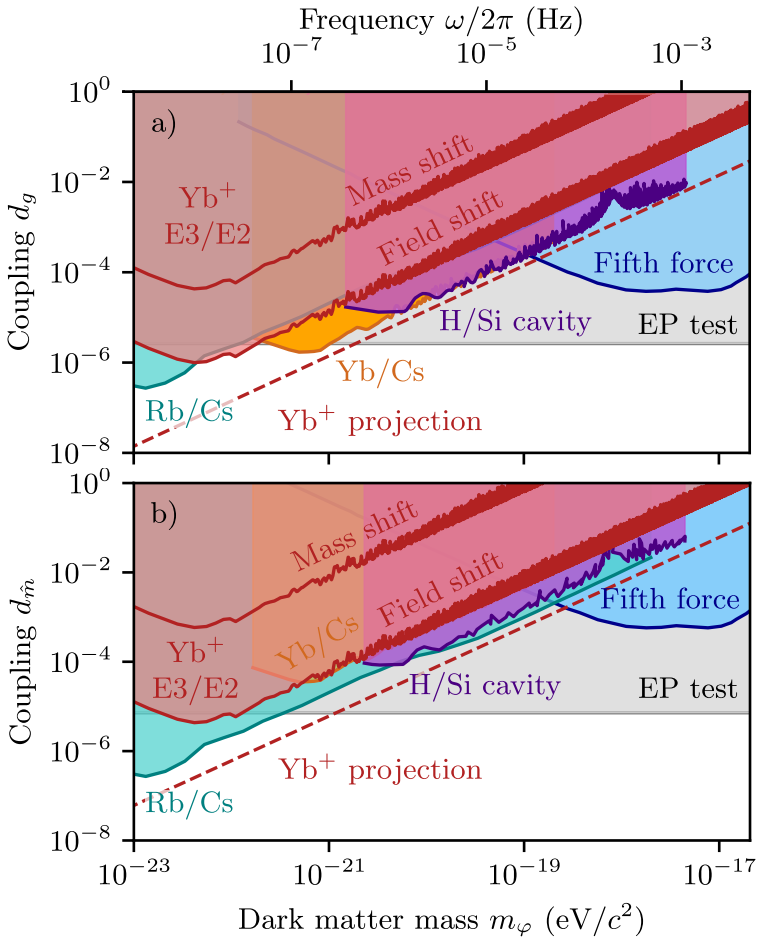

Figure 3.10: Exclusion plot for the linear scalar dark matter coupling a) to the gluons d_g and b) to the quark masses $d_{\hat{m}}$ as a function of mass m_φ. Using the field shift effect, limits at the 95% confidence level from our measurements of the frequency ratio ν_{E3}/ν_{E2} are shown in dark red. Based on the same data, the much weaker limit from the mass shift is shown for reference. The dashed line shows a projection assuming amplitude limits at the 1×10^{-18}-level. The grey and the blue lines depict the strongest EP bound [114, 115] and the bound from various fifth force searches [135], respectively. Bounds from existing spectroscopy experiments are also shown: Rb/Cs [93] (turquoise), Yb/Cs [117] (orange), H/Si cavity [109] (purple).

https://doi.org/10.7795/110.20260227

constants in light nuclei to heavy nuclei, assuming a universal scaling of the charge radius as $r_N = A^3\, r_{N,0}$.

The dependence on the nuclear couplings discussed here is *additional* to the dependence on d_e discussed previously, so the full differential effective coupling probed by measurements of $\nu_{\mathrm{E3}}/\nu_{\mathrm{E2}}$ is

$$\begin{aligned} \Delta d_{\mathrm{eff}} &= \Delta K_{rel}\, d_e + K_{E3,E2}\left[(\alpha+\beta)\, d_g + \beta\, d_{\hat{m}}\right] \\ &\approx -6.95\, d_e - 3.5\times 10^{-3} d_g - 0.8\times 10^{-3} d_{\hat{m}}\,. \end{aligned} \tag{3.36}$$

The considerations for $^{171}\mathrm{Yb}^+$ outlined here are proof-of-principle and the dependence on nuclear couplings via the mass shift and/or field shift plays a role in other optical frequency comparisons, including those presented in this thesis. However, the corresponding sensitivities have not been calculated yet.

Independent of considerations in the context of ultralight dark matter, the dependence of the frequency ratio on the nuclear fundamental constants can also be used to derive limits on e.g. a linear drift of the mean of the light quark masses from our measurements, as pointed out and calculated in [136]. Using our limit on a linear drift of $\nu_{\mathrm{E3}}/\nu_{\mathrm{E2}}$ presented in section 2.4 and the sensitivity above (Equation 3.36), we obtain

$$\frac{1}{\hat{m}}\frac{\mathrm{d}\hat{m}}{\mathrm{d}t} = 1.5(2.2)\times 10^{-15}/\mathrm{yr}\,. \tag{3.37}$$

This value has more than an order of magnitude higher uncertainty than the best published limit of $1.36(0.91)\times 10^{-16}$/yr based on the comparison of Rb and Cs hyperfine transition frequencies over 12 years, which features a much larger sensitivity of -21×10^{-3} to variations of $\hat{m}$ [137].

In summary, even though the dependence of optical clock comparisons on the nuclear fundamental constants is generally smaller than that of frequency comparisons involving hyperfine transitions, we obtained competitive limits on UDM-nuclear couplings. The effect of the mass and/or field shifts on optical clock transitions should therefore not be neglected when searching for variations of fundamental constants, and could improve dark matter searches as optical clocks continue to develop.

https://doi.org/10.7795/110.20260227

3.5 The case of equal sensitivities - effects of space- and time separation

In section 3.2, we have seen that for typical experiments measuring the frequency ratio of a pair of co-located oscillators A and B, the ratio will only contain a field-induced contribution if the oscillators have *different* effective field couplings (i.e. if they depend differently on the fundamental constants). As a consequence, for co-located comparisons at low frequency, terms containing d_{m_e} never appear alone, but rather in some relative combination [97, 138] (see Refs. [101, 139] for discussions on high-frequency comparisons). Hyperfine transitions depend on the electron-to-proton mass ratio m_e/m_p, and consequently comparing an optical to a microwave transition leads to effective couplings including $|d_{m_e} - d_g|$ [98, 99]. This is important since in the simplest models d_{m_e} and d_g may be similar or equal [9], leading to a cancellation of signals.

A pair of space-time separated oscillators, on the other hand, will experience a different local value of the scalar field due to its oscillations. In this case, the frequency ratio for a pair of oscillators with identical effective couplings will gain the field-induced shift

$$\begin{aligned}\frac{\Delta(\nu_A/\nu_B)}{\nu_A/\nu_B} &= \varphi_0\, d_{\text{eff}} \left[\cos(\omega t) - \cos(\omega t - \delta)\right] \\ &\approx \varphi_0\, d_{\text{eff}} \sin(\omega t)\, \delta,\end{aligned} \tag{3.38}$$

where we used $|\delta| \ll 1$ for the scalar field phase difference between the two oscillators and ignored the overall, common phase of the field.

Two terms contribute to the phase difference δ: the time delay Δt due to the signal propagation between the two oscillators, and a term due to the spatial separation

$$\delta = \omega \Delta t - \boldsymbol{k} \cdot \Delta \boldsymbol{x}, \tag{3.39}$$

where $\Delta \boldsymbol{x} = D\, \boldsymbol{n}$, with D the linear distance between the oscillators, and $\boldsymbol{n}$ the separation unit vector. In the considered mass range $m_\varphi \lesssim 10^{-14}\,\text{eV}$, we have $\lambda_\varphi = 2\pi/k \gtrsim 10^8\,\text{km} \gg D$, so the field can be considered coherent across all oscillators. Notice that $kD/(\omega\Delta t) \approx v/c \approx 10^{-3}$. Therefore, the contribution of the spatial phase difference can be neglected, unless the contribution of the temporal term is experimentally suppressed.

https://doi.org/10.7795/110.20260227

For a dark matter interpretation, $\varphi_0 \propto 1/m_\varphi$, while $\omega \propto m_\varphi$. At the same time, both terms in the phase shift (3.39) are linear in m_φ. Therefore, the signal amplitude (3.38) would be independent of the dark matter mass. This is in contrast to most dark matter searches, where the signal amplitude would scale inversely with the mass (c.f. subsection 3.3.3).

The signal (3.38) has a linear scaling with the effective distance (D or $\Delta t/c$) between the oscillators, which offers a method to enhance the sensitivity with spatially separated sensors. Crucially, the dependence on distance may also act as a key dark matter signature: A network of comparisons with multiple distances could be used to exclude spurious terrestrial sources for the oscillations.

The network of optical fiber-linked atomic clocks and cavities located at PTB in Germany, LNE-SYRTE in France, INRIM in Italy, and NPL in the United Kingdom [140–145] is particularly suitable for precision frequency comparisons over large distances. The fiber links allow state-of-the-art comparisons of optical frequencies over $\sim 10^3$ km distances with $\lesssim 10^{-17}$ precision [143, 146]. The network has been employed previously for tests of fundamental physics [147], and to search for transient variations in fundamental constants and dark matter [148].

As an initial search demonstrating our method, we analyse publicly available data from a pair of ultra-stable lasers located at NPL and PTB [146, 149]. The frequencies of the cavity-stabilized lasers are compared via the optical fiber links, and have been measured to achieve a fractional frequency instability as low as 7×10^{-17} [146].

The fiber-link distance L between the cavities is 2220 km [146], corresponding to a delay time of ≈ 10 ms. However, due to the active noise cancellation employed, the time delay contribution leads to no observable effects in the frequency comparisons. The noise cancellation works by sending a frequency signal from one oscillator to the other, reflecting it, and comparing to its source [143]. Any phase shift between the sent and received signals is assumed to be noise introduced on the fiber link and actively suppressed. Since the test signal traverses the fiber length twice, half the observed phase shift is subtracted from the signal. In the presence of the dark matter field, the test signal would gain a dark-matter–induced shift in comparison to its source [Eq. (3.38)] due to the time delay between the sent and received signals with $\delta = 2\omega\Delta t$ (where $\Delta t = nL/c$ is the one-way time delay with the fiber's refractive index n). The noise-correction signal would thus contain a component exactly equal to the time-delay contribution to the dark matter signal. As such, any signal caused by a time delay would be interpreted as noise, and removed. Since the considered

https://doi.org/10.7795/110.20260227

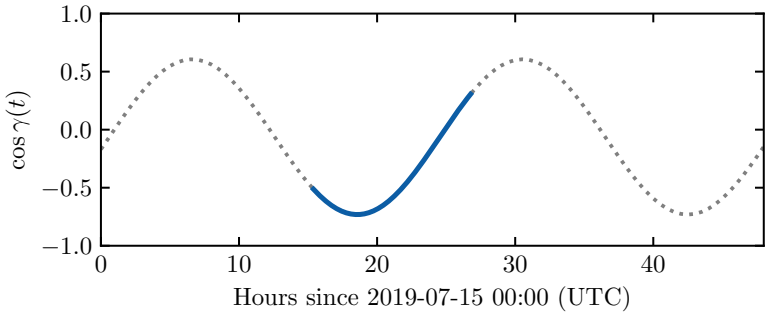

Figure 3.11: Expected daily modulation of dark matter signal according to $\boldsymbol{n} \cdot \boldsymbol{n}_\odot = \cos\gamma(t)$, where $\boldsymbol{n}$ is the separation unit vector between the cavities located at NPL and PTB, and $\boldsymbol{n}_\odot$ is the direction of Earth's motion through the dark matter halo. The solid line shows the observation period for the considered data [146].

dark-matter oscillation period is much larger than the fiber delay time, any signals originating from dark-matter–induced modifications to the length and refractive index of the fiber [138] are also removed by the noise cancellation.

On the other hand, the signal coming from the spatial separation is not removed. This provides a unique opportunity to probe the spatial fluctuations of scalar dark matter, with induced signal

$$\frac{\Delta(\nu_A/\nu_B)}{\nu_A/\nu_B} = \varphi_0 \left(d_{m_e} + d_e\right) \frac{\omega D\, \boldsymbol{n} \cdot \boldsymbol{v}}{c^2} \sin(\omega t). \tag{3.40}$$

To determine the signal strength, we average Equation 3.40 over the dark matter velocity distribution $f(\boldsymbol{v})$. In the galactic rest frame, the average would be zero. In the Earth frame, however, it is non-zero due to Earth's motion through the galaxy with speed $v_\odot \approx 220\,\mathrm{km/s}$ (roughly towards the Cygnus constellation). We have

$$\int \mathrm{d}^3\boldsymbol{v}\, f(\boldsymbol{v})\, \boldsymbol{v} \cdot \boldsymbol{n} = \boldsymbol{v}_\odot \cdot \boldsymbol{n} = v_\odot \cos\gamma(t), \tag{3.41}$$

where γ is the angle between the laboratory separation and the direction of Earth's galactic motion, which we compute using Ref. [150]. This exhibits a strong sidereal modulation due to Earth's rotation, as shown in Figure 3.11.

In general, this modulation would present a key dark matter observable. For the present data set, however, there is less than one full day of data [149]. As such, we do not search for the daily modulation, but rather average the expected signal amplitude over the observation period, finding $\langle\cos\gamma\rangle_{\mathrm{T}} \approx -0.41$ [151].

https://doi.org/10.7795/110.20260227

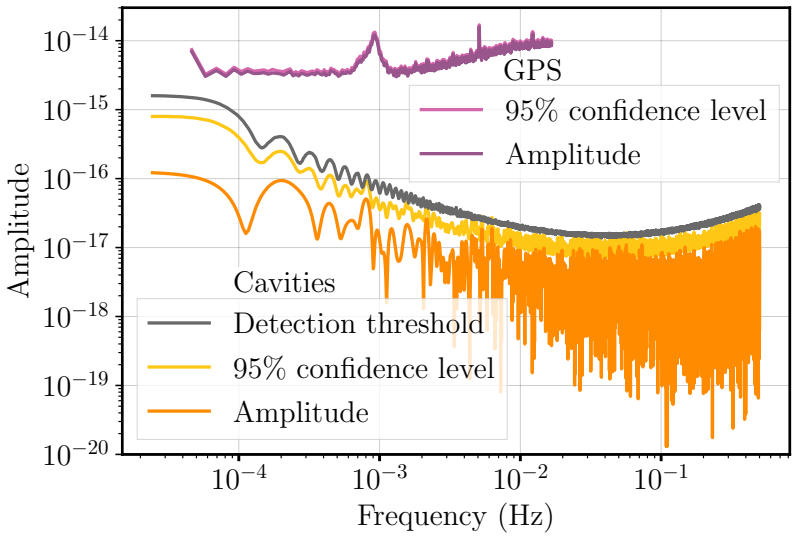

Figure 3.12: Amplitude spectrum of the NPL/PTB cavity- cavity comparison, and GPS microwave clock data, showing the upper 95% confidence levels and detection threshold.

We search for oscillations in the data following exactly the approach detailed for the optical clock comparison data in section 3.3. The resulting spectrum is shown in Figure 3.12. To obtain the 95% confidence level and the detection threshold with Monte-Carlo sampling, we implemented the full noise model as given in Table 1 of Ref. [149] using the colorednoise python package, and verified that our implementation of the model yields a similar Allan deviation compared to the original data.

The high-frequency bound of our analysis is 0.5 Hz, limited by the 1 Hz sampling rate, while the low-frequency bound is determined by the total measurement duration of 4.1×10^4 s. (Unlike for the data in section 3.3, we do not extend the limits to lower frequencies with individual fits here.) For frequencies $f = \omega/(2\pi) < 1$ Hz, the dark matter coherence time is $\tau_c > 10^6$ s, well above the total measurement duration.

We find no statistically significant oscillations in the data given the available noise model, and therefore place constraints on the magnitude of $|d_e + d_{m_e}|$. By combining with the existing constraints on $|d_e|$ [40, 117, 122, 152, 153] , c.f. section 3.3, which are at least an order of magnitude tighter, we place the first constraints on $|d_{m_e}|$ alone in this mass range, which we present in Figure 3.13. The previous experiments in this range probe combinations including $|d_{m_e} - d_g|$. In the analysis, we account for the stochastic nature of the scalar fields by re-scaling our limits by a factor of 1/3, as discussed in section 3.2.

https://doi.org/10.7795/110.20260227

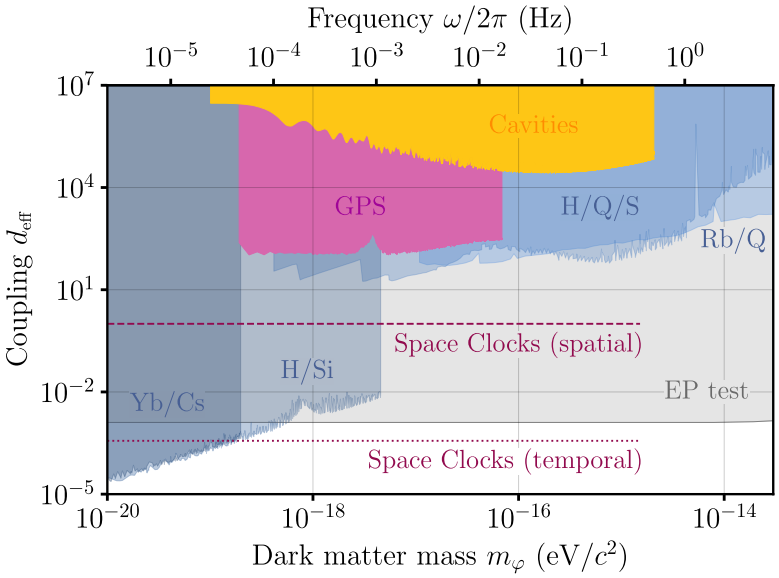

Figure 3.13: Constraints on effective couplings d_{eff} involving d_{m_e} (95% confidence level) as a function of the dark matter mass m_ϕ and corresponding oscillation frequency $\omega/2\pi$. Shown in blue are existing constraints on $|d_{m_e} - d_g|$ from local clock and oscillator comparisons (Yb/Cs [117], H/Si [109], H/Quartz/Sapphire [154], and Rb/Quartz [122]; the Ref. [154] constraint has been rescaled by 3.0 to account for the stochasticity [95], which is already included in the other constraints). The gray band shows constraints on $|d_{m_e} - d_g|$ from equivalence principle (EP) tests by the MICROSCOPE mission [7, 114, 115]. The constraints from this work are the only constraints on d_{m_e} alone in this mass range.

As a complementary example, we also consider data from the Rb microwave clocks on board the GPS satellites, as compared to an Earth-based hydrogen maser. The GPS data have previously been used for dark matter and cosmic field searches [10, 155, 156]. The GPS comparisons are made with a one-way microwave link, and the type of noise cancellation as employed in the fiber network is not possible. Therefore, this search is sensitive to the phase difference caused by the signal time delay:

$$\frac{\Delta(\nu_A/\nu_B)}{\nu_A/\nu_B} = \varphi_0 \, d_{\text{eff}}^{\text{mw}} \, \frac{\omega D}{c} \, \sin(\omega t). \tag{3.42}$$

The GPS constellation consists of approximately 30 satellites in orbit at a radius of $D \approx 26\,000$ km. Signals driven by an onboard Rb microwave atomic clock are broadcast from each of the satellites. The time differences between the satellite clocks and a ground-based hydrogen maser are determined, and made publicly available [157, 158]. From these, we derive the fractional frequency differences averaged over the 30 s sampling period [155].

https://doi.org/10.7795/110.20260227

Relativistic Doppler shift effects cause periodic variations in the clock timings that oscillate at the $\sim 12\,\mathrm{hr}$ orbital period. These are modeled and removed [159]. Due to the imperfect nature of the modeling, residual effects are present in the data, and consequently, we do not search for oscillations at or below this frequency.

Since the scalar field is coherent across the network, and the time delay between each of the satellites and the Earth-based receiver station is roughly the same, the dark matter signal should be approximately equal for each GPS satellite clock. Therefore, for each day of data, we form a weighted average of the frequency comparisons for each of the Rb satellite clocks in the network, compared to the common ground-based H-maser. We then form the amplitude spectrum for each day of data. Since we only use clocks for which there are no missing data points, we use the standard Fourier method. We repeat the process for the most recent 34 weeks of data (up to May 11, 2024), resulting in 238 spectra. We take the average as the best-fit amplitude spectrum, and use the spread in amplitudes at each frequency to determine the maximum spectrum at the 95% confidence level. Due to the large number of spectra, this is very close to the average, as shown in Figure 3.12. We have made our code for this analysis public [151].

There are several large peaks in the GPS amplitude spectrum, which are likely caused by the satellite operation and signal processing. Without a full noise model for these clocks, we cannot define a detection threshold. From the analysis, we place constraints on the combination of couplings in Equation 3.16. By combining with existing constraints on $|d_e|$ [40, 117, 122, 152, 153], $|d_{m_e} - d_g|$ [109, 117, 122, 154], and $|d_{m_q} - d_g|$ [93, 117], we constrain d_{m_e} alone. The constraints at the 95% confidence level are shown in Figure 3.13.

In Figure 3.13, we also present projections of future sensitivities. The "Space Clocks" projections are based on a future network of clocks showing white frequency noise with an amplitude of 10^{-18}, and a separation equal to the GPS diameter [92, 160–163]. We show this both for the spatial term [Equation 3.40], and the temporal term [Equation 3.42], which would apply only if the noise cancellation does not remove the time-delay contribution signal.

In conclusion, we present a method to search for ultralight dark matter with space-time separated atomic clocks and cavities. We demonstrate this method by searching for oscillations with periods ranging from $2\,\mathrm{s}$ to $10^5\,\mathrm{s}$ using frequency ratio measurements of lasers stabilized to optical cavities, and the microwave clocks on board the GPS satellites. We placed constraints on the coupling of scalar dark matter to

https://doi.org/10.7795/110.20260227

electrons in the mass range ($10^{-19} - 2\times10^{-15}\,\mathrm{eV}/c^2$.) These are the only constraints on d_{m_e} alone at low frequencies $< 1\,\mathrm{Hz}$.

Searching for ultralight dark matter with space-time separated oscillators uniquely enables probing the spatial fluctuations of scalar dark matter, and features key signatures to distinguish a dark matter signal from a spurious signal in case of a detection, namely the scaling with the effective distance, and the sidereal modulation. The method also circumvents the need for the oscillators to feature a differential sensitivity to the considered dark matter coupling. Without the need to optimize for large differential sensitivities, future comparisons between space-time separated oscillators are free to focus on utilizing the full potential of the available sensor types to investigate different frequency ranges. This is particularly relevant for future measurement campaigns involving long fiber links, and for future fundamental physics investigations in space.

3.6 Summary and outlook

This chapter has presented different aspects of searches for ultralight dark matter with optical frequency comparisons. In section 3.3 we leveraged the high fine-structure sensitivity of the $^{171}\mathrm{Yb}^+$ E3 transition in two optical clock comparisons. An analysis of the resulting data for oscillations acts as a broadband search for a coupling d_e of scalar ultralight dark matter to photons. In the absence of statistically significant oscillations, we were able to place improved bounds on the strength of this coupling over a wide range of possible dark matter masses.

Section 3.4 demonstrates how optical atomic clock comparisons are sensitive to nuclear UDM couplings via the mass and field shifts, using the $\nu_{\mathrm{E3}}/\nu_{\mathrm{E2}}$ frequency ratio as an example. Even though the corresponding sensitivities are three orders of magnitude smaller than that to variations of the fine-structure constant, the obtained limits are competitive with those from comparisons of microwave clocks based on hyperfine transitions.

In section 3.5 we have investigated how space- and time-separation of the two oscillators in an optical frequency comparison can retain sensitivity to dark matter couplings even for equal oscillators. As an example, we have presented an analysis of available data from the comparison of lasers locked to ultrastable cavities across the European fiber network, and from microwave clocks aboard the GPS satellites.

https://doi.org/10.7795/110.20260227

This complementary approach allows accessing unique combinations of dark matter couplings, and in the case of detection, experimental signatures allowing to distinguish noise from a dark matter signal.

How can we improve our experiments to perform even better UDM searches in the future? One answer is to use clocks based on transitions with increased sensitivity to the constant under investigation, since the sensitivity contributes linearly to the coupling strength that can be probed. Regarding α-sensitivity, an optical lattice clock based on neutral ytterbium [58], as well as certain species of highly charged ions [120, 121] would be advantageous. A potential future nuclear optical clock based on thorium [118, 119, 164, 165], would offer even higher sensitivity, and could potentially investigate a coupling several orders of magnitude below the limits presented here.

For a given sensitivity, the amplitude level of the measurement noise at a specific frequency limits the search. This relates to the properties of the measurement: The measurement instability determines what amplitude levels can be probed for a given averaging time, with a $1/\sqrt{\tau}$ scaling in the case of white noise. What level can ultimately be reached depends on the long-term stability, or reproducibility, of the involved systems. While the systematic uncertainty of a clock may be an indicator of its expected long-term stability, we have shown that in the case of the Yb1 clock operating on the E2 transition a reproducibility well below the systematic uncertainty is obtained. We will see in chapter 5 that the same holds true for the Yb1 clock operating on the E3 transition. Although it is harder to quantify, experimental robustness is also an important factor, not just because a lack of it might cause characteristic gaps in the data, e.g. over night, but also through the feasibility to accumulate a large amount of data with reasonable effort and within an accessible time frame.

The investigated range of dark matter masses was limited by the $\approx 200\,\mathrm{s}$ time constant of the servo to below $2 \times 10^{-17}\,\mathrm{eV}$ in our optical frequency comparisons. Slightly higher masses can be probed by comparing other types of oscillators, e.g. optical cavities. It would be interesting, however, to apply the high α-sensitivity of the E3 transition to larger dark matter masses around $10^{-16}\,\mathrm{eV}/c^2$ and beyond. To achieve this without being limited by the typical servo time constants in optical clocks, dynamical decoupling sequences, which offer increased sensitivity to variations at particular frequencies, specifically frequencies even larger than the inverse total interrogation time, could be employed [109, 166, 167].

https://doi.org/10.7795/110.20260227

To utilize the high α-sensitivity of the E3 transitions for improved measurements in the current frequency range, one approach could be to perform a yearslong optical frequency comparison between a clock based on the $^{171}Yb^{+}$ E3 transition, and a suitable partner clock that is more stable than that based on the E2 transition. Furthermore, the instability of the clock running on the E3 transition could be improved, for example with longer coherent interrogation times or simultaneous interrogation of multiple ions. First experimental steps towards these goals were taken in the scope of this thesis with the construction of a new optical clock apparatus that combines $^{171}Yb^{+}$ and $^{88}Sr^{+}$ ions.

https://doi.org/10.7795/110.20260227

https://doi.org/10.7795/110.20260227

4 A new optical clock experiment for $^{171}Yb^{+}$ and $^{88}Sr^{+}$ ions

We have seen in previous chapters that the electric quadrupole, or E2, transition in $^{171}Yb^{+}$ can be used to characterize shift effects for the clock based on the less sensitive electric octupole, or E3, transition, and also as a suitable partner for optical frequency comparisons with high differential α-sensitivity. The "toolbox" of available transitions can be extended further by co-trapping $^{171}Yb^{+}$ ions with a different ion species that offers a clock transition with useful complementary characteristics. The $^{2}S_{1/2} \rightarrow {}^{2}D_{5/2}$ electric quadrupole transition in $^{88}Sr^{+}$ is a particularly attractive candidate for several reasons:

First, the differential static scalar polarizability, which determines the sensitivity to thermal radiation, is very well known for this transition [168, 169]. In $^{171}Yb^{+}$, limited knowledge of the same atomic parameter corresponds to a fractional frequency uncertainty of 1.3×10^{-18} for a clock operating on the E3 transition at room temperature [22]. By subjecting both ion species to the same perturbing radiation, for example infrared laser light, and measuring the effect on the respective clock transitions, the 45 times lower uncertainty of the polarizability in $^{88}Sr^{+}$ can be transferred to $^{171}Yb^{+}$. This will enable the possibility of room-temperature $^{171}Yb^{+}$ ion clocks with systematic uncertainties well below 1×10^{-18}.

Second, the 674 nm wavelength used to drive this transition in $^{88}Sr^{+}$ is close to the magic wavelength of the $^{171}Yb^{+}$ E3 transition [30]. Therefore, sideband cooling of a $^{88}Sr^{+}$ ancillary ion could be performed during clock operation on a co-trapped $^{171}Yb^{+}$ ion, without the clock operating on the E3 transition being limited by the associated light shift. Then, interrogation of the sympathetically cooled $^{171}Yb^{+}$ ion is no longer compromised by motional heating, enabling extended coherent interrogation times on the E3 transition.

https://doi.org/10.7795/110.20260227

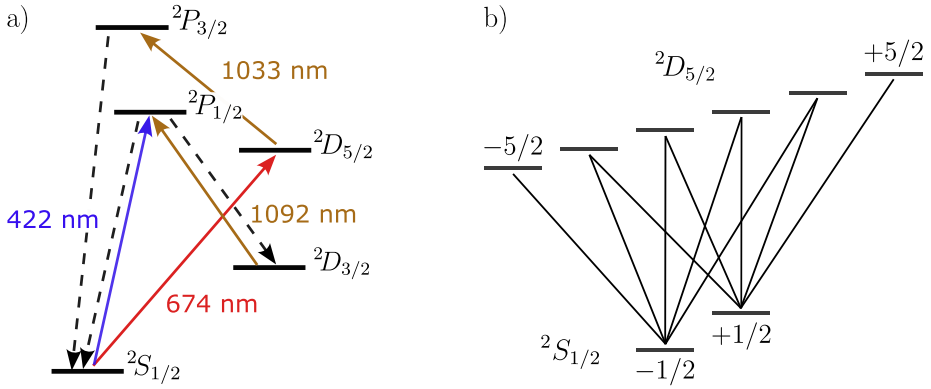

Figure 4.1: Relevant level scheme of $^{88}Sr^+$. a) An electric dipole transition at 422 nm is used for Doppler cooling and detection. An electric quadrupole transition at 674 nm can be used for precision spectroscopy, as well as for resolved sideband cooling. A repump transition at 1092 nm facilitates closed-cycle Doppler cooling. Another repump transition at 1033 nm is used to depopulate the $^2D_{5/2}$ excited state. b) The $^2S_{1/2} \rightarrow {}^2D_{5/2}$ clock transition is split into ten Zeeman components in an external magnetic field.

Finally, we have seen in chapter 2 that the instability of a single-ion $^{171}Yb^+$ clock running on the E2 transition is limited by the short (53 ms [51]) excited-state lifetime. And while interleaved interrogation of both the E2 and E3 transitions in a single $^{171}Yb^+$ ion offers many advantages and has proven to be extremely robust and long-term stable, the reduced duty cycle of each clock further deteriorates the measurement instability of the frequency ratio. A frequency comparison between a clock operating on the $^{88}Sr^+$ $^2S_{1/2} \rightarrow {}^2D_{5/2}$ transition and a clock running on the $^{171}Yb^+$ E3 transition, both realized within the same experimental apparatus, might offer similar advantages to interleaved interrogation, but vastly improved instability. The sensitivity of the $^{88}Sr^+$ clock frequency ν_{Sr^+} to variations of the fine-structure constant is $K_\alpha = 0.43$ [27], yielding a differential sensitivity $\Delta K_\alpha = 6.38$ for the frequency ratio ν_{Sr^+}/ν_{E3}, only slightly smaller than the differential sensitivity of 6.95 for ν_{E3}/ν_{E2}. This makes improved searches for variations of the fine-structure constant with this frequency ratio feasible.

With this in mind, let's take a first look at some of the properties of $^{88}Sr^+$ ions. The relevant level scheme of $^{88}Sr^+$ is depicted in Figure 4.1. An electric dipole transition at 422 nm can be used for Doppler cooling and detection. A repump transition at 1092 nm facilitates closed-cycle Doppler cooling, and another one at 1033 nm is used to depopulate the $^2D_{5/2}$ state after successful clock excitation [170]. In contrast to $^{171}Yb^+$, with its $m_F = 0 \rightarrow m_F = 0$ transitions, $^{88}Sr^+$ offers no first-order Zeeman insensitive transitions. Instead, an external magnetic field splits the

https://doi.org/10.7795/110.20260227

$^2S_{1/2} \rightarrow {}^2D_{5/2}$ clock transition into ten first-order Zeeman sensitive components. The $^2D_{5/2}$ excited state has a natural lifetime of 391 ms [171], which allows for longer coherent interrogation times than that of $^{171}Yb^+$ E2 transition, but without the technical challenges associated with clock operation on the ultra-narrow E3 transition.

A first dual-species optical clock experiment co-trapping $^{88}Sr^+$ and $^{171}Yb^+$ ions in a linear ion trap has previously been set up in our group, with first results reported in [43]. That experimental apparatus is currently used to improve the knowledge of the dynamical polarizability in $^{171}Yb^+$, as outlined above, and the results will be reported in detail in Martin Steinel's dissertation, and corresponding publications. Clock performance in this system is limited by the prototype ion trap made from printed-circuit polymer material (Rogers 4350B). In the scope of this thesis, a second-generation dual-species apparatus was developed. The biggest improvements are the high-performance ion trap constructed from alumium-nitride wafers, increased optical access, and the implementation of camera-based, ion-resolved state detection. This chapter describes and characterizes the newly constructed experimental apparatus, setting the stage for the results obtained in chapter 5, as well as future measurements involving this system.

A first overview of key experimental components is provided in Figure 4.2, with further details discussed throughout the remainder of this chapter: Section 4.1 contains information on the vacuum system and a characterization of the residual background pressure based on the reordering of a mixed-species ion crystal. Section 4.2 describes the intra-vacuum assembly including the ion trap, the electrical connections, and the atom sources. Section 4.3 gives an overview over the optical access provided by the system, as well as current and planned laser beam paths for both ion species. Section 4.4 describes and characterizes an imaging system that is designed to combine the fluorescence of both ion species onto a single EMCCD camera for site-resolved state detection in single- or mixed-species ion crystals. Section 4.5 concerns the magnetic field control, including the coil geometry and magnetic field stability. Section 4.6 contains measurements characterizing the relevant properties of the ion trap, including excess micromotion, ion heating, and the oscillating magnetic field from the trap drive. Section 4.7 discusses temperature measurements around the ion trap and the associated uncertainty of the temperature at the position of the ions. This is important to characterize the frequency shift from thermal radiation. All ion-based measurements throughout were performed with $^{88}Sr^+$, as trapping of $^{171}Yb^+$ has not yet been attempted in this apparatus.

https://doi.org/10.7795/110.20260227

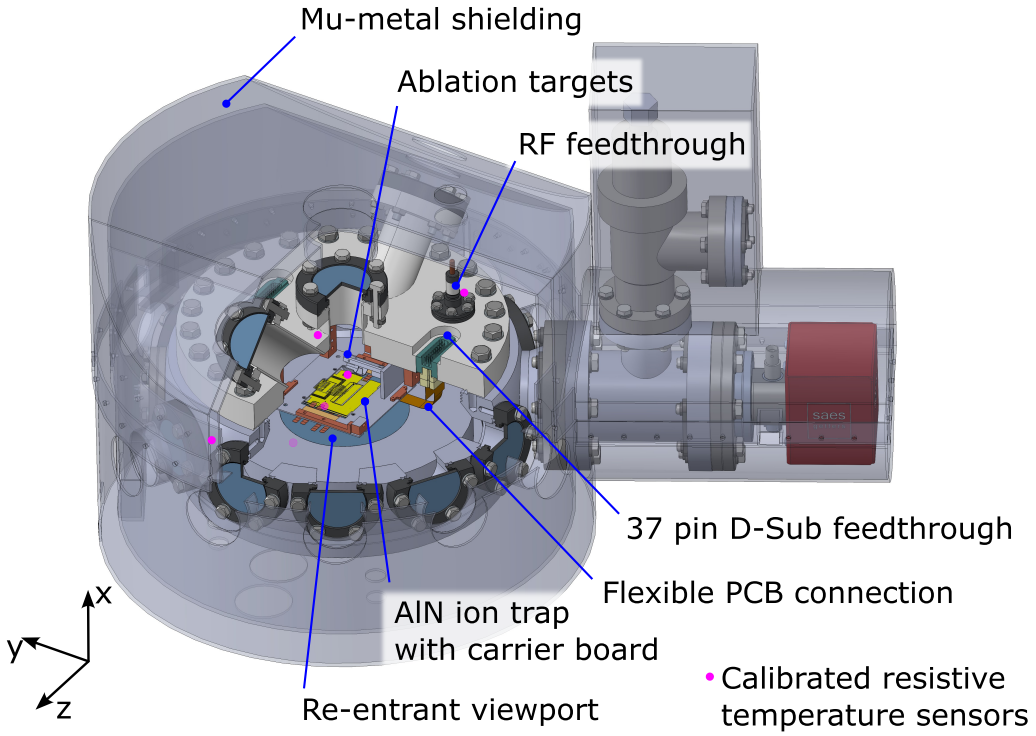

Figure 4.2: Overview over key experimental components. The vacuum system is constructed from conflat components which are almost exclusively made of titanium, with the exception of the valve and pumps, which are made of stainless steel. All intra-vacuum components are assembled on a large DN200 CF flange with a coaxial feedthrough for the radiofrequency (RF) trap drive and two 37 pin D-Sub feedthroughs for DC voltages and temperature readout. A segmented linear ion trap made from aluminum nitride (AlN) wafers with structured gold coatings is glued to a ceramic carrier board sitting on four feet machined from a copper alloy. Two targets for laser ablation are mounted with titanium components and act as atom sources. A large reentrant viewport provides high-NA optical access. Calibrated temperature sensors are integrated on two of the trap wafers and distributed on the outside of the vacuum chamber. Two 3 mm thick layers of mu-metal provide magnetic shielding.

https://doi.org/10.7795/110.20260227

4.1 Vacuum system and residual pressure

Great care is taken to avoid the use of materials that can be magnetized in the vacuum system. Except for the valve and the pumps, the vacuum components are made from titanium, with most pieces being custom designs. All bolts are grade V titanium. Standard ConFlat (CF) flanges and copper gaskets are used throughout. The vacuum chamber consists of a DN200CF (10 in) spherical dodecahedron with 11 DN40CF ports and one pumping port with a DN63CF flange. Connected to the pumping port is a custom T-piece offering access to a DN40CF standard stainless-steel all-metal angle valve for closing off the system after initial pumping, and an ion-getter pump (SAES NexTorr Z200). The port opposite the pumping port holds an additional small getter pump (SAES CapaciTorr Z16). All viewports are fused silica with titanium flanges and a custom antireflection coating for all wavelengths used in $^{171}Yb^+$ or $^{88}Sr^+$. The lowest wavelength is 370 nm, used for Doppler cooling of $^{171}Yb^+$, and the highest is 1092 nm, used for repumping in $^{88}Sr^+$. A custom DN200CF re-entrant viewport offers high-NA optical access for imaging through a 6.4 mm thick window of 68 mm diameter, and 8 threaded holes on its outside are used to mount the vacuum system on the optical table. All intra-vacuum components are mounted to the inside of a single DN200CF flange via threaded holes. Welded to this flange are three DN40CF half-nipples to provide optical access, as well as two non-magnetic titanium 37-pin Sub-D electrical feedthroughs (Allectra 218-D37-TI). A coaxial feedthrough with a single copper pin in a DN16CF titanium flange (Kurt J Lesker EFT-SPL407) is used for the RF voltage supplied to the ion trap.

Vacuum components were assembled as supplied by the companies, i.e. without further cleaning. Intra-vacuum components were largely machined in-house and cleaned in an ultrasonic bath using first acetone, then isopropanol, and finally de-ionized water. Since the vacuum system contains only small amounts of stainless steel, no specific measures to reduce hydrogen outgassing were performed. After assembly of the full system including all viewports and intra-vacuum components, the system was baked once to about 140 °C for about two weeks in an oven while being pumped with a turbomolecular pump. During cooldown of the system after baking and pump activation, the controller of the ion-getter pump showed its lowest current reading already at an elevated temperature of about 50 °C, indicating a final pressure below 1 nPa at the position of the pump.

To investigate the background pressure at the position of the trapped ions, we

https://doi.org/10.7795/110.20260227

measure the reorder rate Γ of a linear ion crystal consisting of $^{88}Sr^+$ ions as well as another Sr isotope, most likely $^{87}Sr^+$ or $^{86}Sr^+$, which does not fluoresce at our usual laser wavelengths. To this end, we continuously cool the $^{88}Sr^+$ ions on the $^2S_{1/2} \rightarrow {}^2P_{1/2}$ transition and track their centroid positions using images taken with an EMCCD at an exposure time of 100 ms over several hours. We determine reorder events in a time series of the bright ions' position sampled at 1 s by counting the number of times any of the recorded z-positions change by more than 7 pixels.

We need to account for the fact that not every crystal melting is detected as a reordering:

$$\Gamma = \Gamma_{\mathrm{det}} \frac{n_{\mathrm{tot}}}{n_{\mathrm{vis}}}, \tag{4.1}$$

where Γ_{det} is the detected reorder rate, and Γ is the corrected reorder rate. Under the assumption that all crystal configurations are equally likely, one can determine the ratio of total reordering events to detected events, $n_{\mathrm{tot}}/n_{\mathrm{vis}}$, with combinatorics. In the case of two ions the probability would be 50% to end up in the original configuration, so only half of the melting events would be detected. More generally, for chains of N ions, with M bright and $N-M$ dark, there are $N!$ initial configurations, and $N!$ possible reorderings per configuration. Thus the number of total possible reorderings is $n_{\mathrm{tot}} = (N!)^2$. The number of visible reorderings is $n_{\mathrm{vis}} = N!(N! - k)$, where k is the number of invisible reorderings of each of the initial $N!$ configurations. k is calculated from generating all possible reorderings and counting the number of indistinguishable reorderings. This yields a corrected reorder rate of

$$\Gamma = \Gamma_{\mathrm{det}} \frac{1}{N\left(1 - \frac{M!(N-M)!}{N!}\right)}. \tag{4.2}$$

We perform the measurement with low axial confinement and calculate the two-ion reordering energy barrier following [172] to be below $k_B \times 1\,\mathrm{K}$. This means that only a neglegible fraction of collisions with the room-temperature background gas does not provide enough energy for crystal reordering. In a 54 000 s long measurement with a linear crystal of four bright and two dark ions, we detect a total of 349 reordering events. A fit to the exponential distribution of the time between collisions yields a corrected reorder rate of $\Gamma = 1.13(8) \times 10^{-3}$/s/ion. A second, shorter measurement with one bright and two dark ions yields a corrected rate of $\Gamma = 1.5(3) \times 10^{-3}$/s/ion. The weighted mean is $\Gamma = 1.16(7) \times 10^{-3}$/s/ion.

Following [173], we estimate the background pressure p corresponding to the mea-

https://doi.org/10.7795/110.20260227

sured re-order rate: The pressure is obtained from the ideal gas law $p = \rho k_B T$ by eliminating the density via the Langevin rate $\gamma_L = 2\pi\rho\sqrt{C_4/\mu}$ with μ the reduced mass between the trapped ion and the average mass of the background gas, and where the C_4 parameter can be obtained from the static polarizability of the background gas. This yields

$$p = \frac{\Gamma k_B T \sqrt{\mu}}{2\pi\sqrt{C_4}} \tag{4.3}$$

We estimate the pressure assuming the background gas is air ($C_4 \approx 2.65 \times 10^{-57}\mathrm{Jm}^4$, $\mu \approx 3.6 \times 10^{-26}\,\mathrm{kg}$), and obtain $p \approx 2.8\,\mathrm{nPa}$. Alternatively, the background gas might consist of molecular hydrogen ($C_4 = 9.16 \times 10^{-59}\mathrm{Jm}^4$, $\mu \approx 3.3 \times 10^{-27}\,\mathrm{kg}$), for which the observed collision rate would yield a pressure of $p \approx 4.5\,\mathrm{nPa}$. Without knowledge of the background gas composition, these values can only serve as a rough estimate for the true background pressure. In particular, there is a possibility of significant outgassing from the solder or glue used on the ion trap.

4.2 Intra-vacuum assembly

To ease the assembly process, all intra-vacuum components were assembled onto the same DN200CF flange, which also contains all electrical feedthroughs. The segmented linear ion trap is based on the design in [174]. It consists of four precision machined aluminium-nitride (AlN) wafers with structured gold coating and was assembled largely following the procedures developed for this trap design in the group of Prof. Mehlstäubler, see e.g. [175] for details. A picture of the final intra-vacuum assembly is shown in Figure 4.3. Low-pass filtering of the supplied DC voltages with a cutoff-frequency of 1.6 kHz is implemented via SMD components soldered directly onto the trap wafers. The two inner wafers additionally feature calibrated Pt1000 sensors, which are shielded from RF-pickoff with capacitors. The ion trap is glued onto an AlN carrier board, which is mounted to the flange with four feet machined from Copper Chromium Zirconium. RF and ground connections between the trap and the carrier board are made with 5 mm wide and 0.1 mm thick copper strips which are soldered onto the trap chips by hand. From there, a broad, laser-cut copper strip connects the RF side of the carrier board to the RF feedthrough, while a solid copper piece connects the ground side to the vacuum chamber. All other electrical connections from the trap onto the carrier board are made with wirebonds. In total there are 40 independent connections for DC voltages (10 trap segments × 4

https://doi.org/10.7795/110.20260227

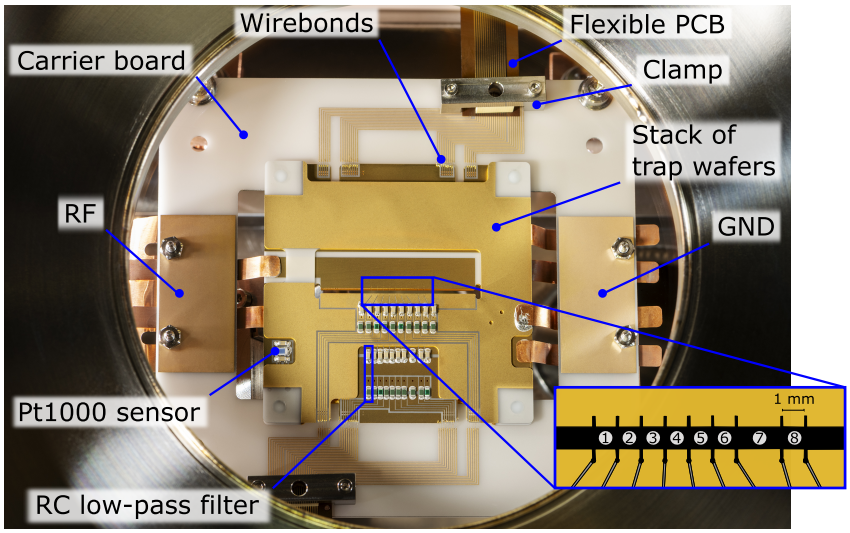

Figure 4.3: Photograph of ion-trap assembly taken through the re-entrant viewport. The linear, segmented ion trap consists of four precision machined aluminium-nitride (AlN) wafers with structured gold coating. The ion trap is glued onto an AlN carrier board. The connections for radiofrequency (RF)-voltages and ground (GND) are made via copper strips. All other connections are made with wirebonds, and then connected via two flexible PCB ribbons to UHV-compatible Sub-D connectors at the corresponding feedthroughs. All DC voltages applied to the trap are low-pass filtered with RC filters soldered onto the trap chips. Two of the four trap chips additionally carry calibrated Pt1000 resistive temperature sensors. Inset: The segmented trap offers eight zones for ion trapping and an additional two endcap segments.

trap wafers) + 8 connections for the two four-wire temperature measurements. The connection to the pins of the two 39-pin Sub-D feedthroughs are made with flexible PCB ribbons, which are pressure-connected to the carrier board with a clamp assembly. On the other side, copper pins are soldered onto both sides of the flexible PCB, which are in turn crimped to nonmagnetic single-pin push-on connectors. The individual connectors are filled into a ceramic insulation piece matching the D-Sub geometry of the feedthrough.

The assembly contains one target each to generate Yb and Sr atoms with laser ablation. For Yb, a piece of solid ytterbium is used, while for Sr we used single-crystal $SrTiO_3$ based on the results in [176], which found reliable loading of Sr^{+} over many iterations with this target compared to other materials. Indeed, we obtained robust loading of $^{88}Sr^{+}$ without ever having to move the position of the ablation laser on the target during the year the experiment has been in operation. Figure 4.4 shows a schematic overview over the atom source geometry. All components used for mounting the ablation targets are made from titanium. The base plate of the

https://doi.org/10.7795/110.20260227

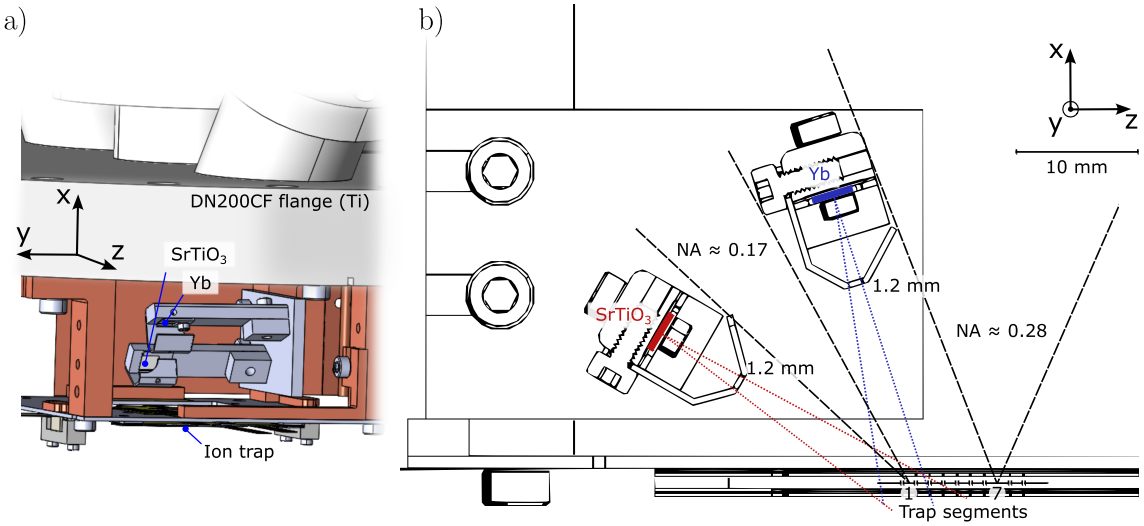

Figure 4.4: Overview over atom source geometry. a) Model of intra-vacuum assembly with laser ablation targets and mounting components, oriented as in the final assembly with gravity pointing downwards along the $-x$-direction. b) Cut through plane of the ions illustrating geometric considerations. The ablation targets and their apertures are aligned for loading into trap segment 1, while the longer "spectroscopy" trap segment 7 is shielded from atom flux. Care is taken not to limit the optical access for these two segments. Laser beams for photo-ionization are aligned to segment 1 along the $+y$-direction, orthogonal to the directions of atom flux.

assembly determines the alignment with respect to the trap. The ablation targets are positioned for maximum atom flux towards trap segment 1. Laser beams for photo-ionization enter this segment orthogonal to the atom flux in order to avoid large Doppler shifts. Thin titanium sheets with apertures of 1.2 mm diameter shield the other trap segments from atom deposition. In particular, segment 7, which is twice as long as the other segments to avoid distortion of the RF field from edge effects, is as far away from the segment chosen for ion loading as possible. Care is taken to preserve the optical access for these two segments.

4.3 Optical access and laser beam paths

The optical setups around the vacuum chamber are organized on three separate levels, with the complete apparatus designed to take up half of a standard optical table: The chamber with the mu-metal shielding is sitting on titanium feet, elevated about 20 cm from a 120 cm x 120 cm honeycomb breadboard which is used for optical access from the bottom via the re-entrant viewport. A second honeycomb breadboard

https://doi.org/10.7795/110.20260227

of similar size sits about 16 cm above the first one and features a custom keyhole cutout for the chamber and magnetic shielding. On top of this central breadboard in turn an aluminium breadboard is mounted vertically for optical access via the three top viewports.

The central horizontal breadboard offers optical access via ten DN40CF viewports. A schematic overview over laser beams on this breadboard is shown in Figure 4.5. The geometry of the vacuum system was chosen specifically to maximize optical access given the constraints of the ion trap design: The four spacers between the individual trap wafers are placed at the corners of the square trap chips, blocking access at 45° with respect to the trap axis, while the dodecahedral chamber offers optical access under multiples of 30°. All depicted beams pass horizontally through the trap center, except for the laser ablation beams, which are oriented upwards onto their respective targets. The ablation laser (CNI Laser EL-532), which features a repetition rate of 10 kHz, pulse length of 2 ns, and pulse energy of 150 µJ, is mounted directly onto the optical breadboard. An automated flip mirror allows switching between the respective beam paths for the two atom species. All other laser light is brought onto the main optical table from separate light distribution breadboards with polarization-maintaining optical fibres. The vertical NA of the beams passing through the trap is limited by the 50 mm × 50 mm trap chips to at most NA ≈ 0.02. Laser beams on this breadboard used for clock operation are planned such that they fulfill the respective selection rules for a single, common magnetic field orientation of $\theta \approx 54.7°$ with respect to the trap axis in the horizontal, which suppresses the variation of the quadrupole shift along chains of ions (c.f subsection 5.2.3). Beams for optical repumping from excited states are set up such that they can be used in all trap segments. Beams for photoionization are aligned to trap segment 1.

Figure 4.6 shows a vertical cut through the system, with a schematic depiction of relevant laser beam paths. The central top viewport allows an NA of about 0.2 for the central trap segments, and might be used for single-ion addressing in the future. The two ports at 45° offer a NA of 0.09, limited by the distance of the DN40CF viewports. They are used for a variety of cooling beams, since these directions have good overlap with all trap axes. Some of the cooling beams feature an elliptical cross-section for homogeneous addressing of ion chains. In particular, the 674 nm beam used for fast optical pumping and sideband cooling of $^{88}Sr^+$ ions is expanded strongly orthogonal to the trap axis before focusing to enable both high Rabi frequencies and relatively homogeneous addressing of up to 100 µm long ion chains. The angle of its linear polarization is optimized experimentally to drive transitions with $\Delta m = 2$ at

https://doi.org/10.7795/110.20260227

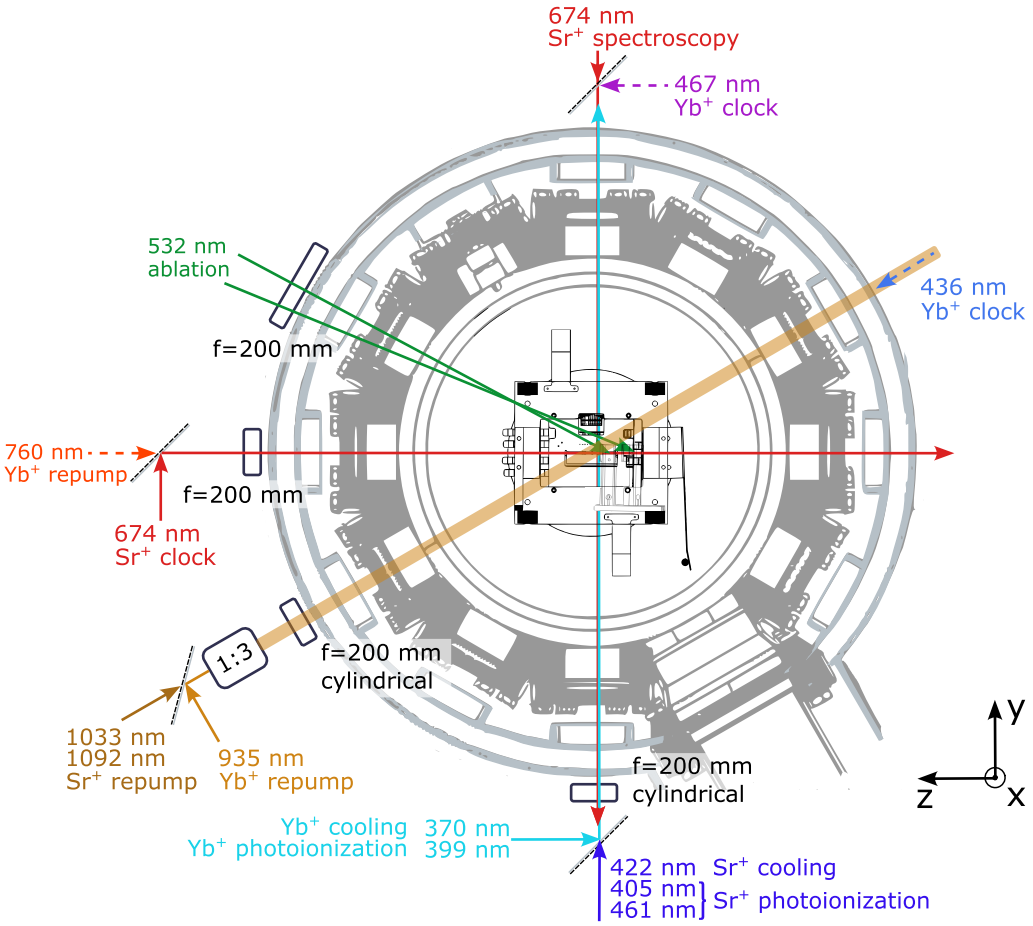

Figure 4.5: Overview over beam geometry in the horizontal plane. The trap axis is aligned along the z-direction. Optical access is available in ten directions. The numerical aperture for addressing trapped ions from any of these directions is limited by the trap chips to about NA=0.02 in the vertical (x) direction. Solid lines depict implemented beam paths, while dashed lines stand for planned beams. All laser light except for the laser ablation beams is brought onto the main optical table with polarization-maintaining optical fibres. Laser light of different wavelengths shown in the same color originates from the same fiber. Otherwise, beams of different wavelength are overlapped with dichroic long-pass filters. The depicted cylindrical lenses are focusing in the vertical direction to enable homogeneous addressing of ion chains.

https://doi.org/10.7795/110.20260227

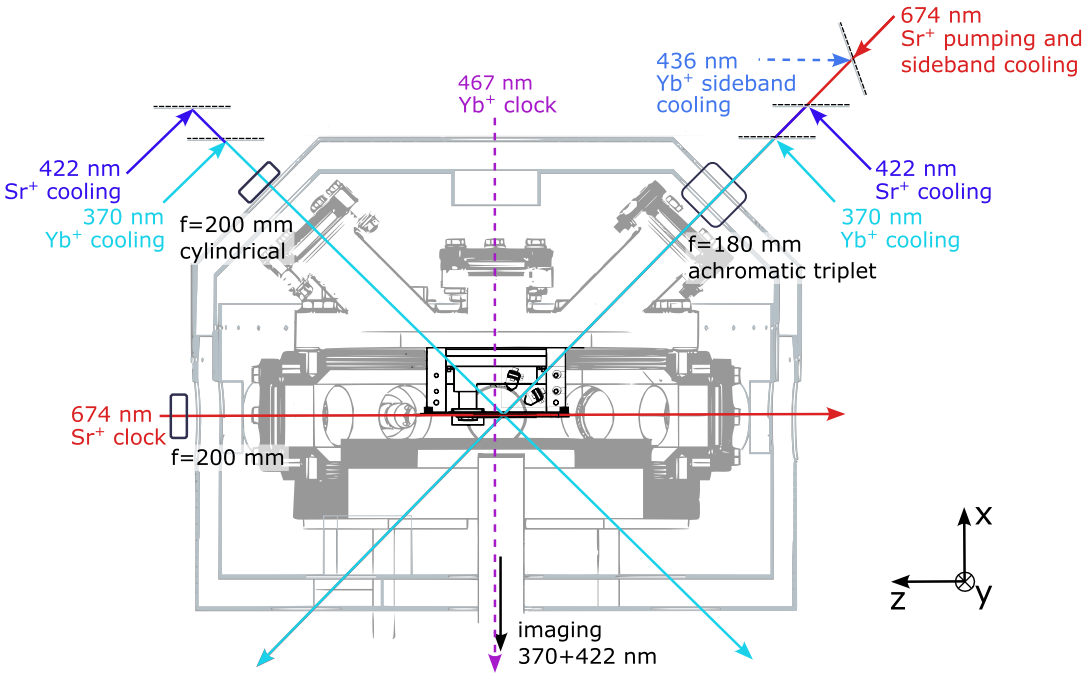

Figure 4.6: Overview over beam geometry in the vertical plane. Solid lines depict implemented beam paths, while dashed lines stand for planned beams. The Doppler cooling beams coming from the left side are round before being focused in only the y-direction with a cylindrical lens to enable homogeneous addressing of ion chains, which are oriented along the z-axis. The beams coming from the right side are focused in both directions. The 674 nm beam used for pumping and sideband cooling is expanded in the y-direction before being focused to achieve high Rabi frequencies that are homogeneous for chains of ions. The top central port features an NA of about 0.2. Beams entering the chamber from any of the top three viewports exit via the large-reentrant viewport on the bottom, which also features high-NA optical access for imaging. Sending in beams from the bottom instead of the top is also possible.

the typical magnetic field direction. For both ion species, three mutually orthogonal Doppler cooling beams are implemented, which enables convenient determination of all micromotion components via photon-correlation.

The bottom breadboard currently holds only the imaging system, which is described in section 4.4, but optics for additional laser beams at 45° with respect to the horizontal may be set up there in the future, as well as optics for fibre length stabilization of a future vertical 467 nm clock beam that passes the first lenses of the imaging system before being separated from the ion fluorescence with a dichroic beamsplitter. All in all, much of the optical access the system offers is currently still unused. This is by design, to enable flexible new optical setups for a variety of future experiments involving both ion species as well as multiple trap segments.

https://doi.org/10.7795/110.20260227

4.4 Imaging and state detection

An optical system for collection and imaging of both the 370 nm fluorescence from $^{171}Yb^{+}$ and the 422 nm fluorescence from $^{88}Sr^{+}$ ions was constructed. Compared to other experiments in our group, which all rely on photomultiplier tubes (PMTs) for state detection, here, both species are imaged onto a shared EMCCD camera which can be used for site-resolved state-detection when working with chains of multiple ions. Additionally, the fluorescence from both species can be sent to individual PMTs.

The entire imaging system is constructed from standard off-the-shelf optical components, and mostly standard SM1 optomechanical components. An overview and description is provided in Figure 4.7. Though a higher NA would be possible with larger diameter lenses, we chose a 25 mm diameter as not to block laser beams passing the ion trap under 45° (c.f. Figure 4.6). The imaging system is set up in two stages, to provide the option of spatial filtering in the first focus for each ion species. Since the system is not designed to be achromatic, the 422 nm and 370 nm fluorescence are split with a dichroic longpass filter and pass independent second imaging stages before being recombined. The fluorescence can be sent to either the shared EMCCD camera or to individual photomultiplier tubes (Hamamatsu H10682-210//001) for each species, depending on the settings of two electronically controlled flip mirrors.

The first imaging stage offers a magnification of about 15 for 370 nm and 18 for 422 nm, and the difference is largely compensated by slightly different magnifications between two and three in the second stage. We obtain an overall magnification of 38 for 422 nm and 41 for 370 nm. This was measured in a test setup imaging the transmission of 370 nm and 422 nm light through a 1 µm pinhole: A small change in the position of the pinhole and the first-stage imaging components, as indicated by the reading of a micrometer screw, was compared to the distance the image moved on the camera chip for the respective wavelength. The EMCCD camera (Princeton Instruments ProEM HS) has 512×512 pixels of size $16\,\mu m \times 16\,\mu m$, meaning we can image about $250\,\mu m \times 250\,\mu m$ onto the camera chip with this magnification.

We do not expect diffraction limited performance with this imaging system, since the standard asphere was designed without taking into account the vacuum window. Instead, our design objectives were to image both species with a similar magnification and resolution, to be able to resolve individual ions in a chain with negligible

https://doi.org/10.7795/110.20260227

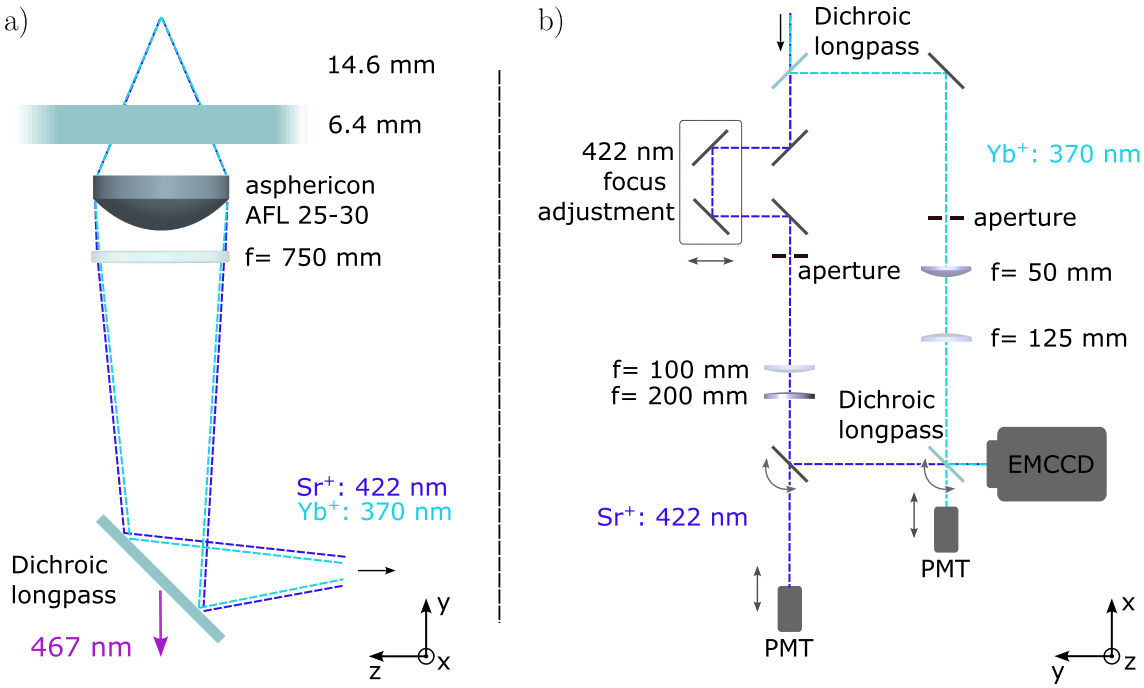

Figure 4.7: Overview over dual-species imaging setup (not to scale). All lenses have a 25 mm diameter. a) First-stage imaging. The ions sit 14.6 mm away from the 6.4 mm thick fused silica viewport. A standard asphere (asphericon AFL 25-30, NA=0.38) is used as a first lens, followed by a standard spherical singlet lens with 750 mm nominal focal length. A dichroic longpass filter reflects the fluorescence of both species, but transmitts 476 nm light used for excitation of the $^{171}Yb^{+}$ E3 transition, which might prove useful in the future for individual addressing of ions at this wavelength. The optical components can be moved with respect to the vacuum chamber using a three-axis translation stage. The differential focal shift between the two wavelengths is about 126 mm. b) Second-stage imaging. To counter differential focal shifts, the two wavelengths are split and later recombined before a shared EMCCD camera. The focus of the 422 nm path can be adjusted independently using two mirrors on a translation stage. Spatial filtering is implemented with an aperture in each of the respective first image planes. The different magnifications of the two paths counter the magnification difference of the first stage, and we measure an overall magnification of 38 for 422 nm and 41 for 370 nm. The fluorescence can be sent to either the EMCCD camera or to a photomultiplier tube (PMT) for each species, depending on the settings of two electronic flip mirrors. Narrow-band optical filters (not depicted) for each wavelength are installed before the flip mirrors. The components are pre-assembled on an optical breadboard which can be moved with respect to the first-stage imaging objective.

https://doi.org/10.7795/110.20260227

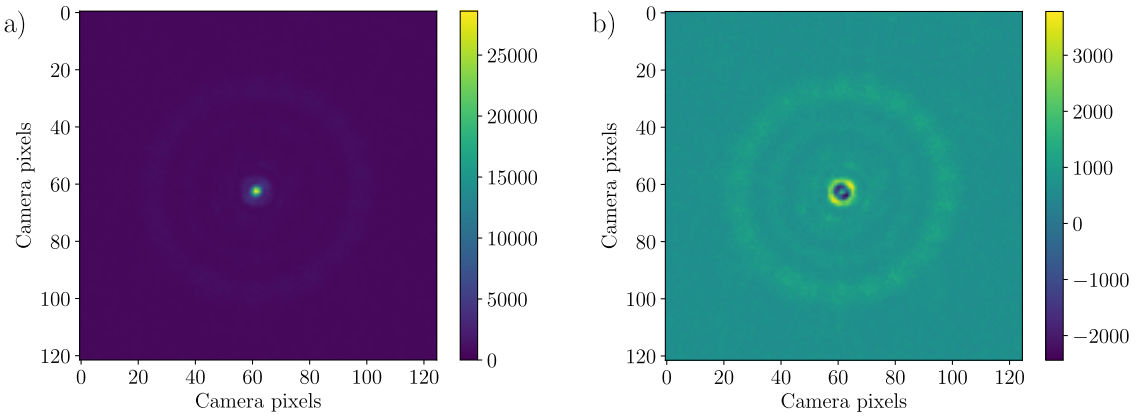

Figure 4.8: Image of a single Sr^+ ion a) and residual with respect to a fit of a 2D Airy function b). Spherical aberrations are clearly visible, with signs of oblique astigmatism close to the center of the image. The fit yields a radius (first zero of the Airy disk) of 3.88(4) pixels, corresponding to about 1.6 µm in the ion plane, and to an effective NA of 0.16.

crosstalk, to collect sufficient fluorescence for detection within a few ms, and to achieve a field of view that allows detection for ≈100 µm long ion chains. We analyse the image quality and implement camera detection using $^{88}Sr^+$. An image of a single $^{88}Sr^+$ ion is depicted in Figure 4.8. A fit of a two-dimensional Airy function to the image yields a radius at the first zero of 3.88(4) pixels, corresponding to about 1.6 µm in the ion plane. This means that ions in a crystal with typical ion-ion distances of 3-6 µm are well-resolved. The fit residual makes aberrations apparent: While coma was overcome by alignment of the first- and second stage imaging systems with respect to each other, signs of spherical aberrations and oblique astigmatism remain visible. These do however not lead to significant cross-talk during detection, since they are about an order of magnitude weaker than the central maximum.

Figure 4.9 shows a linear chain of 16 ions. The ions are clearly resolved, and the field of view is sufficient to perform state detection on ion chains of this size.

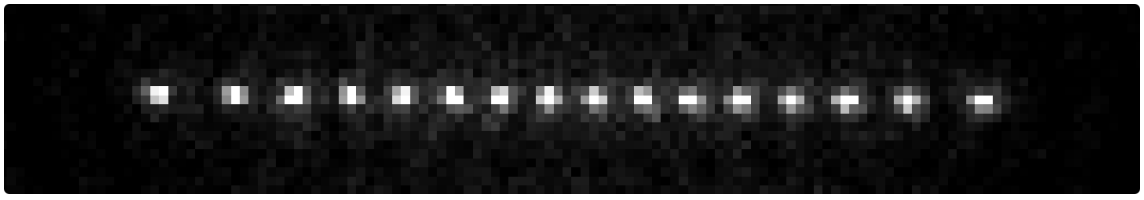

Figure 4.9: Camera image of a linear Coulomb crystal with 16 $^{88}Sr^+$ ions. A 2×2 binning has been used. The total length of the depicted ion chain is about 80 µm.

https://doi.org/10.7795/110.20260227

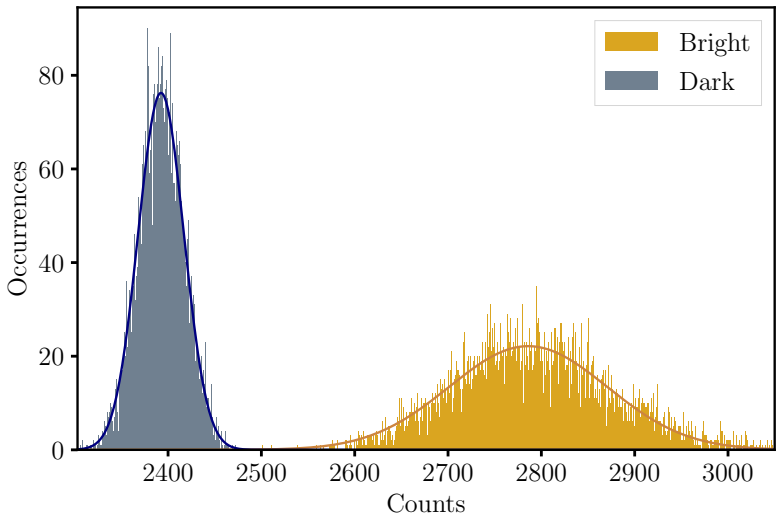

Figure 4.10: Histogram for the state detection of $^{88}Sr^{+}$. The data is obtained for typical experimental parameters: A saturation parameter $s \approx 0.7$ with the 422 nm laser frequency stabilized to the half-maximum of the resonance, a detection time of 7 ms, an EM gain of 200, 2×2 binning, and a region of interest consisting of the four brightest (binned) pixels. Solid lines are Gaussian fits to the distributions.

The maximum observable number of counts for a fully saturated $^{88}Sr^{+}$ ion is given by the product of the 1/4 relative occupation of the excited state [177], the natural linewidth of the transition $2\pi \times 21.6\,\mathrm{MHz}$ [178], and the $\approx 40\%$ quantum efficiency of the PMT, yielding about 13.6×10^6 counts/s. We observe a maximum of 0.12×10^6 counts/s, indicating an effective NA close to 0.2.

Camera-based state detection provides scalability to many ions, as well as site-resolved information. Typical camera settings we employ for state detection are a 2×2 binning and an EM gain of 200. Detection is implemented using a simple threshold on a region of interest (ROI) consisting of the four brightest pixels belonging to each ion. A corresponding histogram for a typical saturation parameter $s \approx 0.7$ and a detection time of 7 ms is shown in Figure 4.10. Gaussian fits to the distributions for the dark and bright states indicate an infidelity below 0.02%. The infidelity in state preparation and the loss of contrast from finite ion temperature are at the few-percent level each. The obtained detection fidelity is therefore more than sufficient to not affect the clock's instability via a loss of contrast.

The number of ions and their approximate positions are detected automatically based on a simple centroid method, and the pixels used as ROI are selected, also automatically, from the 8×8 pixels around each ion position. This function is also

https://doi.org/10.7795/110.20260227

called during clock operation with multiple ions whenever several consecutive invalid clock cycles occur, making the clock robust against the occasional loss of an ion.

Our experimental control system consists of the open-source software and open hardware of the "Advanced Real-Time Infrastructure for Quantum Physics" (ARTIQ). We integrate camera-based detection into the experimental sequences using an external trigger generated in ARTIQ to synchronize the camera acquisition with the corresponding laser pulses for detection. Two images are evaluated together outside of the real-time environment: One taken after clock excitation, and one taken after repumping from the excited state. A callback function evaluates both images, once they become available, extracting the total number of counts in each of the ROIs. The resulting two one-dimensional arrays are passed as datasets into ARTIQ. This takes about 12-15 ms, and currently the experimental sequence only continues once new datasets are available. Which of the ions were excited, and if all ions were bright again after repumping, indicating a valid clock cycle, is then decided within ARTIQ.

4.5 Magnetic field control

Three orthogonal sets of coils are used to define the quantization axis during clock operation. The coils were designed to provide a field of a few µT for a maximal current of 20 mA that can be obtained from operational amplifiers in home-built, low-noise current sources. The currents are provided by a three-channel source that is controlled via DAC voltages generated within the ARTIQ-based experimental control system. An existing routine for magnetic field calibration and compensation of background fields based on the Zeeman-sensitive components of the $^{171}Yb^{+}$ E2 transition has been adapted for use with $^{88}Sr^{+}$, and allows convenient and repeatable setting of magnetic field directions and strengths.

An overview over the coil geometry is provided in Figure 4.11. In addition to the main coils, each direction also features an independent set of coils (in the same coil holders) that could be used for active magnetic field stabilization in the future, if needed. Along the x-axis an additional larger set of coils is used to generate a field of a few hundred µT to prevent coherent population trapping in $^{171}Yb^{+}$ during Doppler cooling and detection [50]. This coil pair generates a field of 1.7 µT/mA at the position of the ions and has a combined resistance of 7 Ω, meaning about 0.6 W

https://doi.org/10.7795/110.20260227

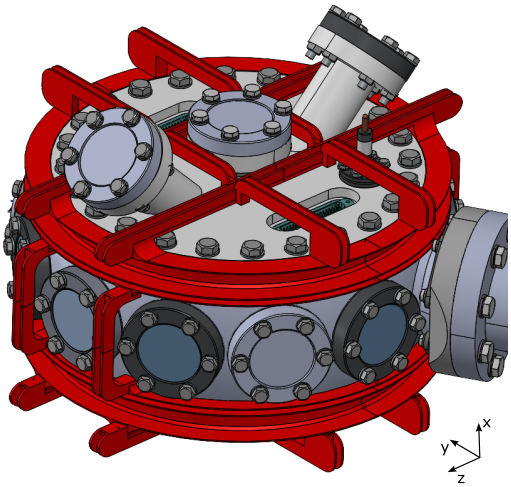

Figure 4.11: Overview over magnetic field coil geometry. 3D-printed coil holders are shown in red, with the vacuum chamber depicted for reference. Three orthogonal sets of coils are used to define the quantization axis with a field of a few µT during clock operation. Along the x-axis an additional larger set of coils is used to generate a field of a few hundred µT to impede coherent population trapping in $^{171}Yb^{+}$ during detection. Due to geometric constraints, the coils (not shown) were wound by hand around the assembled vacuum system.

of power are dissipated when generating a field of 500 µT. To avoid inhomogeneously heating up the vacuum chamber, which could impede a precise characterization of the ions' thermal environment, copper tubing for water cooling is set up in the center of the coils. All coil pairs are connected in series, except for the large coils which are connected in parallel so that charges can flow off them faster.

Along the z-axis, an additional, independent coil pair is connected to provide a magnetic field gradient at the position of the ions. We use this set of coils to compensate small magnetic field gradients on the order of 0.1 nT/100 µm along chains of trapped ions with currents on the order of 1 mA.

A low-noise magnetic field is particularly important for clock operation based on $^{88}Sr^{+}$, which, in contrast to $^{171}Yb^{+}$, does not offer a first-order Zeeman insensitive clock transition. We were able to extend initial coherence times of a few tens of ms to over 100 ms on even the most sensitive Zeeman components of the $^{2}S_{1/2} \rightarrow {}^{2}D_{5/2}$ clock transition in $^{88}Sr^{+}$. Initially, ground loops from connections between ion trap regions that were already grounded to the vacuum chamber and the ground of the DC voltage supply via the carrier board, feedthrough, and a 2 m long cable, were limiting

https://doi.org/10.7795/110.20260227

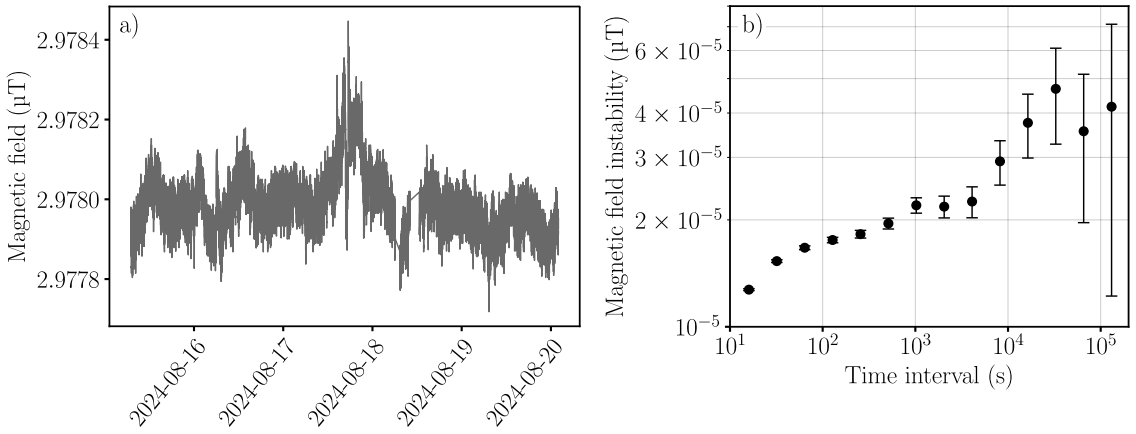

Figure 4.12: Typical day-to-day variation of the magnetic field, obtained from clock operation with a single $^{88}Sr^{+}$ ion. a) Magnetic field during approximately 115 hours of clock operation. b) Instability of the magnetic field data in a) as characterized by the Allan deviation.

the coherence. After interrupting these connections on the outside of the chamber, the next limiting factor was the resolution of the digital-to-analog conversion, which was contributing to the noise of the voltage-controlled current source. This effect was reduced by adapting the voltage-to-current conversion factor of the current source to only cover the necessary magnetic field range of a few μT. So far, we were unable to fully extend the coherence on the $^{88}Sr^{+}$ clock transition to a level limited only by the 391 ms excited state lifetime. One difference between our current experimental configuration and the ideal ground configuration shown in [179] is the fact that the ARTIQ DAC output used to provide DC voltages to the trap electrodes is not purely differential, and grounding of the ARTIQ crate could not be avoided.

To analyse slow variations of the magnetic field, we extract its magnitude from clock operation with $^{88}Sr^{+}$, as described in chapter 5, using the known first-order magnetic field sensitivities. An example for magnetic field variation during several days of clock operation is shown in Figure 4.12. Typical variations are below the nT-level over days, unless physical changes are made to the experimental apparatus.

https://doi.org/10.7795/110.20260227

4.6 Ion trap characterization

The ion trap is arguably the most important experimental component in any trapped-ion experiment, and in optical clocks based on trapped ions its properties, such as excess micromotion or ion heating, can easily prohibit fractional systematic uncertainties at the 10^{-18} level. We use a linear, segmented ion trap based on the design in [174], which was developed in Prof. Mehlstäubler's group at PTB. The properties of this trap design, in particular with respect to the use for optical clocks based on trapped ions, have been analysed in detail in several publications [174, 180–182] and theses [175, 183, 184]. Here, we forego a detailed analysis of the trap properties and focus only on those that might differ from one implementation to another, and that are directly relevant to the clock performance.

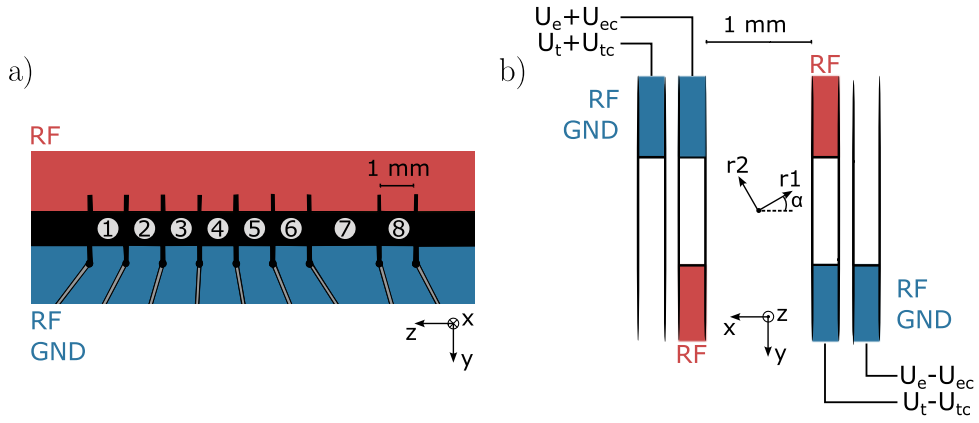

Figure 4.13: Schematic depiction of ion trap geometry. a) Frontal view showing the trapping segments 1-8. Ions are loaded into segment 1, and all characterization measurements and spectroscopy reported here is also performed in this segment. b) Cut through the radial plane. The voltage U_e, applied to neighboring segments, is used for axial confinement. The angle α of the radial trap axes with respect to the trap wafers is determined by the voltages U_e and U_t. The voltages U_{ec} and U_{tc} are used to compensate stray fields in the radial plane within one segment.

A schematic overview over the trap geometry is depicted in Figure 4.13. Four precision machined aluminium-nitride (AlN) wafers with structured gold coating are stacked with AlN spacers and aligned to within about 2 µm with respect to each other. The inner two wafers carry the RF and DC voltages required for ion trapping, while the outer wafers offer additional degrees of freedom for compensation of stray electric fields and rotation of the trap axes. Even though the trap offers eight distinct trapping zones, so far all measurements have been performed in the trap segment labeled 1 in Figure 4.13, which is used for ion loading.

https://doi.org/10.7795/110.20260227

All voltages applied to the ion trap are generated within our experimental control system based on ARTIQ. The trap drive RF voltage at 14.242 MHz is generated with direct digital synthesis, amplified with a standard 2W amplifier, and applied to the trap via a helical resonator with a quality factor of about 500, which was constructed following the design in [185]. The DC voltages are generated using digital-to-analog conversion, and are amplified to a maximum of 85 V.

4.6.1 Excess micromotion

We compensate for stray electric fields, thereby minimizing excess micromotion, using the photon-correlation technique [186] with three mutually orthogonal cooling laser beams. This typically yields a residual rf field close to zero in the radial directions, however we do observe some excess axial micromotion that cannot be compensated. For a given trap drive voltage, the amount of axial micromotion remains constant over time. We measure the residual field for a variety of ion positions along the trap axis, with the results shown in Figure 4.14 , and find no significant changes within a few tens of µm. We observe a single coherent photoncorrelation signal from chains of up to ten ions, and micromotion monitoring and compensation is routinely performed also with chains of ions.

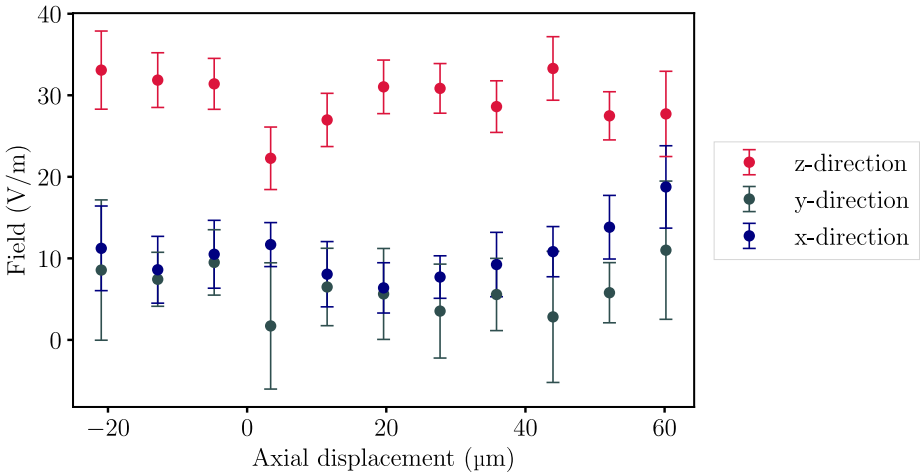

Figure 4.14: Residual field amplitude due to excess micromotion at different positions along the trap axis. A single $^{88}Sr^{+}$ ion was confined with a mean radial secular frequency of about 630 kHz and, after compensation of stray fields, moved along the trap axis with a varying differential voltage between the electrodes used for DC confinement. Error bars are based on the uncertainties of the fits to the photoncorrelation signals. Within the uncertainty, the micromotion remains the same for the different ion positions. A small amount of residual axial micromotion that cannot be compensated is visible.

https://doi.org/10.7795/110.20260227

While the radial excess micromotion in the x-direction increases slowly and monotonically on a timescale of days to weeks, we see non-monotonic changes in the y-direction, sometimes on a timescale of hours. We attribute these changes to charges on the re-entrant viewport, since the direction does not match that of any of the trap electrodes. To control frequency shifts associated with excess micromotion, discussed in subsection 5.3.3, we have implemented regular automatic micromotion monitoring and, if necessary, compensation during clock operation with $^{88}Sr^+$.

4.6.2 Ion heating

In the absence of cooling, the temperature of trapped ions increases over time due to electric field noise that couples to their motion. This effect needs to be considered when assessing frequency shifts resulting from the finite ion temperature. Large heating rates lead to an increased temperature uncertainty and accordingly to an increased uncertainty of the second-order Doppler shift and the quadratic DC Stark shift from the finite mean-squared trap field that is sampled by the ions (c.f. subsection 5.3.2).

We measure the heating rate of each of the three motional modes of a single trapped $^{88}Sr^+$ ion. To this end, we first perform continuous resolved sideband cooling on the cycling $m_J = -1/2 \rightarrow m_J = -5/2$ component of the $^2S_{1/2} \rightarrow {}^2D_{5/2}$ clock transition, bringing the ion close to its motional ground state. For each mode we then measure the relative excitation probabilities $P_{\mathrm{rsb}}/P_{\mathrm{bsb}}$ of first-order red and blue motional sidebands of the same Zeeman component. We ensure that both sidebands are resonantly probed, with interrogation times much shorter than those corresponding to maximum population transfer. The mean phonon number $\bar{n}$ is extracted via [187]

$$\bar{n} = \frac{P_{\mathrm{rsb}}/P_{\mathrm{bsb}}}{1 - P_{\mathrm{rsb}}/P_{\mathrm{bsb}}}\,. \tag{4.4}$$

The heating rate is obtained from measurements with a variable wait time between sideband cooling and temperature determination, and the results are depicted in Figure 4.15. Linear fits to the mean phonon number yield the following heating rates:

Mode	Secular frequency	$\dot{\bar{n}}$ (phonons/s)	$\hbar\omega\dot{\bar{n}}/k_{\mathrm{B}}$ (mK/s)
Lower radial	$2\pi \times 1060\,\mathrm{kHz}$	0.3(1)	0.016(6)
Higher radial	$2\pi \times 1080\,\mathrm{kHz}$	0.7(1)	0.038(4)
Axial	$2\pi \times 220\,\mathrm{kHz}$	3.6(3)	0.038(3)

https://doi.org/10.7795/110.20260227

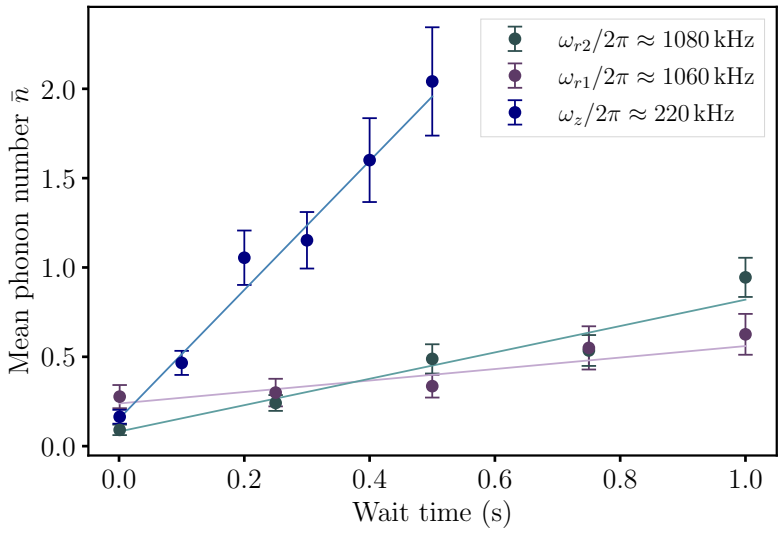

Figure 4.15: Mean thermal occupation numbers $\bar{n}$ of a single $^{88}Sr^+$ ion for different wait times after sideband cooling. Error bars are statistical, assuming a Poisson distribution for the total number of excitations on each sideband. Solid lines correspond to linear fits.

The confinement conditions used in this measurement are those employed for clock operation with multiple $^{88}Sr^+$ ions (c.f. chapter 5). An independent measurement with the higher axial secular frequency of $\omega_z \approx 2\pi \times 670\,\mathrm{kHz}$ used during single-ion clock operation yielded an even lower axial heating rate of 0.52(3) phonons/s, or 0.017(1) mK/s.

Low heating rates on the order of 1 phonon/s are typical for this type of ion trap [174, 184, 188], due to the relatively large distance of the ion from the gold-coated trap electrodes and the low-pass filtering that is implemented directly on the trap wafers. For clock operation with Doppler-cooled $^{88}Sr^+$ ions, and a coherent interrogation time limited to a few hundred ms, these heating rates are completely negligible in the determination of frequency shifts.

4.6.3 Oscillating magnetic field from trap drive

Small unbalanced currents result in a magnetic field that oscillates at the frequency of the trap drive. Since this field may shift transition frequencies at a level that is relevant for optical clocks, its magnitude and direction need to be assessed [189–191]. We follow the approach developed in [190]: When the energy difference between two Zeeman levels is brought close to resonance with the trap drive frequency,

https://doi.org/10.7795/110.20260227

the coupling of the two levels by the oscillating magnetic field perpendicular to the quantization axis leads to an Autler-Townes splitting. Measuring the resonant frequency splitting between the dressed states allows assessing the amplitude $B_{RF,\perp}$ of the oscillating field for a given RF voltage applied to the trap.

Compared to our usual operating conditions, achieving a Zeeman splitting close to our trap drive frequeny of $\Omega_{RF} = 2\pi \times 14.242\,\mathrm{MHz}$ requires a rather large static magnetic field. We choose to perform this measurement with $^{88}Sr^+$, since the Zeeman splitting of $\omega_Z = 2\pi \times 28\,\mathrm{kHz/\mu T}\, B$ between its ground state sublevels $^2S_{1/2}, m_J = \pm 1/2$ is twice as large as than available in the $^{171}Yb^+$ ground state for a given magnetic field strength B. The necessary field of 508.6 µT can be obtained by applying a current of about 303 mA to the pair of large magnetic field coils. We optically drive the $^2S_{1/2}, m_J = -1/2 \rightarrow {}^2D_{5/2}, m_J = -5/2$ transition to observe the ground state avoided crossing, since it is conveniently free of a second-order Zeeman shift. The measurement is performed with a single $^{88}Sr^+$ ion under typical trapping conditions (radial trapping frequencies of 1052 kHz and 862 kHz). Excess micromotion is minimized before the measurement and monitored intermittently between frequency scans.

Figure 4.16 shows the resulting data: Spectra showing the Autler-Townes splitting are recorded for different amplitudes of the static magnetic field across the resonance. The frequency splitting is obtained from fits to the two peaks. Changing the current supplied to the coils and therefore the magnitude of the static magnetic field leads to a change in detuning $\delta = \omega_Z - \Omega_{RF}$, with the splitting given by $\sqrt{\delta^2 + \Omega^2}$. A fit with Ω and the current-to-field conversion factor of the coils as free parameters yields a resonant Rabi frequency of $\Omega = 2\pi \times 19.716(22)\,\mathrm{kHz}$. We extract the corresponding magnetic field causing this coupling via

$$\Omega = \frac{g_J \mu_B}{\hbar} B_{RF,\perp} \tag{4.5}$$

and obtain $B_{RF,\perp} = 1.4073(16)\,\mu\mathrm{T}$.

We observe excess scatter of the splittings when assuming the uncertainty of each splitting corresponds to only that of the fit result. The residuals are correlated with the order in which the scans were taken, and are explained by variation of the RF voltage on the trap, as evident from variation of the radial secular frequencies on the order of 1 kHz during the measurement period. The uncertainty of the fit used to extract Ω incorporates the excess scatter of the data to fulfill $\chi^2_{\mathrm{red}} = 1$. This

https://doi.org/10.7795/110.20260227

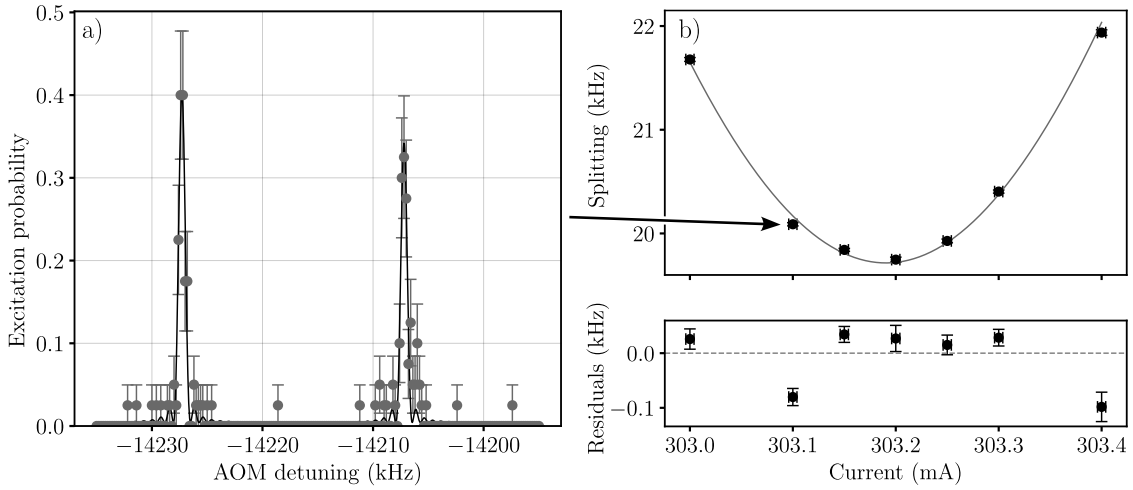

Figure 4.16: Measurement of Autler-Townes splitting between the ${}^2S_{1/2}, m_J = \pm 1/2$ states in ${}^{88}Sr^+$ caused by the oscillating magnetic field from the trap drive. a) Typical spectrum taken on the ${}^2S_{1/2}, m_J = -1/2 \rightarrow {}^2D_{5/2}, m_J = -5/2$ transition at a a static magnetic field strength B close to resonance of the ground state Zeeman splitting and the trap drive frequency: 14.242 MHz = 28 kHz/µT B. A fit is used to extract the frequency splitting between the two peaks. b) Spectra are taking for different currents applied to a pair of magnetic field coils, i.e. different values of B across the resonance. The quantization axis is vertical (along the x-direction). Error bars are obtained from the uncertainties of the fits. The minimal splitting of 19.716(22) kHz corresponds to an oscillating magnetic field of amplitude $B_{RF,\perp} = 1.4073(16)$ µT perpendicular to the quantization axis. Excess scatter is caused by variations of the trap drive voltage and accounted for in the uncertainty of the fit result Ω.

treatment also pays tribute to the fact that the same variations of the RF voltage that limit the determination of the AC magnetic field are also expected during clock operation. Implementing active stabilization of the RF power, e.g. as described in [192], is expected to significantly reduce these variations. This will allow both more precise determination of the oscillating magnetic field, as well as reduce the variation of its amplitude during clock operation.

The most straightforward way to assess the oscillating field in all three dimensions would be to repeat the measurement above with two orthogonal orientations of the static magnetic field. However, the experimental apparatus only features one pair of coils that allows for large enough currents to produce the required field (c.f. section 4.5), oriented along the vertical direction. We therefore resort to tilting the angle of the quantization axis with a smaller field produced via the available orthogonal sets of coils. The results are shown in Figure 4.17. We find $B_{RF,\perp} = 2.0769(30)$ µT with a tilt of the quantization axis by 9.9° orthogonal to the trap

https://doi.org/10.7795/110.20260227

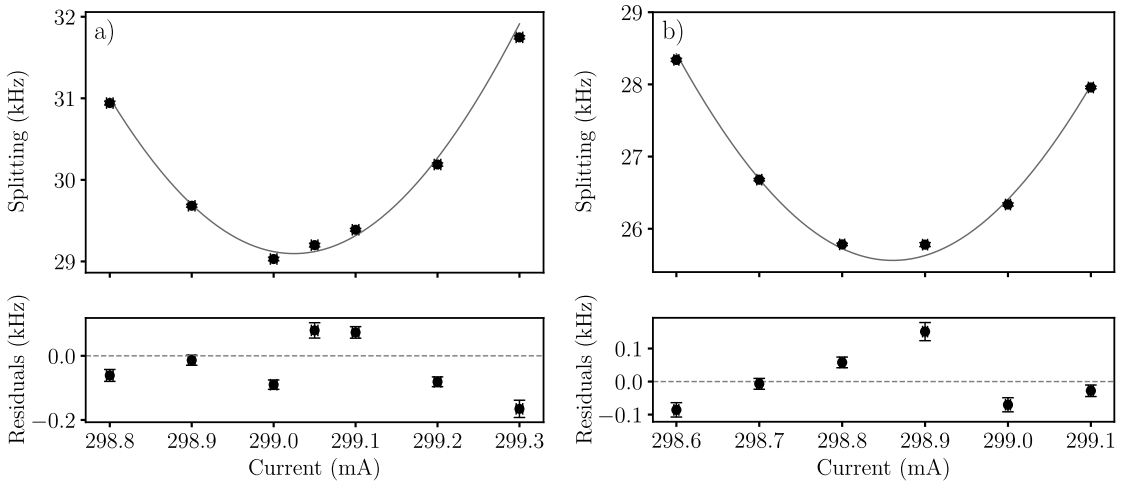

Figure 4.17: Measurement of Autler-Townes splitting due to oscillating magnetic field as above, but with the quantization axis tilted from the vertical (x) orientation by a) 9.9° orthogonal to the trap axis (y-direction) and b) by 7.7° along the trap axis (z-direction). We find a) $\Omega = 2\pi \times 29.096(42)\,\mathrm{kHz}$ and b) $\Omega = 2\pi \times 25.561(35)\,\mathrm{kHz}$, corresponding to orthogonal magnetic field amplitudes of $B_{RF,\perp} = 2.0769(30)\,\mu\mathrm{T}$ and $B_{RF,\perp} = 1.8246(25)\,\mu\mathrm{T}$ respectively.

axis and $B_{RF,\perp} = 1.8246(25)\,\mu\mathrm{T}$ with a tilt of 7.7° in the direction of the trap axis. The increased amplitude for a tilt in both directions compared to the original measurement immediately shows that the largest oscillating field component must be along the vertical direction, corresponding to the quantization axis of the first measurement.

From geometric considerations, and with an uncertainty of 0.1° for both tilting angles, we find the three components of the oscillating magnetic field amplitude as

$$B_{RF} = \left[6.091(55), 0.834(10), 1.1333(75)\right]\ \mu\mathrm{T}\,, \tag{4.6}$$

which corresponds to a total mean amplitude of $6.252(54)\,\mu\mathrm{T}$. The uncertainty of around 1% is limited by the variations of the oscillating field during the measurement. The field is significantly larger than that measured in our group for an earlier trap based on the same design in a different experimental apparatus, which had an amplitude well below $1\,\mu\mathrm{T}$. The cause of the comparatively large amplitude, in particular in the x-direction, is not immediately obvious. Further investigations are necessary to enable $^{171}\mathrm{Yb}^{+}$ clocks with lowest uncertainties: For the $^{171}\mathrm{Yb}^{+}$ E3 transition with a sensitivity of $2.28\,\mathrm{mHz}/\mu\mathrm{T}^2$ [190] (averaged over three interrogation directions), the current measurement result would yield a 2×10^{-18} fractional frequency uncertainty.

https://doi.org/10.7795/110.20260227

4.7 Temperature management

The uncertainty associated with the Stark shift induced by thermal radiation is a major contribution to the overall systematic uncertainty of many state-of-the-art optical atomic clocks, in particular those operating in a room-temperature environment. To characterize the thermal environment of the ions, we employ six resistive temperature sensors, which have been calibrated with a $k = 2$ uncertainty of 37 mK at PTB, corresponding to a 1σ-uncertainty of $\sigma_{T_{\text{sensor}}} = 18.5\,\text{mK}$. Two of the sensors are soldered directly onto the RF-carrying inner trap wafers, while the remaining four are distributed on the outside of the vacuum chamber (c.f. Figure 5.10). A linear fit to each sensor's calibration points is used to interpolate the temperature readings. We pre-selected sensors for calibration that showed no relevant variation of the measured temperatures after heating and cooling processes, which is important since the calibration was performed before soldering the sensors to the trap chips.

When applying a radiofrequency voltage to the trap, the temperatures of the trap increases with respect to the background temperature of the chamber T_{ch}. Additionally, the temperature sensor on the outside of the RF feedthrough also shows an elevated temperature, leading to increased inhomogeneity between the four temperature sensors on the outside of the chamber. When no RF power is supplied to the ion trap and the system is in thermal equilibrium, the readings from all sensors agree to within less than 35 mK.

During clock operation, the temperature rise of the trap electrodes due to the applied RF power has to be considered, since they make up a significant fraction of the solid angle around the ions. The ion trap we employ has been specifically designed to provide a low temperature rise under RF, and extensive thermal modeling for this trap geometry has been developed [182].

The effective temperature experienced by the ions

$$T_{\text{ions}} = T_{\text{ch}} + \Delta T_{\text{ions}} \tag{4.7}$$

is extracted from the temperature of the chamber T_{ch}, which we obtain as the mean of the four temperature sensors on the vacuum chamber, and the effective temperature increase ΔT_{ions} experienced by the ions inside the trap, which can be obtained from the average [182]:

$$\Delta T_{\text{ions}} = \frac{\alpha\,\Delta T_1 + \beta\,\Delta T_2}{2}\,, \tag{4.8}$$

https://doi.org/10.7795/110.20260227

with $\alpha = 0.43(10)$, $\beta = 0.32(10)$, and $\Delta T_{1,2} = T_{1,2} - T_{\mathrm{ch}}$ the temperature differences between T_1 and T_2 read out from the sensors on the trap wafers and the vacuum chamber temperature. Here, T_1 denotes the sensor closer to the carrier board, and T_2 that further away from it.

The overall resulting uncertainty the temperature experienced by the ions is then

$$\sigma_{T_{\mathrm{ions}}} = \Bigg[\left(\frac{1}{2}\Delta T_1\, \sigma_\alpha\right)^2 + \left(\frac{1}{2}\Delta T_2\, \sigma_\beta\right)^2 + \left(\left(1 - \frac{\alpha}{2} - \frac{\beta}{2}\right)\sigma_{T_{\mathrm{ch}}}\right)^2 + \left(\frac{1}{2}\alpha\, \sigma_{T_1}\right)^2 + \left(\frac{1}{2}\beta\, \sigma_{T_2}\right)^2 \Bigg]^{1/2} . \tag{4.9}$$

The uncertainty of the chamber temperature is given by

$$\sigma_{T_{\mathrm{ch}}} = \sqrt{\sigma^2_{T_{\mathrm{ch,stat}}} + \sigma^2_{T_{\mathrm{sensor}}}} \tag{4.10}$$

where the uncertainty due to its inhomogeneity is

$$\sigma_{T_{\mathrm{ch,stat}}} = \left(\max(\{T_i\}) - \min(\{T_i\})\right)/\sqrt{12}\,, \tag{4.11}$$

with $\{T_i\} = \{T_3, ..., T_6\}$.

For the work presented here, we typically employ an RF power that yields radial secular frequencies around 1 MHz for a single $^{88}Sr^{+}$ ion. Under these operating conditions, we find $\left(\max(\{T_i\}) - \min(\{T_i\})\right) \leq 150\,\mathrm{mK}$ and therefore $\sigma T_{\mathrm{ch}} = 47\,\mathrm{mK}$. Using the observed upper bounds of $\Delta T_1 \approx 570\,\mathrm{mK}$ and $\Delta T_2 \approx 590\,\mathrm{mK}$ yields an overall temperature uncertainty of $\sigma_{T_{\mathrm{ions}}} = 50.7\,\mathrm{mK}$. Here, the first three terms in Equation 4.9 dominate, each contributing close to 1/3 of the uncertainty. The temperature uncertainty could be drastically reduced by actively cooling the RF feedthrough and/or the connected ion trap, thereby reducing the RF-induced temperature increases $\Delta T_{1,2}$, as well as the inhomogeneity of the chamber temperature, which is currently dominated by the temperature increase around the feedthrough.

Since the radial trapping frequencies scale inversely with the ion mass, an increase of the RF power might be beneficial for future work with $^{171}Yb^{+}$. For an increase close to 3 dB, we find $\Delta T_1 \approx 1040\,\mathrm{mK}$ and $\Delta T_2 \approx 1080\,\mathrm{mK}$, as well as an increased temperature inhomogeneity of the vacuum chamber $\left(\max(\{T_i\}) - \min(\{T_i\})\right) \approx 280\,\mathrm{mK}$. This corresponds to an overall temperature uncertainty of 91 mK. The

https://doi.org/10.7795/110.20260227

temperature increase for a given RF voltage is significantly higher in our system than those observed in [182], which might be caused by worse heat-sinking of the ion trap to the chamber in our setup.

Under current operating conditions the temperature experienced by the ions varies around a mean value of about 23.6 °C with the room temperature of the laboratory. All temperature sensors are automatically read out every second, and the results are logged in a database and can be used to calculate a time-resolved correction of the frequency shift from thermal radiation for each clock transition. The timescales of the laboratory temperature variations are slow enough not to cause additional temperature uncertainties, since the time-resolved correction of the associated frequency shift is applied with a temporal resolution of 10 s.

4.8 Implications for clock operation with $^{171}Yb^{+}$

This chapter has, after briefly introducing the motivation for combining $^{88}Sr^{+}$ and $^{171}Yb^{+}$ ions, focused on describing the new experimental apparatus and some of the considerations that went into its construction. First characterization measurements were presented, the results of which will become important for the discussions of frequency shifts on the $^{88}Sr^{+}$ clock transition in the next chapter.

The system was set up with the goal of enabling a systematic uncertainty in the mid-10^{-19}-range for a clock operating on the $^{171}Yb^{+}$ E3 transition, as well as stable and robust clock operation for improved tests of fundamental physics. Before focusing in detail on a $^{88}Sr^{+}$ clock that has been implemented with this apparatus (c.f. chapter 5), I'd therefore like to briefly comment on the prospects for optical clock operation with $^{171}Yb^{+}$ based on the current state and knowledge of the experiment.

The very low heating rates found with trapped $^{88}Sr^{+}$ ions are promising for extended coherent interrogation of the $^{171}Yb^{+}$ E3 transition. In a single-ion trap in our group, a coherent interrogation time of 2 s has enabled an instability of $5 \times 10^{-16}/\sqrt{\tau(\mathrm{s})}$. Interrogating nine ions simultaneously in the linear trap of the new apparatus could reduce this instability by up to a factor of 3. This would in turn enable reaching a fractional statistical uncertainty below 1×10^{-18} within a day. The trap also seems very well-suited for experiments towards minute-scale coherence between two $^{171}Yb^{+}$ ions, aided by sympathetic cooling with a $^{88}Sr^{+}$ ion.

https://doi.org/10.7795/110.20260227

For the clock based on $^{88}Sr^+$, the two frequency shifts associated with excess micromotion largely cancel at our trap drive frequency [168]. Excess micromotion will become more relevant for future clock operation with $^{171}Yb^+$, which does not provide this cancellation. The presence of a moderate amount of incompensable axial micromotion, and some excess variation of one of the radial components will make a careful and time-resolved characterization necessary. Compensation of the varying field component experienced by the ion to a maximal amplitude of about 50 V/m, characterized to within 5 V/m, seems feasible with regular monitoring, for example every hour. Together with a constant axial contribution of 90 V/m, determined to within 5 V/m, this would correspond to a fractional frequency uncertainty of 6×10^{-19} for a clock operating on the E2 transition and 3×10^{-19} for a clock based on the E3 transition.

As discussed in more detail in the next chapter, the 51 mK uncertainty of the temperature experienced by the ions corresponds to a fractional uncertainty of 3.7×10^{-19} for the $^{88}Sr^+$ clock. Even though clock operation with $^{171}Yb^+$ will likely require a higher RF power, leading to a larger temperature uncertainty in the current configuration of the experiment, the sensitivity to thermal radiation is more than five times smaller for the E3 transition [193]. A temperature uncertainty of 100 mK would therefore lead to a fractional frequency uncertainty of only about 1×10^{-19}.

To summarize, even though clock operation with $^{171}Yb^+$ has not been implemented yet, things look promising for a clock based on the E3 transition, and the properties of the experimental apparatus should not impede state-of-the art systematic uncertainties well below 1×10^{-18}. The instabilities of frequency ratio measurements involving $^{171}Yb^+$ and $^{88}Sr^+$ can be improved with this system compared to those obtained to date: via extended coherent interrogation times on the E3 transition, and, as demonstrated in the following, by simultaneously interrogating multiple ions in a linear Coulomb crystal.

https://doi.org/10.7795/110.20260227

5 An optical clock based on multiple $^{88}Sr^{+}$ ions

An optical clock based on the $^2S_{1/2} \rightarrow {}^2D_{5/2}$ transition in $^{88}Sr^{+}$ was realized with the experimental apparatus introduced in the previous chapter. Simultaneously interrogating multiple ions in a linear Coulomb crystal offers a straightforward avenue towards an improved frequency instability and therefore reduced measurement times. However, differences in frequency shifts for the different positions in an ion chain need to be considered carefully. So far, clock operation with three $^{88}Sr^{+}$ ions [43] and four $^{115}In^{+}$ ions [21] has been demonstrated, though not with fully evaluated systematic uncertainties.

In the scope of this work, a robust and accurate clock with up to 10 $^{88}Sr^{+}$ ions was implemented. Scaling to multiple ions is particularly helpful for a $^{88}Sr^{+}$ clock, as the instability for a single ion is limited by the Hz-level natural linewidth [170] and magnetic field fluctuations. Even though the employed transition is rather sensitive to external fields, we show that the frequency shifts from variations of external perturbations along the ion chain can be suppressed to a level that does not limit the systematic uncertainty. Systematic frequency shifts and their uncertainties are evaluated for both operation with a single ion and multiple ions.

The chapter starts out by introducing the experimental parameters and interrogation sequence used for clock operation with $^{88}Sr^{+}$ in section 5.1. Effects related to multi-ion clock operation are discussed in section 5.2, starting with the consequences of the coupled ion motion. Then, a technique for obtaining ion-resolved information on frequency shifts even in the case of global clock interrogation with a single laser beam is introduced. This technique is applied to analyse the variation of the quadrupole shift from ion-ion Coulomb interactions, as well as a magnetic field gradient. Both effects are suppressed experimentally, and the resulting residual clock shifts are analysed.

https://doi.org/10.7795/110.20260227

Section 5.3 discusses systematic effects relevant to both operation with a single and multiple ions, with a preliminary uncertainty budget as a key result. We obtain a systematic uncertainty of 5.3×10^{-19} for the clock operating with eight to ten ions. In fact, multi-ion operation reduces the systematic uncertainty from 6.5×10^{-19} for a single ion, since melting of the Coulomb crystal reduces the number of undetected background gas collisions.

Section 5.4 contains results from an optical frequency comparison between the new optical clock and the single-ion $^{171}Yb^{+}$ clock operating on the E3 transition (c.f. chapter 2). We obtain a combined fractional uncertainty of 2.9×10^{-18} on the resulting frequency ratio, the lowest reported on any frequency comparison between different transitions to date. Measurement results obtained with a single $^{88}Sr^{+}$ ion are compatible with those obtained with eight to ten ions, and multi-ion operation leads to a significantly improved measurement instability.

5.1 Experimental parameters and interrogation sequence

A single $^{88}Sr^{+}$ ion or a linear Coulomb crystal of eight to ten $^{88}Sr^{+}$ ions is confined in one segment of the linear, segmented ion trap. An overview over the measurement geometry is shown in Figure 5.1. Laser beams with broad elliptical cross-sections are employed for cooling, repumping, and state preparation to address all ions in a chain with similar intensities. Residual fluorescence variations between ions in the center of the chain and its edges are typically limited to about 5%. The beam used for clock interrogation is aligned along the axis of the ion chain, yielding the same Rabi frequency for all ions (within the $\approx 1\%$ resolution obtained in typical measurements).

During clock operation, the same experimental sequence, largely following that developed by Martin Steinel for the work reported in [43], is repeated periodically: Laser cooling on the dipole-allowed $^2S_{1/2} \rightarrow {}^2P_{1/2}$ transition at 422 nm for 5 ms reduces residual thermal motion close to the Doppler limit, with laser light at 1092 nm preventing population trapping in the $^2D_{3/2}$ state. For multiple ions, we additionally perform resolved sideband cooling of the axial centre-of-mass (COM) motional mode (c.f. subsection 5.3.2). Subsequent preparation in the $^2S_{1/2}, m_J = -1/2\,(+1/2)$ sublevel with a fidelity of about 95% is achieved with multiple fast pulses on the

https://doi.org/10.7795/110.20260227

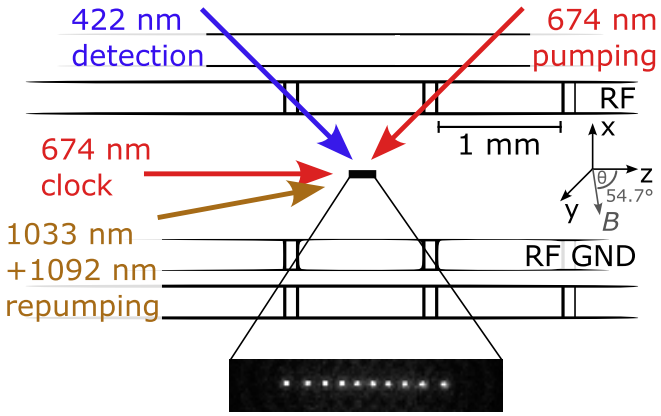

Figure 5.1: Overview over measurement geometry for clock operation with $^{88}Sr^{+}$ ions. Chains of up to ten ions are trapped in a single segment of the linear radiofrequency trap. The ions are addressed collectively: laser beams with elliptical cross-section are used for Doppler cooling and state detection (422 nm), state preparation and sideband cooling (674 nm), and repumping (1033 nm and 1092 nm). For clock operation, the ions are interrogated on the $^2S_{1/2} \rightarrow {}^2D_{5/2}$ transition with a 674 nm laser beam propagating along the trap axis. The magnetic field defining the quantization axis is precisely adjusted to provide an angle of 54.7° w.r.t. the trap axis, thereby suppressing the effect of varying electric field gradients along the ion chain.

$^2S_{1/2}, m_J = +1/2\,(-1/2) \rightarrow {}^2D_{5/2}, m_J = -3/2\,(+3/2)$ transition respectively, with repumping from the $^2D_{5/2}$ state after each pulse. After mechanical shutters block the light used for cooling and preparation, Rabi interrogation of the clock transition is performed using a single rectangular laser pulse. A successful excitation is indicated by absence of fluorescence at the beginning of the subsequent cooling cycle. After fluorescence detection, laser light at 1033 nm enables fast depletion of the excited clock state via the $^2P_{3/2}$ state back to the ground state. A clock interrogation cycle is valid (i.e. used for steering of the clock) if the fluorescence signal reappears within the subsequent cooling period. An invalid cycle is repeated, and lack of fluorescence over several cycles triggers a "rescue" sequence that involves reducing the trap confinement and illuminating the ion(s) with strong, red-detuned 422 nm laser light. While we use a photomultiplier tube for state detection of a single ion, an EMCCD camera is employed for detection during multi-ion operation.

The $^2S_{1/2} \rightarrow {}^2D_{5/2}$ transition is split into ten first-order Zeeman-sensitive components via a static external magnetic field of about 3 µT, as illustrated in Figure 5.2. We interrogate pairs of transitions with opposite sensitivity, and use the resulting average, which is free of the first-order Zeeman shift. Additionally, we construct a weighted average of two such transition pairs to suppress tensorial frequency shifts

https://doi.org/10.7795/110.20260227

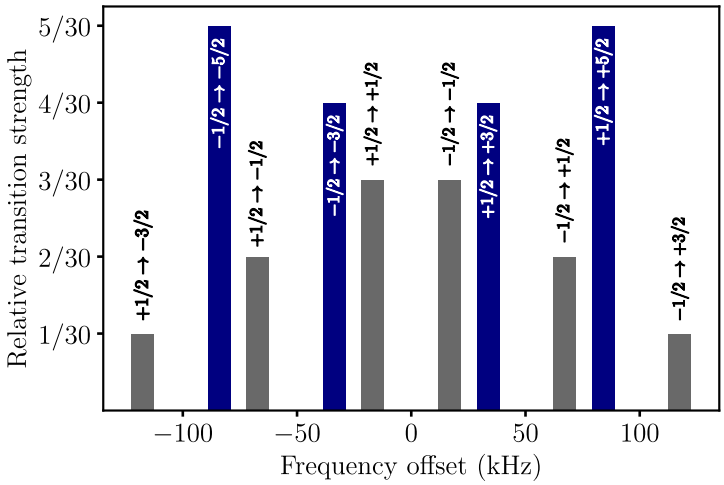

Figure 5.2: Zeeman components of the $^2S_{1/2} \rightarrow {}^2D_{5/2}$ transition in $^{88}Sr^{+}$ for an external magnetic field of 3 µT. The relative transition strengths are given by the square of the Clebsch-Gordan coefficients. The Zeeman components highlighted in blue are interrogated during optical clock operation.

such as the quadrupole shift [194]. Magnetic field noise limits the coherence in our setup, and consequently we scale the interrogation time t inversely with the Zeeman sensitivity of each transition pair. 250 ms long interrogation pulses are used on each of the $^2S_{1/2}, m_J = \pm 1/2 \rightarrow {}^2D_{5/2}, m_J = \pm 3/2$ transitions, and 100 ms long pulses on the $^2S_{1/2}, m_J = \pm 1/2 \rightarrow {}^2D_{5/2}, m_J = \pm 5/2$ transitions. For these interrogation times, we observe Fourier-limited linewidths and maximum excitation probabilities of about 67% and 80% respectively, with the difference resulting from the 391 ms [171] excited-state lifetime.

We use the combination of Zeeman pairs we have previously found to yield the best instability of a $^{88}Sr^{+}$ clock limited by magnetic field noise [43]: The $^2S_{1/2}, m_J = \pm 1/2 \rightarrow {}^2D_{5/2}, m_J = \pm 3/2$ transition pair is interrogated twice as often as the $^2S_{1/2}, m_J = \pm 1/2 \rightarrow {}^2D_{5/2}, m_J = \pm 5/2$ transition pair, and they are averaged with respective weights of 5/6 and 1/6.

Each Zeeman component is interrogated with detunings $\pm\Delta\nu = \pm 0.4/t$ from its center frequency, such that the excitation probability is 50% of the maximum. After completing a measurement cycle, the corresponding servo shifts the center frequency by $\left(0.15\,(n_+ - n_-)/N\right)\Delta\nu$, with $n_+(n_-)$ the total number of successful excitations at positive (negative) detuning after two interrogations each, performed in the order $[-\Delta\nu, +\Delta\nu, +\Delta\nu, -\Delta\nu]$, and where N denotes the number of ions.

When operating the clock with a single ion, we typically employ secular trapping

https://doi.org/10.7795/110.20260227

frequencies of about $\omega_{\text{rad }1,2} = 2\pi \times \{840, 1030\}\,\text{kHz}$ in the radial directions and $\omega_z = 2\pi \times 720\,\text{kHz}$ in the axial direction. We choose the RF power providing the radial confinement such that the resulting temperature increase of the ion trap does not limit the clock's systematic uncertainty. For a given radial confinement, trapping linear Coulomb crystals of multiple ions along the direction of null RF field requires relaxing the DC confinement. Requiring that all motional modes are well-separated from the carrier transitions, with the outermost transitions Zeeman-shifted by about 117 kHz from the line center, sets a lower limit on the axial confinement and therefore the number of ions that can be held in a linear chain. We work with centre-of-mass secular frequencies of $\omega_{\text{ax, COM}} = 2\pi \times 220\,\text{kHz}$, and $\omega_{\text{rad COM }1,2} = 2\pi \times \{1080, 1100\}\,\text{kHz}$, which enables us to hold up to 10 ions in a linear chain. The same confinement was chosen regardless of the exact number of ions.

5.2 Considerations for working with multiple ions

For the simultaneous interrogation of N uncorrelated ions, the frequency instability of the clock is expected to scale as $1/\sqrt{N}$. This reduces the measurement time to achieve a given statistical uncertainty by a factor of N. However, interrogating a linear Coulomb crystal of N ions is not the same as interrogating a single ion N times: The ions do not sit at the same point in space, and consequently they may be subject to different external perturbations. Additionally, they interact via their mutual Coulomb-repulsion, leading to coupled collective motion in the shared trapping potential, as well as different electric field gradients at the different positions of the ions in the chain. These effects, and their consequences for a multi-ion clock, will be discussed in the following.

5.2.1 Effects of collective ion motion

The thermal motion of N trapped ions in a linear Coulomb crystal can be described by N eigenmodes for each of the three spatial dimensions. The derivation of the eigenfrequencies ω_α and corresponding eigenvectors β_α can be found e.g. in [195, 196]. In case of a single ion species, a mode in which all ions participate equally and oscillate in phase with the single-ion secular frequency, called centre-of-mass (COM) mode, exists for each dimension. The COM mode is the lowest frequency mode for

https://doi.org/10.7795/110.20260227

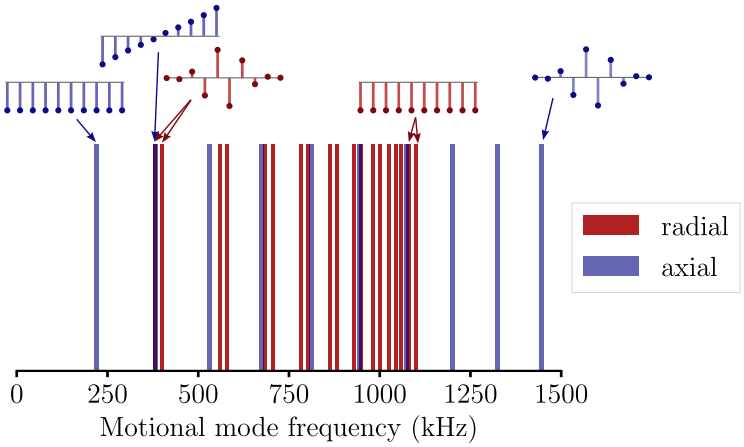

Figure 5.3: Motional mode spectrum for 10 $^{88}Sr^{+}$ ions under our typical trapping conditions. The frequencies of the centre-of-mass motional modes are 220 kHz in the axial direction and 1080 kHz, 1100 kHz in the radial directions. The relative participation of the ions in selected modes are shown pictorially, with the axial motion projected orthogonal to the trap axis for clarity. Calculated using a numerical method provided by Tabea Nordmann [184].

the axial direction, and the highest frequency mode for the radial directions. The calculated motional mode spectrum for a linear chain of 10 $^{88}Sr^{+}$ ions under the typical confinement during clock operation is shown in Figure 5.3.

The relevant frequency shifts associated with thermal ion motion are from the second-order Doppler and DC Stark effects. For $^{88}Sr^{+}$, these two shifts partially cancel at our trap drive frequency, leading to a combined fractional frequency shift on the order of only 1×10^{-18} after Doppler cooling (c.f. subsection 5.3.2). This makes more precise control over the ion temperature, for example via resolved sideband cooling, unnecessary in the context of the systematic uncertainty of the clock.

In the context of the clock's instability, the Debye-Waller effect – the dependence of the Rabi frequency on the motional state [37], needs to be considered. Especially for clock operation with multiple ions, this effect can lead to a degradation of contrast resulting from the finite ion temperatures, as discussed in the following.

When performing laser interrogation of a two-level system with a chain of ions, the carrier Rabi frequency associated with motional quantum number n for ion i participating in m relevant motional modes is [197]

$$\Omega_{i,n} = \Omega_0 \prod_{\alpha=1}^{m} L_n(\eta_{\alpha,i}^2)\, \mathrm{e}^{-\eta_{\alpha,i}^2/2} \tag{5.1}$$

https://doi.org/10.7795/110.20260227

where Ω_0 denotes the Rabi frequency, L_n are the Laguerre polynomials, and $\eta_{\alpha,i}$ is the Lamb-Dicke parameter given by

$$\eta_{\alpha,i} = k_\alpha \beta_{\alpha,i} \sqrt{\frac{\hbar}{2 m_i \omega_\alpha}} \,. \tag{5.2}$$

Here, m_i denotes the mass of the ion and k_α the projection of the wave-vector onto the mode's axis. The probability of ion i to be in the excited state after interacting with the laser for a time t is then [198]

$$P_i = \sum_{\{n_\alpha\}} \left(\prod_{\alpha=1}^{m} p_n(\alpha) \right) \frac{1}{2} (1 - \cos(2\Omega_{n_\alpha} t)) \,, \tag{5.3}$$

where $p_n(\alpha)$ denotes the occupation probability of motional state n, which might be different for different modes α, and the first sum is an m-fold summation over all relevant quantum numbers for each mode. This expression can be hard to evaluate, even numerically, but it may be simplified to

$$P_i = 1/2 \left(1 - \frac{\cos(2\Omega_0 t) + 2\Omega_0 t \sum_\alpha \eta_\alpha^2 \bar{n}_\alpha \sin(2\Omega_0 t)}{1 + (2\Omega_0 t \sum_\alpha \eta_\alpha^2 \bar{n}_\alpha)^2} \right) \,, \tag{5.4}$$

assuming thermal states for all modes, with mean occupation number $\bar{n}_\alpha$ for mode α, expanding to second order in η, and under the approximation $2\Omega_0 t (\bar{n} \eta_{\alpha,i}^2 / 2)^2 \ll 1$ [197]. This is however not always the case for all modes, especially for many ions.

Qualitatively, the dependence on the ions' motional states leads to thermal dephasing of the Rabi oscillation, with the largest effect associated with modes that have a broad distribution $p_n(\alpha)$. For a given temperature after Doppler cooling, these are the low-frequency modes. The reduced maximal excitation probability leads to a reduced contrast, which degrades the clock instability with a linear dependence (c.f. Equation 1.4).

For our current clock configuration, all ions are interrogated with the same Rabi frequency Ω_0, and the servo feedback is based on the sum over the excitations of all ions after a π-pulse. Since ion heating plays a negligible role (c.f. section 4.6), it is safe to assume that for each trap axis all modes have the same temperature after Doppler cooling.

https://doi.org/10.7795/110.20260227

Since only those modes that have a projection along the propagation direction of the probing laser beam are relevant, the choice of this direction with respect to the trap axes becomes important. Trapping multiple ions in a linear Coulomb crystal along the null of micromotion in a linear trap requires relaxation of the axial confinement w.r.t. the radial confinement, which might make interrogation along a radial direction seem attractive. However, when increasing the number of ions for a given external confinement, the additional radial motional modes are at the low end of the spectrum, making scaling to many ions unfavorable, while axial modes are added at higher motional frequencies. We therefore perform axial interrogation, and aim to use as many ions as possible for a given confinement.

To overcome the reduction of carrier excitation probability associated with the lowest-frequency axial motional modes, we employ resolved sideband cooling. Typical results are shown in Figure 5.4 for a chain of eight ions. While without sideband cooling thermal dephasing limits the overall excitation probability at the first maximum of the Rabi oscillation to about 65%, it is increased to 85% after sideband cooling of the COM mode. Additionally cooling the second-lowest motional mode, which has the strongest involvement of the outermost ions, only offers a modest increase well below 1% for excitation with a π-pulse, though the effect, in particular on the outer ions, becomes visible for longer pulses. This shows that thermal dephasing common to all ions dominates the reduction of excitation probability, while the impact from averaging over slightly different effective Rabi frequencies Ω_i is less pronounced.

We therefore employ sideband cooling on only the axial COM mode during clock operation. This has the added advantages that the kinetic energy of all ions is reduced equally, and that the COM mode is well-resolved in the mode spectrum (c.f. Figure 5.3), so that accidental cooling of other modes is avoided. The effect of performing sideband cooling on one out of $3N$ motional modes on the temperature-related frequency shifts is very small since we use at least eight ions during clock operation.

With a typical axial temperature of 0.57 mK after Doppler cooling, $\bar{n}_{\mathrm{COM}} \approx 54$. We use the strong, elliptical beam under 45° with respect to the trap axis and perform continuous resolved sideband cooling using the red sidebands of the cycling $m_J = -1/2 \rightarrow m_J = -5/2$ transition. The transition is weakly broadened with the 1033 nm repumping laser, which is frequency-stabilized on resonance to avoid light shifts. The obtainable cooling speed is limited by the red sidebands of the

https://doi.org/10.7795/110.20260227

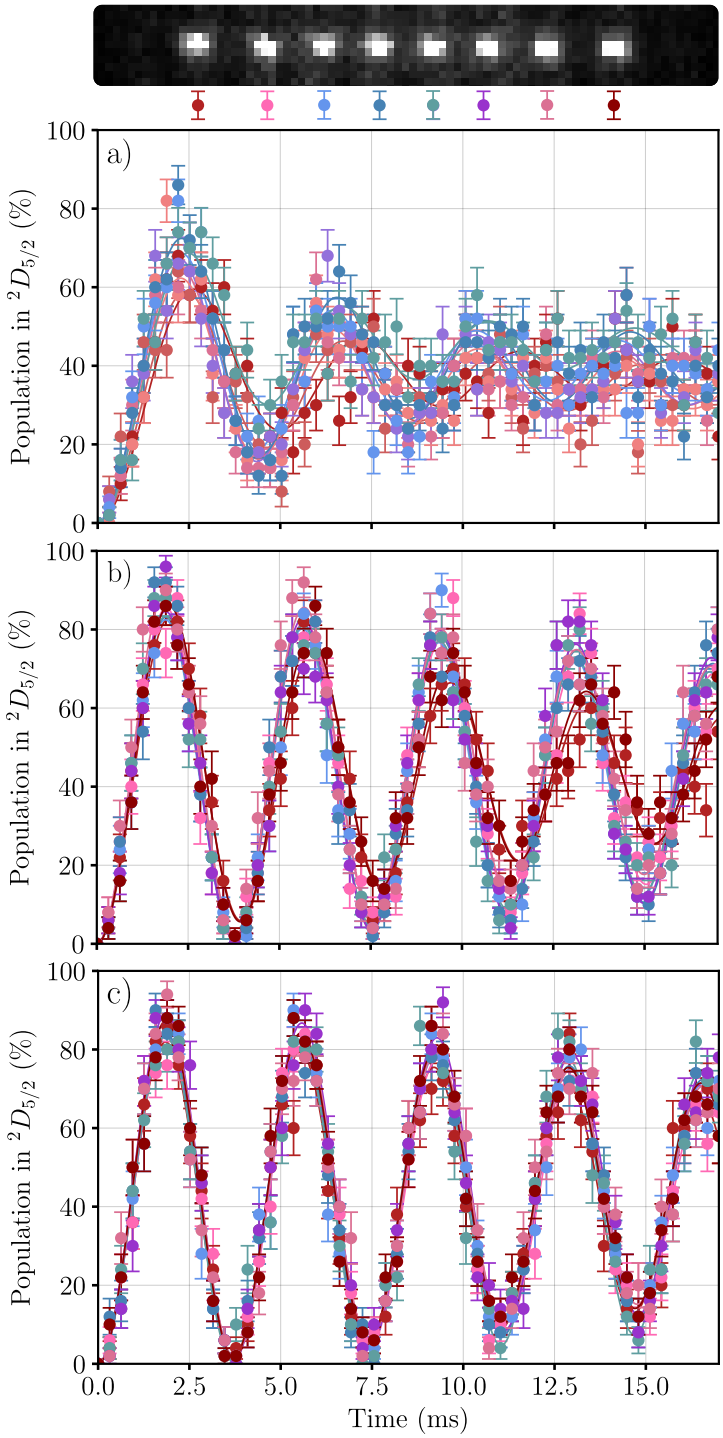

Figure 5.4: Rabi oscillations on the $^2S_{1/2}, m_J = -1/2 \rightarrow {}^2D_{5/2}, m_J = -5/2$ transition taken with eight ions, interrogated with a laser beam propagating along the trap axis. a) After homogeneous Doppler cooling of all ions, without resolved sideband cooling. b) With sideband cooling of the lowest-frequency axial motional mode (centre-of-mass mode) at about 220 kHz. c) With sideband cooling of the centre-of-mass mode and the next higher motional mode (tilt mode) at about 380 kHz. Each point is the average of 50 interrogations, error bars are statistical. The solid lines are fits of the simplified form Equation 5.4.

https://doi.org/10.7795/110.20260227

$-1/3 \rightarrow -3/2$ transition, which are about 50 kHz away. The experimental sequence is optimized for speed and robustness. We start out with 5 ms of cooling on the second-order sideband, followed by 10 ms on the first-order sideband, and another 3 ms on the same sideband with the 1033 nm laser power further reduced by 3 dB. We reliably obtain $\bar{n}_{\mathrm{COM}} \approx 0.3$ based on the relative excitation strengths of the red and blue sidebands.

5.2.2 Ion-resolved information with global addressing

To realize a clock based on the interrogation of multiple ions with a common laser beam, their resonant transition frequencies need to be similar enough for all ions to contribute to the clock signal. This means that differential shifts between the ions need to be smaller than the linewidth. There are two main effects that affect the ions differently depending on their position in the Coulomb crystal: First, a variation of the magnetic field along the ion chain leads to different first-order Zeeman shifts. Second, the ion-ion Coulomb interactions are stronger in the center of the chain than on its edges, leading to position-dependent electric field gradients and resulting quadrupole shifts.

Each of these effects can be overcome experimentally, as discussed in detail below. Typical resulting spectra are shown in Figure 5.5: For our usual interrogation times of 100 ms on the $m_J = \pm 1/2 \rightarrow m_J = \pm 5/2$ components and 250 ms on the $m_J = \pm 1/2 \rightarrow m_J = \pm 3/2$ components, the individual center frequencies of all ions agree within the given resolution and we obtain Fourier-limited collective linewidths.

While a linear variation of a shift along the ion chain primarily causes broadening, leading to reduced instability, shifts that vary nonlinearly from one ion to another distort the collective line asymmetrically and lead to a systematic offset between the frequency realized by the servo and the true average over all ions. To investigate these systematic effects with a higher resolution than that obtained from individual frequency scans, we developed a method to extract ion-resolved frequency shifts directly from the information obtained during clock operation.

Recall that each Zeeman component is interrogated at detunings $\pm\Delta\nu$, selected to provide 50% of the maximum excitation probability for the Fourier-limited line, and the corresponding servo is steered with the feedback signal $\left(0.15\,(n_+ - n_-)/N\right)\Delta\nu$,

https://doi.org/10.7795/110.20260227

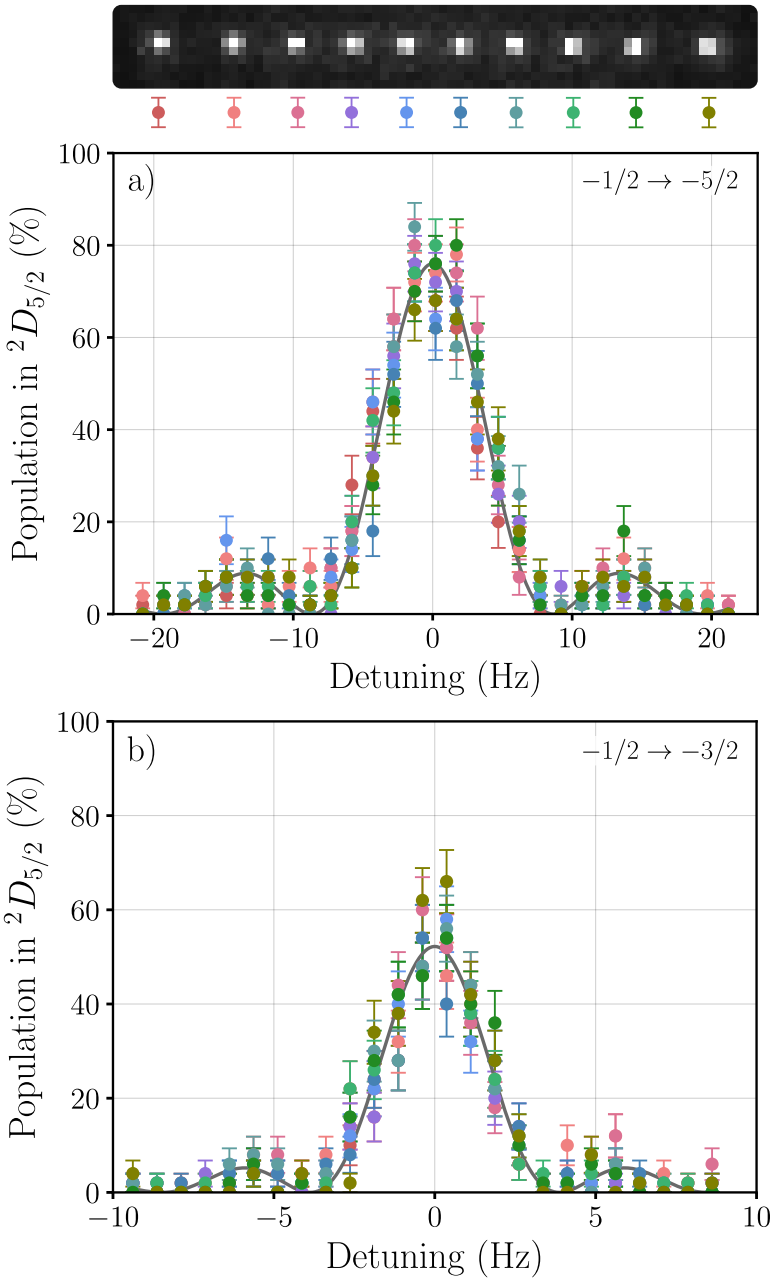

Figure 5.5: Spectra taken with an approximately 55 µm long chain of 10 $^{88}Sr^+$ ions on selected Zeeman components of the $^2S_{1/2} \rightarrow {}^2D_{5/2}$ transition with the interrogation times used during clock operation. a) Spectrum taken on the $m_J = -1/2 \rightarrow m_J = -5/2$ component with a 100 ms long π-pulse. b) Spectrum taken on the $m_J = -1/2 \rightarrow m_J = -3/2$ component with a 250 ms long π-pulse. The difference in excitation probability is due to the radiative decay from the excited state. Each point is the average of 50 repetitions, and the error bars are statistical. The solid line in each case corresponds to a fit of a Fourier-limited line (Equation 5.5) to the average of all ions, with the amplitude and center frequency as free parameters.

https://doi.org/10.7795/110.20260227

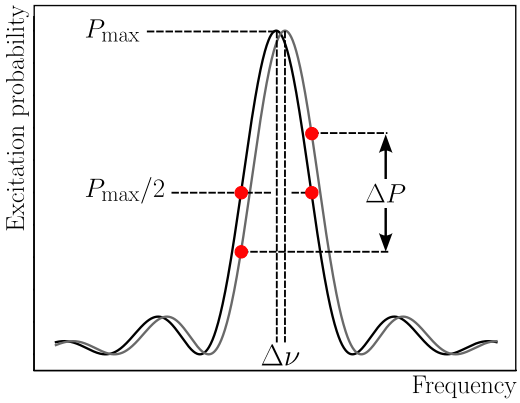

Figure 5.6: Principle of extracting frequency offsets from population imbalances. During the clock sequence, each Zeeman component is probed on the left and right side of the line center, ideally at the half-maximum, and the servo adjusts the center frequency to minimize the imbalance of the excitation probability. A residual average population imbalance $\Delta P \neq 0$ signals an offset $\Delta\nu$ of the line center with respect to the frequency realized by the servo. For a known lineshape, $\Delta\nu$ can be calculated from an observed ΔP.

with $n_+(n_-)$ the total number of successful excitations at positive (negative) detuning. To retain site-resolved information during multi-ion operation, we record the individual excitation imbalances $(n_+ - n_-)_i$ for each ion i and each clock cycle. We can translate a time-averaged excitation imbalance $\Delta P_i = \langle (n_+ - n_-)_i \rangle_t$ to a frequency offset with respect to the line center according to the servo based on all ions, using the known lineshape. The principle is illustrated in Figure 5.6. We employ this technique to investigate shift effects in an ion-resolved fashion and with high frequency resolution.

This approach depends on reliable knowledge of the lineshape of the individual ions, and the differential shifts across the ion chain being constant over the averaging time. We use the analytic description of the excited state probability P for a coupled two-level system (see e.g. [199])

$$P = P_{\max} \frac{\Omega^2}{\Omega^2 + \Delta^2} \sin^2\left(\frac{1}{2}\sqrt{\Omega^2 + \Delta^2}\, t\right) , \tag{5.5}$$

where Δ denotes the detuning from resonance, and we assume a perfect π-pulse, i.e. $\Omega = \pi/t$ for a specific interrogation time t. The maximal excitation probability $P_{\max}$ is approximated by twice the excitation probability found at the interrogation points for each ion, which is valid as long as the frequency shifts between the ions are small compared to the linewidth. Numerically solving the associated master equation using the python package qutip shows that the effect the 391 ms excited state lifetime

https://doi.org/10.7795/110.20260227

has on the line shape (except for a reduction of the excitation probability) is negligible for our maximal interrogation time of 250 ms. The same holds true for small deviations from the ideal π-pulse condition. We have not observed any variations of the line shape over time based on regular frequency scans. The recorded single-ion excitation imbalances display white-noise behavior based on the analysis of their Allan deviation, indicating that the shifts we investigate remain constant on the timescales of typical measurement runs (a few days). The same holds true for the overall excitation probabilities.

The results obtained with this method will be presented in the context of the frequency shifts that made it necessary in the first place: the quadrupole shift and the first-order Zeeman shift.

5.2.3 Quadrupole shift and its variation along the ion chain

The quadrupole shift results from the interaction of an electric quadrupole moment $\Theta^{(2)}$ with an electric field gradient $\nabla E^{(2)}$, corresponding to a Hamiltonian:

$$H_{\mathrm{QS}} = \nabla E^{(2)} \cdot \Theta^{(2)} = \sum_{q=-2}^{2} (-1)^q \nabla E^{(2)}_q \Theta^{(2)}_{-q} \tag{5.6}$$

with the components in the spherical basis [67]

$$\nabla E^{(2)}_0 = -\frac{1}{2}\frac{\partial E_z}{\partial z}\,, \tag{5.7}$$

$$\nabla E^{(2)}_{\pm 1} = \pm\frac{\sqrt{6}}{6}\frac{\partial E_\pm}{\partial z} = \pm\frac{\sqrt{6}}{6}\partial_\pm E_z\,, \tag{5.8}$$

$$\nabla E^{(2)}_{\pm 2} = -\frac{\sqrt{6}}{12}\partial_\pm E_\pm\,, \tag{5.9}$$

where $E_\pm \equiv E_x \pm iE_y$, $\partial_\pm \equiv \partial/\partial x \pm i\partial/\partial y$, and E_x, E_y, E_z denote the components of the electric field.

As the electron distribution of the ground state is spherically symmetric, the relevant quadrupole moment is that of the excited clock state. For the $^2D_{5/2}$ state in $^{88}\mathrm{Sr}^+$, the matrix element $\Theta \equiv \langle J, m_j = J|\,\Theta^{(2)}_0\,|J, m_J = J\rangle$ has been measured to be $2.6(3)\,ea_0^2$ [200], which is significantly larger than those associated with the relevant clock transitions in $^{171}\mathrm{Yb}^+$ (c.f. section 2.1). The clock transitions in In^+ and Al^+ feature over five and six orders of magnitude smaller quadrupole moments

https://doi.org/10.7795/110.20260227

respectively [201]. In fact, the comparatively large quadrupole moment, and the first-order Zeeman sensitivity, might make $^{88}Sr^{+}$ seem like an unattractive candidate for a multi-ion clock at first glance, at least without employing dynamical decoupling schemes for shift suppression [202].

While in a spherically symmetric single-ion trap electric field gradients stem only from stray fields, the harmonic DC confinement of a linear ion trap leads to a comparatively large electric field gradient, which for our configuration can lead to a quadrupole shift of several Hz, depending on the magnetic field orientation. For a chain of ions, the electric field gradients due to their mutual Coulomb interaction are of the same order of magnitude and have to be considered additionally. This warrants taking a closer look at the details of this effect, and the consequences for a multi-ion optical clock.

We start by deriving relevant electric field gradients for an ion chain in a linear Paul trap, based on the treatment in [174]. The potential due to the static voltage used for axial confinement is given by

$$\Phi_{\mathrm{dc}} = \frac{m\omega_z^2}{2e}\left[z^2 - \alpha x^2 - (1-\alpha)y^2\right] , \tag{5.10}$$

with the single-ion axial secular frequency ω_z and the factor $\alpha \approx 1/2$, the exact value of which depends on the trap geometry and the voltage U_t. The resulting electric field gradients are

$$\frac{\partial E_{\mathrm{trap}}}{\partial x, y} = \frac{m\omega_z^2}{2e}\left[1 \pm (2\alpha - 1)\right] e_{x,y} , \tag{5.11}$$

$$\frac{\partial E_{\mathrm{trap}}}{\partial z} = \frac{m\omega_z^2}{e} e_z , \tag{5.12}$$

where e_i, $i \in \{x, y, z\}$ denote the unit vectors.

Next, let's consider the effect of the ions in a linear crystal have on each other. Starting from the potential of a singly-charged point-like ion j some distance z_j along the trap axis away

$$\Phi_{\mathrm{ion}} = \frac{e}{4\pi\epsilon_0(z - z_j)} , \tag{5.13}$$

we can see that the z-component of the contribution from other ions to the electric field gradient experienced by ion i is

https://doi.org/10.7795/110.20260227

$$\frac{\partial E_{\text{ions},i}}{\partial z} = \sum_{j\neq i} \frac{2e}{4\pi\epsilon_0 \left|z_i - z_j\right|^3} e_z = \frac{2m\omega_z^2}{e} \sum_{j\neq i} \frac{1}{\left|u_i - u_j\right|^3} e_z \,, \tag{5.14}$$

where the ion positions z_i are given by the equilibrium positions in the harmonic potential, and $u_i = z_i/l$ are dimensionless, rescaled with [195]

$$l^3 = \frac{e^2}{4\pi\epsilon_0 m\omega_z^2} \,, \tag{5.15}$$

such that they depend only on the number of ions and not the the ion mass or secular frequency. Due to the Laplace condition and cylindrical symmetry

$$\frac{\partial E_{\text{ions},i,x}}{\partial x} = \frac{\partial E_{\text{ions},i,y}}{\partial y} = -\frac{1}{2}\frac{\partial E_{\text{ions},i,z}}{\partial z} \,. \tag{5.16}$$

Combining the contributions from the confining voltage and the other ions, one obtains the following components of $\nabla E_i^{(2)}$ acting on ion i:

$$\left(\nabla E_i^{(2)}\right)_0 = \frac{m\omega_z^2}{e}\left(\frac{1}{2} + \sum_{j\neq i}\frac{1}{\left|u_i - u_j\right|^3}\right) \,, \tag{5.17}$$

$$\left(\nabla E_i^{(2)}\right)_{\pm 1} = 0 \,, \tag{5.18}$$

$$\left(\nabla E_i^{(2)}\right)_{\pm 2} = \frac{1}{\sqrt{6}}\frac{m\omega_z^2}{e}\left(\frac{1}{2} - \alpha\right) \,. \tag{5.19}$$

Finally, we need to transform the coordinate system from one where z is along the ion chain, to one where z' is parallel to the magnetic field B and therefore the quantization axis. Using the transformation matrices for rotating the rank 2 spherical tensors, which are for example given in [203], one can obtain this by a rotation by Φ around z, which leaves $\left(\nabla E_i^{(2)}\right)_0$ unchanged, followed by a rotation by θ around the new y'-axis, yielding

$$\begin{aligned}\left(\nabla E_i^{(2)}\right)''_0 &= \sqrt{\frac{3}{8}}\sin^2\theta\left(\left(\nabla E_i^{(2)}\right)'_{+2} + \left(\nabla E_i^{(2)}\right)'_{-2}\right) + \frac{1}{2}\left(3\cos^2\theta - 1\right)\left(\nabla E_i^{(2)}\right)_0 \\ &= \frac{m\omega_z^2}{e}\left[\frac{\sin^2\theta\cos 2\phi}{2}\left(\frac{1}{2} - \alpha\right) + \frac{3\cos^2\theta - 1}{2}\left(\frac{1}{2} + \sum_{j\neq i}\frac{1}{\left|u_i - u_j\right|^3}\right)\right] \,.\end{aligned} \tag{5.20}$$

The first term is the same for all ions, while the second term leads to a different

https://doi.org/10.7795/110.20260227

quadrupole shift depending on the ion position in the linear Coulomb crystal. While a constant quadrupole shift cancels perfectly in our averaging scheme, this is no longer the case for the contribution that varies along the ion chain: The nonlinear variation leads not only to line broadening, but also to a frequency offset due to the asymmetry of the resulting collective line.

Taking into account the scaling of the quadrupole matrix element with the quantum number m_J as

$$\Theta(J, m_J) = \frac{3m_J^2 - J(J+1)}{J(2J-1)}\,\Theta(J, m_J = J)\,, \tag{5.21}$$

we can conveniently parametrize the quadrupole shift for ion i resulting from ion-ion interactions (i.e. the second term in Equation 5.20) as

$$\Delta\nu_{QS,i} = \Delta\nu_{QS}(\theta, J)\,(m_J^2 - J(J+1)/3)\left(\sum_{j\neq i}\frac{1}{|u_i - u_j|^3}\right)\,, \tag{5.22}$$

where the second term evaluates as -2/3 for $m_J = 3/2$ and +10/3 for $m_J = 5/2$. Here, we have defined

$$\Delta\nu_{QS}(\theta, J) = \frac{2m\omega_z^2}{h\,e}\frac{3\cos^2\theta - 1}{2}\frac{3}{J(2J-1)}\,\Theta\,, \tag{5.23}$$

which is independent of m_J, i, and the total number of ions. This factor sets the scaling for the amount of quadrupole shift variation (in Hz) across the ion chain at a specific magnetic field angle θ.

We set the magnetic field direction such that its angle with respect to the trap axis is close to $\theta = \arccos(1/\sqrt{3}) \approx 54.7^\circ$ for clock operation with multiple ions, thereby minimizing $\Delta\nu_{QS}$ and suppressing the variation of the quadrupole shift between the different ions. The result is depicted in Figure 5.7. The overall tensor shift is extracted from the respective mean frequencies $\nu_{5/2}$ and $\nu_{3/2}$ of the $\pm1/2 \rightarrow \pm3/2$ and $\pm1/2 \rightarrow \pm5/2$ Zeeman pairs during clock operation according to $(3/10)(5/6)(\nu_{5/2} - \nu_{3/2})$. Small imbalances of the excitation probabilites of the individual ions are translated into frequency offsets from the centre of each servo as explained in subsection 5.2.2. We find a permanent offset of about 0.2° between the z-axis of the coordinate system defined by the magnetic field coils and the trap axis, leading to $\Delta\nu_{\mathrm{QS}} = 4.2(3)\,\mathrm{mHz}$. After adjusting the magnetic field setting to account for this offset, we typically find values of $\Delta\nu_{\mathrm{QS}}$ that are compatible with zero within the resolution obtained in a typical clock run of a few days. Note that

https://doi.org/10.7795/110.20260227

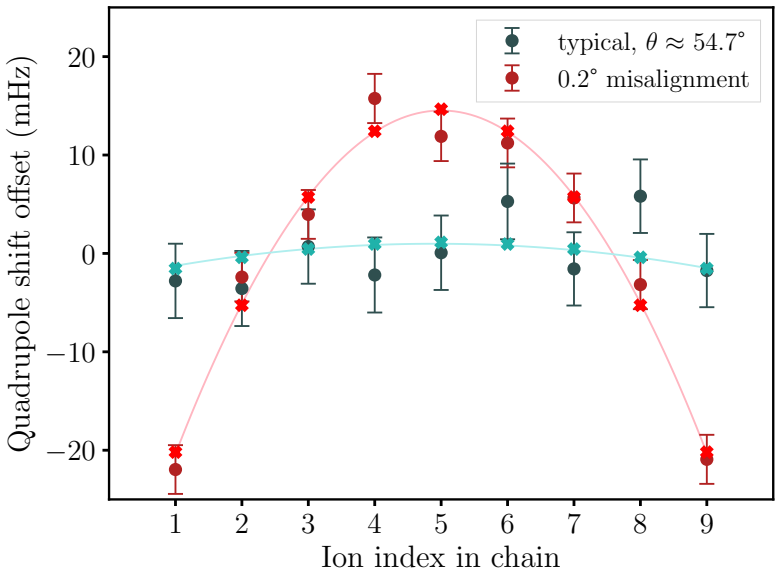

Figure 5.7: Ion-resolved investigation of quadrupole shift variation. Data points are extracted from data accumulated during clock operation with the method introduced in subsection 5.2.2. Error bars correspond to statistical uncertainties, obtained from extrapolating fits to the Allan deviations of the respective population imbalances to the full measurement time. The results of two measurement runs are shown: One for typical magnetic field orientation close to the optimum, with about 4.8×10^4 s of data, and one for an initial misalignment of the magnetic field angle by about 0.2° with about 11.6×10^4 s of data. Crosses are the result of a discrete fit of Equation 5.22 to the data, yielding $\Delta\nu_{\mathrm{QS}} = 0.3(4)$ mHz and $\Delta\nu_{\mathrm{QS}} = 4.2(3)$ mHz, respectively. Average quadrupole shifts of 101 mHz and 201 mHz respectively have been subtracted for clarity. Lines are to guide the eye.

the ion-ion quadrupole shift also contributes an average term to the quadrupole shift, i.e. $\sum_i \Delta\nu_{QS,i} \neq 0$, that has been subtracted in the figure. Note also that a positive value of $\Delta\nu_{\mathrm{QS}}$, as obtained for $\theta < \arccos(1/\sqrt{3})$, corresponds to a negative curvature across the ion chain, as the effect is largest in its center.

For each of the Zeeman components interrogated during the clock sequence, the distorted lineshape results in an offset between the frequency realized by our servo sequence, i.e. the frequency minimizing the population imbalance for interrogation at equal frequency offsets to its left and right, and the true average over all line centers. Some degree of cancellation is obtained for the overall clock output, i.e. the weighted mean of the two Zeeman pairs. However, as the frequency offset on an individual component scales nonlinearly with both the sensitivity to the quadrupole shift and the interrogation time, the amount of suppression, or conversely the residual effect on the overall clock output is not obvious.

https://doi.org/10.7795/110.20260227

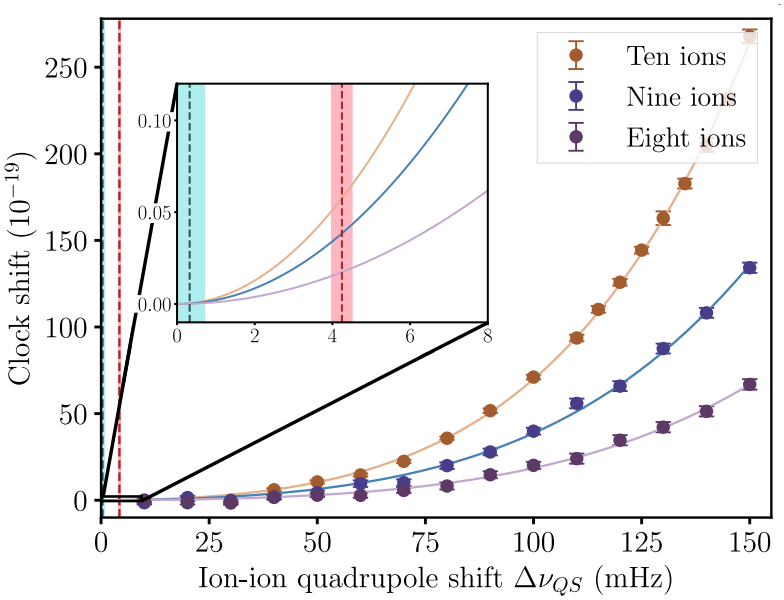

Figure 5.8: Frequency shift due to line pulling as a function of the ion-ion quadrupole shift scaling factor $\Delta\nu_{QS}$. Each point corresponds to a Monte-Carlo simulation of the clock servo with the same interrogation times and weights as in the experiment. Error bars correspond to statistical uncertainties due to the finite number of simulated clock cycles. Negative values of $\Delta\nu_{QS}$ (not shown) lead to corresponding negative frequency shifts. The solid lines are fits of $ax^2 + bx^4$. The green and red dashed vertical lines and shaded areas correspond to the experimental examples shown in Figure 5.7: Nine ions and $\Delta\nu_{\mathrm{QS}} = 0.3(4)\,\mathrm{mHz}$ and $\Delta\nu_{\mathrm{QS}} = 4.2(3)\,\mathrm{mHz}$ respectively. The latter corresponds to a clock shift of $0.038(5) \times 10^{-19}$.

We investigate the residual frequency shift using Monte-Carlo simulations of the clock servo with the same interrogation times and weights used in the experiment for different amounts of ion-ion quadrupole shift. The results are depicted in Figure 5.8. The dependence of the overall frequency offset on $\Delta\nu_{QS}$ is well-described by combining a quadratic and a quartic term. The simulations are performed for eight to ten ions. The frequency shifts for the example measurement runs depicted in Figure 5.7 are obtained: For nine ions with $\Delta\nu_{\mathrm{QS}} = 0.3(4)\,\mathrm{mHz}$ and $\Delta\nu_{\mathrm{QS}} = 4.2(3)\,\mathrm{mHz}$ respectively, fractional clock shifts of $0.0002(5) \times 10^{-19}$ and $0.038(5) \times 10^{-19}$ are obtained. The magnetic field angle is passively much more stable than the initial misalignment of 0.2°, which, even with ten ions, would lead to a frequency shift below 0.1×10^{-19}. Even without the detailed analysis of this effect for every future measurement run, we have thus suppressed the maximal resulting frequency shift to a level that is irrelevant compared to the leading frequency shifts, which will be discussed in section 5.3.

https://doi.org/10.7795/110.20260227

5.2.4 Magnetic field gradient

We observe a linear magnetic field gradient on the order of 0.1 nT/100 µm along the ion chain, leading to differential first-order Zeeman shifts of up to a few Hz between the leftmost and rightmost ions in a Coulomb crystal. When actively setting different magnetic field orientations, the gradient changes as different sets of coils contribute to the overall magnetic field. We use a dedicated set of magnetic field coils connected in an anti-Helmholtz configuration to compensate for this gradient and avoid the associated line broadening.

The local magnetic field strength is obtained from the splitting frequencies of the different Zeeman components using their known first-order sensitivities. Its variation along the trap axis can be measured in different ways: By moving a single ion along the trap axis and performing clock operation at each position, by performing a frequency scan on any one of the Zeeman components and determining the line centers for different ions in a Coulomb-crystal, or by analysing the ion-resolved population imbalances recorded during clock operation (c.f. subsection 5.2.2). The last option is the most precise, and even allows for real-time monitoring during clock operation.

We observe that the residual magnetic field gradient stays constant during our measurement runs and leads to a variation at or below about 10^{-11} T across the ≈ 50 µm long ion chain. As we do not observe any non-linear variation along the ion chain, there are no line pulling effects that would lead to frequency offsets.

5.3 Preliminary shift and uncertainty evaluation

To assess the accuracy of the newly established optical clock, all effects that could lead to a shift of the local oscillator frequency with respect to the ideal, unperturbed transition frequency have to be evaluated carefully. We have already seen that the effects of shift variation along the ion chain are suppressed to well below 0.1×10^{-19}. In the following, remaining relevant frequency shifts and their associated systematic uncertainties are discussed. Their determination largely follows well-established methods. In particular, a detailed discussion of different frequency shifts in $^{88}Sr^{+}$ clocks can be found in [43, 194]. The preliminary uncertainty budget summarizing all relevant shifts and uncertainty contributions can be found at the end of this

https://doi.org/10.7795/110.20260227

section. We obtain an overall fractional frequency uncertainty of 5.3×10^{-19} for the clock operating with eight to ten ions, and 6.5×10^{-19} for the clock operating with a single ion. The difference is caused by a mitigation of collisional shifts through the detection of crystal melting.

5.3.1 Blackbody-radiation shift

By far the largest frequency shift results from the thermal radiation of the room-temperature environment. It is one example of a quadratic Stark shift, a shift due to interaction of the atomic dipole operator $\boldsymbol{d}$ with an electric field $\boldsymbol{E}$. An expression for this shift can be obtained from the Hamiltonian $-\mathbf{dE}$ in second-order perturbation theory, yielding, for a single atomic level characterized by the quantum numbers J, m_J [67]

$$\Delta\nu_{\text{Stark2}} = -\frac{|\mathbf{E}|^2}{h}\left(\frac{\alpha_S}{2} + \frac{\alpha_T}{4}\,\frac{3m_J^2 - J(J+1)}{J(2J-1)}\,(3\cos^2\beta - 1)\right). \tag{5.24}$$

Here, α_S and α_T denote the scalar and tensor polarizabilities, which depend on the wavelength of the perturbing radiation, and β denotes the angle between the quantization axis and the electric field vector.

The perturbation from the blackbody radiation (BBR) of the environment is typically assumed to be isotropic, so that the tensorial term can be neglected. At room temperature, close to 300 K, the BBR shift for an atomic transition can then be approximated by [168, 204]

$$\Delta\nu_{\text{BBR}} \approx -\frac{1}{2h}\left\langle E^2\right\rangle_T \Delta\alpha_0\,(1+\eta)\,, \tag{5.25}$$

with the mean square field

$$\left\langle E^2\right\rangle_T = \left(831.94\,\frac{\text{V}}{\text{m}}\right)^2 \left(\frac{T}{300\,\text{K}}\right)^4. \tag{5.26}$$

Here, $\Delta\alpha_0$ denotes the DC-value of the differential scalar polarizability, and η is a small correction that accounts for the response of the atomic levels to the spectrum of the thermal radiation.

Recent measurements [169] have further reduced the uncertainty of the static differential scalar polarizability in $^{88}\text{Sr}^{+}$ by a factor of 3.5 from that in [168], obtain-

https://doi.org/10.7795/110.20260227

ing $\Delta\alpha_0 = -4.8314(20) \times 10^{-40}\,\mathrm{Jm^2/V^2}$, and we use the fixed correction factor $\eta = -0.00951(15)$ [168]. The uncertainty of the DC polarizability contributes a fractional uncertainty of 2.23×10^{-19} to the BBR shift for our observed average temperature of 296.75 K, and the correction contributes 0.82×10^{-19}.

The temperature at the position of the ions is evaluated in a time-resolved fashion as described in section 4.7. The average BBR shift is about 240 mHz, or in fractional units 5.38×10^{-16}. The temperature uncertainty of 50.7 mK contributes a fractional frequency uncertainty of 3.68×10^{-19}. The overall uncertainty of the BBR shift is then 4.4×10^{-19}.

5.3.2 Thermal ion motion

There are two relevant frequency shifts related to thermal ion motion: the second-order Doppler shift and the quadratic DC Stark shift. The second-order Doppler shift can be written as

$$\frac{\Delta\nu_{\mathrm{Dop2}}}{\nu_0} = -\frac{1}{2}\frac{\langle v^2\rangle}{c^2}\,, \tag{5.27}$$

where ν_0 is used to denote the optical transition frequency. The average squared velocity can be related to the ion temperature: A contribution of $1/2k_\mathrm{B}T$, with k_B the Boltzmann constant, is associated with the secular motion in each of the three directions, and, in a linear trap under the pseudopotential approximation, with each of the two radial directions that are affected by intrinsic micromotion, yielding

$$\frac{\Delta\nu_{\mathrm{Dop2}}}{\nu_0} = -\frac{3}{2}\frac{k_\mathrm{B}T_{\mathrm{avg}}}{mc^2} - \frac{2}{2}\frac{k_\mathrm{B}T_{\mathrm{rad}}}{mc^2}\,, \tag{5.28}$$

where we have introduced the ion temperature T_{avg} averaged over all three directions, and T_{rad} averaged over the two radial directions. The quadratic DC Stark shift results from the finite mean squared trap field $\langle E^2\rangle$ that is sampled by the ions due to their motion in the trap. It is given by

$$\frac{\Delta\nu_{\mathrm{Stark2}}}{\nu_0} = -\frac{\Delta\alpha_0}{h\nu_0}\,\frac{2}{2}k_\mathrm{B}T_{\mathrm{rad}}\,\frac{m\Omega_{\mathrm{RF}}^2}{e^2} \tag{5.29}$$

Due to the negative sign of the static scalar polarizability $\Delta\alpha_0$, a degree of mutual cancellation of these two shifts is obtained for a suitable trap drive frequency.

To accurately determine the temperature of the ions after laser cooling, we need to know the geometric projections of the probing beams onto the trap axes. Assuming

https://doi.org/10.7795/110.20260227

negligible variation of the residual ion motion after Doppler cooling from shot to shot, we can measure the sideband/carrier excitation ratios using laser beams from different directions, and solve for the angle of interest. Laser beams passing through the ion trap in the horizontal are very tightly constrained in the vertical by the 50 mm long trap wafers that are 1 mm apart, so we assume their angle with respect to the horizontal (yz-plane) to be 0°. Additionally, the axial clock laser beam has been aligned to provide similar Rabi frequencies for chains of up to 16 ions, and is found not to excite the radial sidebands, so that it is justified to assume its alignment along the z-axis.

We determine the angle ϕ between the beam used for optical pumping of $^{88}Sr^{+}$ and the horizontal (c.f. Figure 4.6) by measuring the excitation fractions r_{ax} of the horizontal clock beam and r_{pump} of the pump beam, which relate to the angle as

$$\cos(\phi) = \sqrt{\frac{r_{\mathrm{pump}}}{r_{\mathrm{ax}}}}\,. \tag{5.30}$$

We obtain ϕ =44(2)°, compatible with the planned angle of 45°.

We determine the angles of the radial trap axes with respect to the horizontal by comparing the excitation fractions of the pump beam and an auxiliary, purely radial spectroscopy beam set up for this purpose in the horizontal, along the y-axis. We denote the angle between the radial axis with the smaller trapping frequency ω_{r1} and the horizontal as α (c.f. Figure 4.13), meaning the angle between the other radial trap axis and the horizontal is $90°-\alpha$. From geometric considerations we obtain

$$\tan(\alpha) = \sqrt{\frac{r_{\mathrm{pump},\,\omega_{r1}}}{r_{\mathrm{rad},\,\omega_{r2}}\sin^2(\phi)}} = \sqrt{\frac{r_{\mathrm{rad},\,\omega_{r2}}\sin^2(\phi)}{r_{\mathrm{pump},\,\omega_{r2}}}}\,, \tag{5.31}$$

where r_{rad} denotes the excitation fractions of the radial, horizontal beam. We perform independent measurements for each of the two trapping frequencies ω_{r1} and ω_{r2}. By averaging the compatible results, we obtain an angle of $\alpha = 56(2)°$. This is compatible with an angle of 57.1° predicted by modeling of the trapping potential in [175]. Note that this angle is modified by the interplay of the DC voltages applied to the trap segment and the neighboring segments. The measured value corresponds to a dominating axial confining voltage, with $U_e = U_t = 0\,\mathrm{V}$ within the segment.

We measure the temperature of a single ion after Doppler cooling in all three directions using the relative excitation probability of the carrier and corresponding sideband transitions [197]. Here, the mean thermal excitation quantum number $\bar{n}$

https://doi.org/10.7795/110.20260227

is given by $\bar{n} = r/\eta^2$, where r denotes the ratio of excitations on a red sideband to its carrier, and the Lamb-Dicke factor η contains the geometric projections of the probing beam onto the relevant trap axis. We ensure to use weak pulses with less than 20% excitation on the carrier transition. We choose the employed Zeeman components such that the probed sidebands are not close to any other carrier or sideband transitions, and obtain $\bar{n}_{ax} = 16.0(0.5)$, $\bar{n}_{\mathrm{rad1}} = 16.5(1.2)$, $\bar{n}_{\mathrm{rad2}} = 22.9(2.3)$. Here, the uncertainties correspond to statistical measurement uncertainties, limited by the number of excitations on the red sideband, and are calculated assuming a Poissonian distribution of the number of excitations. With the trapping frequencies $\omega_z = 2\pi\times717\,\mathrm{kHz}$ and $\omega_{\mathrm{rad}\ 1,2} = 2\pi\times\{821, 1086\}\,\mathrm{kHz}$ at the time of the measurement we obtain the corresponding temperatures $T_{\mathrm{ax}} = 0.57(2)\,\mathrm{mK}$, $T_{\mathrm{rad},\ 1} = 0.67(5)\,\mathrm{mK}$ and $T_{\mathrm{rad},\ 2}$ =1.15(11) mK. The difference between these temperatures is due to the different projections of the laser beam used for Doppler cooling onto the trap axes. In the overall uncertainty of the average radial and average total temperatures, we additionally include the uncertainties of the projection angles, as well as a 15% uncertainty based on observed variations of ion fluorescence over the almost year-long measurement period. We obtain $T_{\mathrm{rad}} = 0.91(22)\,\mathrm{mK}$ and $T_{\mathrm{avg}} = 0.80(16)\,\mathrm{mK}$. These temperatures are compatible with those obtained from the analysis of thermal dephasing when performing Rabi flops on a carrier transition.

Light for Doppler cooling homogeneously addresses all ions in the linear chain, with variations of fluorescence between the ions around 5%. It is therefore adequate to assume each ion has the same temperatures we have determined for a single ion after Doppler cooling, given their uncertainties of over 20%, which include an uncertainty associated with much larger variations of fluorescence. The motion of a chain of N ions can be described by $3N$ eigenmodes, and we perform sideband cooling of the axial COM mode during clock operation with multiple ions (c.f. subsection 5.3.2). To assess frequency shifts resulting from thermal motion, we assume this mode is cooled completely, i.e. the temperature of all N ions is reduced by a factor of $(3N-1)/(3N)$. Assigning the entire initial temperature of the sideband-cooled mode as an additional uncertainty to include the possibility of residual population in high-lying motional states as well as slight variations in cooling efficiency does not significantly contribute to the overall temperature uncertainty.

With the ion temperatures determined above, and a trap drive frequency of $\Omega_{\mathrm{RF}} = 2\pi \times 14.242\,\mathrm{MHz}$, we obtain a second-order Doppler shift of -2.21×10^{-18} and a Stark shift of 0.94×10^{-18} for a single ion. The combined shift due to thermal motion is -1.27×10^{-18}, with an uncertainty of 2.6×10^{-19}. For eight to ten ions, with the

https://doi.org/10.7795/110.20260227

energy of one motional mode removed via sideband cooling as discussed above, the combined shift is -1.24×10^{-18}, also with an uncertainty of 2.6×10^{-19}.

5.3.3 Excess micromotion

The net shift from excess micromotion to first order in the trap drive frequency is given by [168, 194]:

$$\frac{\Delta\nu_{\mathrm{EMM}}}{\nu_0} = -\frac{1}{2}\left[\frac{\Delta\alpha_0}{h\nu_0} + \left(\frac{e}{m\Omega_{\mathrm{RF}}c}\right)^2\right]\langle E^2\rangle \tag{5.32}$$

Here, the first term is the scalar Stark shift, and the second term the second-order Doppler shift. Our trap drive frequency is close to the "magic" RF frequency of 14.39 MHz [169], where these two shifts cancel completely. Contributions from higher-order trap drive harmonics are neglected since they are suppressed by almost three orders of magnitude for our trapping parameters. The tensor Stark shift is canceled by our averaging scheme, since it has the same m_J-dependence as the quadrupole shift.

We determine the residual RF field amplitude experienced by the ions due to excess micromotion using the photon-correlation technique [186] with three mutually orthogonal laser beams. We find a field amplitude due to excess axial micromotion of 65(10) V/m. The amount of axial micromotion is constant over time within the given uncertainty, which results from long-term variations of the intensity from the probing laser beams. In the other two directions, micromotion compensation generally yields an RF field amplitude close to zero at the beginning of a measurement run. With measurement runs of up to several days and only intermittent monitoring of excess micromotion during these measurements, we use the maximum value of the field amplitudes observed after any measurement, in each of the two orthogonal directions, to determine the uncertainty of the shift. We obtain 58 V/m in x-direction and 90 V/m in y-direction from the maximum observed modulation, leading to a maximal radial field amplitude of 107 V/m.

We obtain a shift of -0.3×10^{-19} (from the constant axial micromotion) and an uncertainty of 0.9×10^{-19} (from the maximal observed amount of micromotion). Recently, we have implemented regular automatic monitoring and compensation of excess micromotion, which further reduces this frequeny shift and its uncertainty.

https://doi.org/10.7795/110.20260227

5.3.4 Collisions

Collisions of the ions with background gas atoms or molecules may lead to frequency shifts via two effects: First, heating of the ion results in an additional contribution to the second-order Doppler shift. Second, the superposition of ground and excited clock state may be perturbed with a phase shift.

An elaborate model taking both effects into account has been developed for the Al^+ ion clock at NIST [172]. An estimate for other ion species is also provided. Second-order Doppler shifts are found to be very small in $^{88}Sr^+$ due to its relatively large mass. An estimate for phase shifts in $^{88}Sr^+$ yields $\pm 11.9 \times 10^{-19}$ for a background pressure of 16 nPa. Re-scaling the given value to the background pressure of 4.5 nPa we obtained from our measured crystal reorder rate assuming H_2 background gas, we would obtain a fractional frequency uncertainty of 3.3×10^{-19}. However, the dependence on different experimental parameters is not provided in [172], since results are obtained with Monte-Carlo simulations.

Here, we therefore make use of the simple worst-case estimate in [205], where a frequency shift of 0.15Γ is obtained for a $\pi/2$ phase shift in each collision. Since this phase change would be random in each collision and cannot be determined experimentally, the associated worst-case frequency shift has to be fully considered as the uncertainty. With a measured collision rate of $\Gamma \approx 1.16 \times 10^{-3}$ /s/ion (c.f. section 4.1), we obtain a fractional uncertainty of 3.9×10^{-19}.

Part of the possible shift due to collisions is mitigated through a protective mechanism in the control sequence: A valid interrogation cycle that contributes to steering of the clock requires all ions to be detected as bright after re-pumping from the $^2D_{5/2}$ excited state. If this is not the case, for example due to crystal melting or an increased ion temperature after a collision, the control system continues to iterate cooling cycles, and after 50 unsuccessful cooling cycles triggers a "rescue" sequence that reduces the trap confinement and illuminates the ions with strong, red-detuned cooling laser light.

We find that for a single ion, close to all clock cycles are valid, and consequently collisions remain generally undetected. In the case of multiple ions, we expect close to all collisions to lead to crystal melting at our trapping conditions (c.f. section 4.1). The crystal may however be recovered during the cooling/detection period, in which case the clock cycle may be registered as valid, if enough fluorescence is collected from each ion. Almost all failed cooling cycles eventually lead to triggering of the

https://doi.org/10.7795/110.20260227

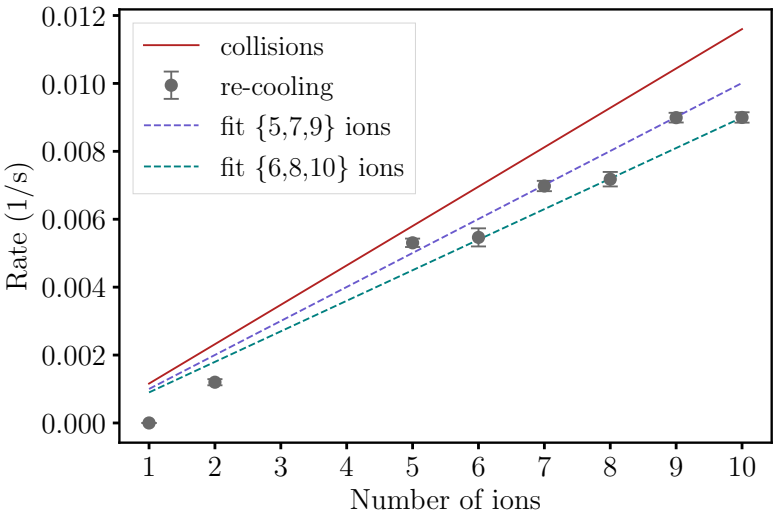

Figure 5.9: Comparison of detected and total collision rates for different numbers of ions. The red line corresponds to the total collision rate of 1.16×10^{-3}/s/ion (c.f. section 4.1). Points correspond to measured rates of re-cooling events that are triggered by consecutive invalid clock cycles. Fits are linear, assuming a fixed fraction of collisions leads to re-cooling. The results indicate a fraction of about 86% during clock operation with 5, 7, or 9 ions, and a slighty lower fraction of 78% during clock operation for 6, 8, or 10 ions. For a single ion, there are no re-cooling events.

re-cooling or "rescue" sequence. We investigate the fraction of re-cooling events with respect to the expected collisions for different numbers of ions confined under the same trapping conditions. The results are shown in Figure 5.9. Interestingly, odd ion numbers seem to lead to a slightly higher fraction of re-cooling events. For five or more ions, at least 78% of collision events lead to re-cooling. This reduces the fractional systematic uncertainty associated with undetected phase shifts from collision events to 0.9×10^{-19}.

5.3.5 Second-order Zeeman shifts

At our current operating conditions, the oscillating magnetic field from the trap drive (c.f. subsection 4.6.3) contributes the largest second-order Zeeman shift. For $^{88}Sr^{+}$, there is no dependence of this shift on the direction of the quantization axis due to our averaging scheme canceling the tensor term. With the average second-order Zeeman sensitivity of $3.122\,\mu Hz/\mu T^2$ [194], we obtain a frequency shift of $122(2)\,\mu Hz$, or $2.74(5) \times 10^{-19}$ in fractional units, from the oscillating magnetic field.

https://doi.org/10.7795/110.20260227

The static magnetic field of about 3µT used to define the quantization axis is determined in a time-resolved fashion from the servos running on the individual Zeeman components and their respective first-order Zeeman sensitivities. The corresponding second-order Zeeman shift is then also calculated and applied in a time-resolved fashion, with an average correction of 0.63×10^{-19} and a negligible uncertainty.

Additionally, the magnetic field from the blackbody radiation of the environment, the root-mean-square value of which is given by [206]

$$B_{\mathrm{rms}} = 2.775\,\mu\mathrm{T} \left(\frac{T(\mathrm{K})}{300\,\mathrm{K}}\right)^2 , \tag{5.33}$$

has to be considered. The associated second-order Zeeman shift is influenced by the coupling of the radiation to the ${}^2D_{5/2} \leftrightarrow {}^2D_{3/2}$ fine-structure transition, and has been calculated to be -0.11×10^{-19} at room temperature in [207]. The corresponding correction is currently not applied in a time-resolved fashion. Variations of the laboratory temperature of up to ± 1 K over the course of the year yield an uncertainty below 10^{-21}.

5.3.6 AC Stark shift from clock interrogation

All laser beams except for the 674 nm clock beam are blocked by mechanical shutters during clock interrogation. Therefore, we only need to consider the Stark shift, of the form Equation 5.24, caused by the field of the interrogating laser itself.

To assess the shift on the ${}^2S_{1/2} \rightarrow {}^2D_{5/2}$ clock transition frequency, the differential scalar and tensor polarizabilities $\Delta\alpha_{S,T}(\lambda = 674\,\mathrm{nm}) = \alpha_{S,T}(D_{5/2}, \lambda = 674\,\mathrm{nm}) - \alpha_{S,T}(S_{1/2}, \lambda = 674\,\mathrm{nm})$ are relevant. The $S_{1/2}$ state has zero tensorial polarizability, and consequently only the $D_{5/2}$ state contributes to the tensor part. For the $D_{5/2}$ state, the tensorial contribution would cancel analogously to the quadrupole shift, if we interrogated all transitions with the same laser light intensity. However, this is not the case since we scale the interrogation time inversely with the first-order Zeeman sensitivity, and adjust the intensity accordingly.

We obtain the relevant diffential polarizabilities from [208] with an estimated uncertainty of 25%, yielding a convenient expression for the AC Stark shift from the interrogation laser in terms of the intensity I_0 at the position of the ion(s):

https://doi.org/10.7795/110.20260227

$$\Delta\nu_{674\,\mathrm{nm}} = I_0 \left(0.525 + 0.064\,(3\cos^2\beta - 1)\,\frac{3m_J^2 - J(J+1)}{J(2J+1)} \right) \mathrm{mHz}/(\mathrm{W/m^2})\,. \tag{5.34}$$

The intensity is obtained by measuring the laser power before and after the vacuum chamber for different intermediate powers and extrapolating to the (very small) powers used during the clock sequence. From measuring the beam diameter at two positions outside the vacuum chamber, we extract an estimated beam waist radius at the ion position of 100(10) µm. We obtain intensities of $I_0(\pm 5/2) \approx 0.031\,\mathrm{W/m^2}$ and $I_0(\pm 3/2) \approx 0.011\,\mathrm{W/m^2}$ during the interrogation pulses for the $\pm 1/2 \rightarrow \pm 5/2$ and $\pm 1/2 \rightarrow \pm 3/2$ Zeeman pairs, respectively.

In our configuration, the clock beam is aligned along the trap axis and horizontally polarized, so that typically $\beta \approx 90° - 54.7° = 35.3°$, and for some of the single-ion measurements we used $\beta \approx 90° - 61.4° = 28.6°$. We calculate the total shift for each of the two relevant Zeeman pairs, and perform a weighted average according to our determination of the center frequency (weight 5/6 for $\pm 1/2 \rightarrow \pm 3/2$ and 1/6 for $\pm 1/2 \rightarrow \pm 5/2$). We obtain a fractional frequency shift of about 0.17×10^{-19} for $\beta = 35.3°$ and 0.18×10^{-19} for $\beta = 28.6°$, each with an estimated uncertainty of 30%, meaning the difference between the two cases is negligible.

5.3.7 Servo error

Systematic frequency offsets can arise if the clock servo fails to predict the correct center frequency for the subsequent interrogation cycle. For example, a linear drift between the atomic transition and the interrogation laser leads to a constant offset in a single-integrating servo [39].

The clock laser we use for interrogation inherits its instability from the $^{171}Yb^{+}$ single-ion clock whenever it is operating on the E3 transition, and otherwise from the ultrastable silicon cavity [65] at PTB (c.f Figure 5.10). During operation of the $^{171}Yb^{+}$ clock, there is no drift of the laser frequency, and consequently no corresponding servo errors. For other time intervals, the effects of a small residual drift of the silicon cavity have to be corrected for.

As we do not observe any variation of tensor shifts during measurement runs, magnetic field variations are the leading remaining possible cause of servo errors. This

https://doi.org/10.7795/110.20260227

error would lead to an imperfect cancellation of the first order Zeeman shift in the center frequency resulting from all servos. The effect is suppressed at multiple levels: Firstly, each Zeeman component is interrogated in a $[-\Delta\nu, +\Delta\nu, +\Delta\nu, -\Delta\nu]$ pattern, instead of e.g. always interrogating the left side of the line before the right [209]. Secondly, the order of interrogating the different Zeeman components during one clock cycle yields a further non-trivial suppression.

We simulate the effect a linear magnetic field drift has on our specific servo sequence, including the employed interrogation times, order of interrogation, as well as the dead time, and find a fractional frequency offset of about $1.0\times10^{-5}/[(\Delta B/\Delta t)(\mathrm{T/s})]$, depending on the drift rate $\Delta B/\Delta t$. Experimentally, we typically do not observe a long-term drift of the magnetic field, but rather noise that shows are more complex behavior (c.f. Figure 4.12). To estimate the overall effect of the observed noise, we numerically calculate the first derivative of the observed magnetic field on 200 s time steps and integrate the accumulated error over the time steps for a selection of typical measurement runs. We obtain fractional frequency shifts below 0.1×10^{-19}. Additional offsets due to nonlinearities on these timescales are expected to be even smaller. A more extensive treatment of servo errors resulting from noise with a zero mean can be found in [210].

One effect that would not be included in our treatment are cycle-synchronous magnetic field changes. However, since we do not switch the magnitude or direction of the applied static field during the clock sequence, and also do not employ any mechanically changing components in the vicinity of the ions, we do not see a possible source of this effect.

As an additional cross-check, we search for imbalances of the overall collective excitation probability on the left and right sides of the resonance in our data, which would correspond to a frequency shift of the atomic transition frequency with respect to the frequency realized by the servo sequence (c.f. subsection 5.2.2). We do not find statistically significant imbalances.

5.3.8 AOM phase chirp

The acousto-optic modulator (AOM) used for clock interrogation is repeatedly switched on and off during the experimental sequence. This leads to temperature changes in the AOM crystal, which in turn cause optical path length changes [211].

https://doi.org/10.7795/110.20260227

We actively stabilize the optical path length between the clock laser system and a point about 15 cm from the vacuum chamber based on interferometry with the retroreflected 0th diffraction order of the AOM used for clock interrogation. The bandwidth of this stabilization is about 10 kHz, and consequently any AOM phase chirp that is common mode to both diffraction orders will be suppressed by a factor of about 1000 for an integrating servo.

At full power, the observed phase error due to AOM chirp in [211] is 9 mrad for an "off" time of 2 ms. This means that for typical "off" times of 40 ms in our experiment, and with a similar duty cycle, we expect 180 mrad at full power, corresponding to a fractional frequency offset of 6×10^{-16}. We use the AOM at more than 40 dB below full diffraction efficiency, corresponding to a factor 10 000 in power. Linear scaling yields an estimated fractional shift below 6×10^{-20}, even without considering the additional suppression from the fiber length stabilization.

https://doi.org/10.7795/110.20260227

5.3.9 Uncertainty budget

The considerations detailed above are summarized in the preliminary uncertainty budget Table 5.1 for clock operations with eight to ten ions. We obtain a systematic uncertainty of 5.3×10^{-19}. This value is slightly below the lowest systematic uncertainty published to date, 5.5×10^{-19}, of the aluminum ion clock at NIST [23]. Recently, an even lower value of 4.6×10^{-19} has been reported for a clock based on a single calcium ion that is trapped in a liquid nitrogen cryogenic environment [24].

Effect	shift (10^{-19})	uncertainty (10^{-19})
Blackbody radiation[1]	5379.1	4.4
Thermal ion motion	−12.4	2.6
Excess micromotion	−0.3	0.9
Collisions	0	0.9
Servo error (Residual 1st order Zeeman)	0	0.1
2nd-order Zeeman (static B-field)[2]	0.6	<0.1
2nd-order Zeeman (BBR)	−0.1	<0.1
2nd-order Zeeman (trap drive)	2.7	<0.1
AC Stark (674 nm)	0.2	<0.1
Residual shift inhomogeneity	0	<0.1
Total	5369.8	5.3

Table 5.1: Preliminary uncertainty budget for the $^{88}Sr^{+}$ clock operating with eight to ten ions. Single-ion operation yields a higher systematic uncertainty of 6.5×10^{-19} due to a 3.9×10^{-19} uncertainty of the collisional shift.
[1]Time-resolved correction based on resistive temperature sensors. Value given is for a typical temperature of 296.75 K.
[2]Time-resolved correction based on servo results. Value given is for a typical magnetic field strength of 3.0 µT.

https://doi.org/10.7795/110.20260227

5.4 Comparison with $^{171}Yb^{+}$ single-ion clock

We compare the new optical clock based on $^{88}Sr^{+}$ to the established single-ion clock (c.f. chapter 2) based on the E3 transition in $^{171}Yb^{+}$. As a reminder, the latter clock has previously been evaluated with a fractional systematic uncertainty of 2.7×10^{-18} [63] and has demonstrated a fractional instability of $1.0 \times 10^{-15}/\sqrt{\tau(\mathrm{s})}$ [63, 68].

Key components involved in this optical frequency comparison are depicted in Figure 5.10. Similar to measurements of the E3/E2 frequency ratio (c.f. section 2.3), the Sr^{+} probe laser frequency is stabilized with fixed ratio R_0 to that of the E3 probe laser at a frequency comb. The servo running on the E3 transition steers the probe laser directly, while the servo of the Sr^{+} clock steers a local offset Δf_2 via an AOM close to the ion trap, which is recorded and can be used to calculate the frequency ratio via

$$\frac{\nu_{\mathrm{Sr}^+}}{\nu_{\mathrm{E3}}} = R_0 \left(1 - \frac{\Delta f_2}{\nu_{\mathrm{Sr}^+}} - \frac{\Delta\nu_{\mathrm{Sr}^+}}{\nu_{\mathrm{Sr}^+}} + \frac{\Delta\nu_{\mathrm{E3}}}{\nu_{\mathrm{E3}}}\right) , \tag{5.35}$$

where the frequency offsets $\Delta\nu_{\mathrm{E3}}$ and $\Delta\nu_{\mathrm{Sr}^+}$ can be obtained from the respective uncertainty budgets. For the $^{88}Sr^{+}$ clock, time-resolved corrections for the BBR shift and second-order Zeeman shift were applied as discussed in section 5.3, so that $\Delta\nu_{\mathrm{Sr}^+}$ and Δf_2 are both time-dependent.

The resulting data, including measurements taken with a single, and eight to ten $^{88}Sr^{+}$ ions, is shown in Figure 5.11. The fractional statistical uncertainty from all data is 9.1×10^{-19}, and we find a reduced Chi square of 1.1, compatible with white frequency noise. This demonstrates a long-term stability, or reproducibility, of the $^{171}Yb^{+}$ clock well below its systematic uncertainty. The frequency ratio $\nu_{\mathrm{Sr}^+}/\nu_{\mathrm{E3}}$ of the two transitions is found to be

$$0.692671163215966039(20)\,,$$

where a gravitational redshift of $-2.620(31) \times 10^{-17}$ between the two clocks has been taken into account. With an overall fractional uncertainty of 2.9×10^{-18} this is the most accurate determination of any frequency ratio involving different atomic transitions to date. Lower uncertainties have only been reported for differential measurements involving multiple samples of the same atomic species in the same apparatus [19, 212–214].

https://doi.org/10.7795/110.20260227

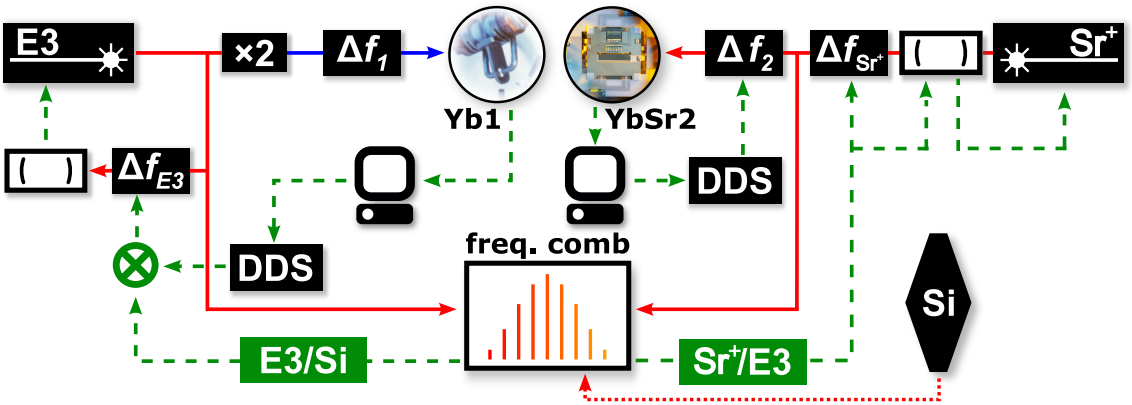

Figure 5.10: Key components in the measurement of ν_{Sr^+}/ν_{E3}. Yb1 refers to the single-ion clock introduced in chapter 2, while YbSr2 refers to the new apparatus described in chapter 4. Optical paths are depicted by red and blue lines; electric signals by dashed green lines. The E3 and Sr^+ clock lasers are stabilized to optical cavities, and the E3 laser light is frequency doubled before being sent to the ion trap. The short-term stability of an ultrastable silicon cavity (Si) [65] is transferred via a frequency comb to the E3 clock laser [66]. The Sr^+ laser frequency is controlled to provide a constant frequency ratio relative to the E3 laser at the a frequency comb via the frequency offset Δf_{Sr^+} and the cavity length, thereby inheriting the Si short term stability from the E3 laser. Spectroscopy of the E3 clock transition steers the corresponding laser frequency via direct digital synthesis (DDS) generating the frequency offset Δf_{E3}, while the frequency of the Sr^+ laser is corrected by an additional offset to Δf_2 directly before the ion trap.

https://doi.org/10.7795/110.20260227

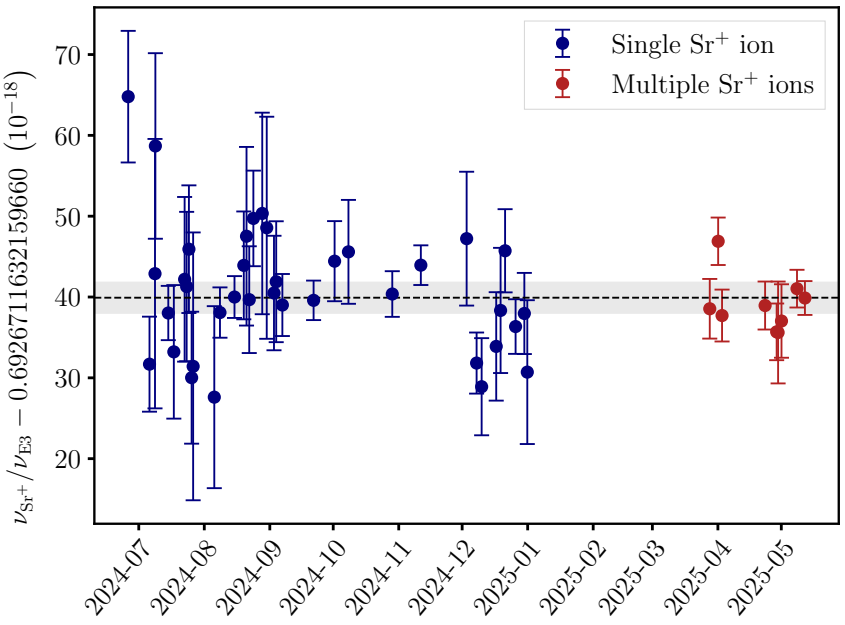

Figure 5.11: Measurements of the ratio between the frequencies ν_{Sr^+} of the $^2S_{1/2} \rightarrow {}^2D_{5/2}$ transition in $^{88}Sr^+$ and ν_{E3} of the $^2S_{1/2} \rightarrow {}^2F_{7/2}$ transition in $^{171}Yb^+$. Data points shown in blue were obtained with a single $^{88}Sr^+$ ion, while data points shown in red correspond to measurements with eight to ten $^{88}Sr^+$ ions. Error bars correspond to the statistical uncertainties of the individual measurements, obtained from extrapolating a fit to the Allan deviation to the measurement time. We find $\chi^2_{red} \approx 1.1$ and an overall statistical uncertainty of 0.9×10^{-18}. The dashed line corresponds to the weighted average of all measurements and the grey shaded area depicts the combined systematic uncertainty of 2.8×10^{-18}.

This measurement constitutes a significant step towards a future redefinition of the SI unit second, since it is only the second frequency ratio measured between different atomic transitions that fulfills the criterion of an overall fractional uncertainty at or below 5×10^{-18} [35]. The first frequency ratio to fulfill this criterion, with an overall uncertainty of 4.4×10^{-18}, was that measured between the same $^{171}Yb^+$ single-ion clock running on the E3 transition, and the $^{115}In^+$ Coulomb crystal clock at PTB [21].

Our result is compatible at the 1σ-level with that previously obtained in our group [43], when accounting for the different value of the dyamical polarizability that was used in the correction of the BBR shift, and reduces the uncertainty of ν_{Sr^+}/ν_{E3} by almost an order of magnitude.

The instability of these measurements, as characterized by the Allan deviation, is shown in Figure 5.12. With a single $^{88}Sr^+$ ion, we find a measurement instability

https://doi.org/10.7795/110.20260227

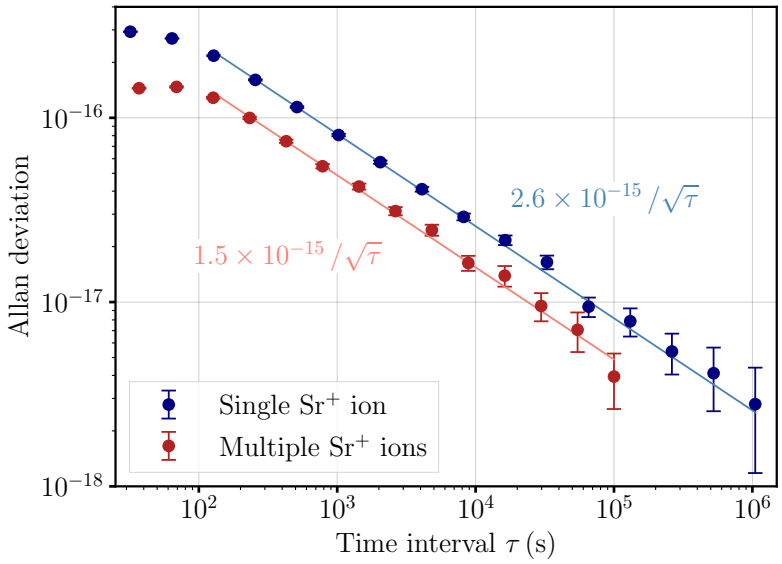

Figure 5.12: Measurement instability of the frequency ratio ν_{Sr^+}/ν_{Yb^+} as characterized by the Allan deviation for operation of the $^{88}Sr^+$ clock with a single ion (shown in blue) and eight to ten ions (shown in red). The solid lines depict fits according to the $1/\sqrt{\tau}$ scaling for white frequency noise.

of $2.6 \times 10^{-15}/\sqrt{\tau(s)}$ for an averaging time τ, indicating an instability of $2.4 \times 10^{-15}/\sqrt{\tau(s)}$ of the $^{88}Sr^+$ clock. For N ions, one would expect a reduction of the clock's instability by a factor of $1/\sqrt{N}$. While all ions contribute to the clock signal with the same excitation probabilities, we find that the dead time associated with frequent re-cooling after crystal melting limits the instability of the $^{88}Sr^+$ clock operating with eight to ten ions to about $1.1 \times 10^{-15}/\sqrt{\tau(s)}$. While this is not the ideal improvement by $\sqrt{N}$, it still reduces the measurement time by more than a factor of four compared to single-ion operation. Currently, re-cooling of the crystal takes about 4 s, and the instability could be improved further by making this process more efficient. Lower collision rates in a cryogenic environment would also contribute to an improved instability.

https://doi.org/10.7795/110.20260227

https://doi.org/10.7795/110.20260227

6 Conclusion and Outlook

This thesis has reported on optical frequency comparisons and their application to probing variations of fundamental constants. Key experimental results in chapter 2 and chapter 3 were based on data obtained with an existing optical clock setup based on a single $^{171}Yb^{+}$ ion. Interleaved interrogation of both an electric octupole (E3) transition and an electric quadrupole (E2) transition enables a high level of experimental robustness in realizing the frequency ratio ν_{E3}/ν_{E2}, which is highly sensitive to variations of the fine-structure constant. The long-term reproducibility of this measurement was demonstrated to be at the low-10^{-18} level. Including the resulting data with that previously obtained in our group improved the best constraints on a linear drift of the fine-structure constant α to $(1/\alpha)(\mathrm{d}\alpha/\mathrm{d}t) = 1.8(2.5) \times 10^{-19}/\mathrm{yr}$ and its coupling to the gravitational potential Φ of the sun to $(c^2/\alpha)(\mathrm{d}\alpha/\mathrm{d}\Phi) = -2.4(3.0) \times 10^{-9}$, reducing uncertainties by about a factor of four.

Frequency comparisons for the search of new physics are an ongoing long-term project. Specifically the analysis of a frequency ratio with respect to slow temporal changes of fundamental constants improves as the time spanned by individual measurements increases. The measurement data of the E3/E2 frequency ratio presented in chapter 2 ends in November 2022. In the almost three years since, measurements have continued with further improved experimental availability. Evaluation of the data is ongoing, and is expected to offer a further improved reach compared to the results presented in this thesis.

In chapter 3 the ν_{E3}/ν_{E2} measurement data, along with that from a comparison between the $^{171}Yb^{+}$ E3 clock and a Sr lattice clock, was analysed for oscillations in the context of a broadband search for signatures of ultralight dark matter (UDM). By searching for oscillations of fundamental constants, we investigated small, hypothetical couplings between ultralight dark matter and standard model matter. Leveraging the high α-sensitivity of both measured frequency ratios, more than an

https://doi.org/10.7795/110.20260227

order-of-magnitude improvement in limits on a scalar UDM coupling to photons was obtained over a wide range of dark matter masses.

Two additional aspects of searching for ultralight dark matter were investigated: First, UDM couplings to the nuclear sector, which are commonly probed using clocks based on hyperfine transitions, were investigated with optical clocks for the first time. This was done by considering the influence that small oscillations of the nuclear charge radius would have on the E3/E2 frequency ratio. Second, comparisons between space- and time-separated oscillators were analysed. It was shown that this approach preserves sensitivity to dark matter even for the case of identical sensitivities to fundamental constants, and also offers access to complementary dark matter signatures and couplings.

A new optical clock apparatus, aimed at mid-10^{-19}-level systematic uncertainties and robust clock operation for improved tests of fundamental physics, was developed and constructed in the scope of this thesis. Key elements of this dual-species experimental apparatus, designed for use with $^{88}Sr^{+}$ and $^{171}Yb^{+}$ ions, were presented in chapter 4. Initial characterizations, relevant for the discussion of $^{88}Sr^{+}$ clock frequency shifts in chapter 5, were carried out. Low heating rates of trapped $^{88}Sr^{+}$ ions suggest the potential for long coherent interrogation on the $^{171}Yb^{+}$ E3 transition, with projected frequency instabilities at the low $10^{-16}/\sqrt{\tau}$-level. Micromotion effects, which are suppressed for $^{88}Sr^{+}$, require careful monitoring for $^{171}Yb^{+}$ but remain compatible with low-10^{-19} uncertainties. Time-resolved monitoring of the system's temperature with calibrated resistive temperature sensors, combined with existing modeling, enables a precise characterization of the ions' thermal environment. Overall, the apparatus supports the prospect of improved $^{171}Yb^{+}$ clocks and highly stable $^{171}Yb^{+}/^{88}Sr^{+}$ frequency ratio measurements.

Chapter 5 has presented an optical clock based on the $^{2}S_{1/2} \rightarrow {}^{2}D_{5/2}$ transition in $^{88}Sr^{+}$, realized with the experimental apparatus introduced in chapter 4. To overcome the limited instability of the clock based on a single $^{88}Sr^{+}$ ion, robust clock operation with linear Coulomb crystals of eight to ten ions was implemented. Effects related to multi-ion clock operation, such as the coupled ion motion, were analysed. A technique for obtaining ion-resolved information on frequency shifts even in the case of global interrogation with a single laser beam was introduced, and applied to analyse the variation of electric field gradients and the magnetic field strength along the ion chain.

https://doi.org/10.7795/110.20260227

Systematic effects relevant to both operation with a single and multiple ions were analysed, and we obtained a fractional systematic uncertainty of 5.3×10^{-19} for the clock operating with eight to ten ions, and 6.5×10^{-19} for a single ion. The difference is due to the fact that melting of the Coulomb crystal reduces the number of undetected background gas collisions.

We compared the new optical clock with the single-ion $^{171}Yb^+$ clock operating on the $^2S_{1/2}(F = 0) \rightarrow {}^2F_{7/2}(F = 3)$ E3 transition and obtained an unperturbed frequency ratio of $\nu_{Sr^+}/\nu_{E3} = 0.692671163215966039(20)$. The combined fractional uncertainty of 2.9×10^{-18} is the lowest reported on any frequency comparison involving different atomic transitions to date. Measurement results obtained with a single $^{88}Sr^+$ ion are compatible with those obtained with eight to ten ions, and multi-ion operation leads to a significantly improved measurement instability.

The measurement of this frequency ratio, particularly when performed with multiple $^{88}Sr^+$ ions, overcomes some of the limitations of those used in searches for ultralight dark matter in chapter 3: Its instability is lower by a factor of about 6.7 than that obtained in the measurement of ν_{E3}/ν_{E2}. Additionally, the measurement already demonstrates an exceptional long-term stability without the excess noise observed in the comparison with the Sr lattice clock.

These improvements become apparent in the exclusion plot Figure 6.1. The same data evaluation explained in detail in section 3.3 was applied to the multi-ion measurement data of ν_{Sr^+}/ν_{E3} shown in Figure 5.11. In the absence of statistically significant oscillations, and using the α-sensitivity of 6.38 [27], we obtain limits on the scalar UDM coupling d_e. Even though only 1.0×10^6 s (11 days) of data are analysed, the limits are already slightly tighter than those obtained from evaluating 20×10^6 s (235 days) of ν_{E3}/ν_{E2} data over most of the investigated mass range, due to the improved measurement instability. The projection shows the expected reach if the larger amount of data (20×10^6 s) was available for the frequency ratio ν_{Sr^+}/ν_{E3}, obtained with an instability of $1 \times 10^{-15}/\sqrt{\tau(\mathrm{s})}$.

Currently, the $^{88}Sr^+$ multi-ion clock and the $^{171}Yb^+$ single-ion clock contribute about equally to the measurement instability of ν_{Sr^+}/ν_{E3}. Realizing a clock based on the $^{171}Yb^+$ E3 transition within the same apparatus as the $^{88}Sr^+$ clock, for example in a separate trap segment, will offer further improvements. The $^{171}Yb^+$ clock is expected to become more stable than the current single-ion clock for two reasons: The small heating rate will enable increased coherent interrogation times on the E3 transition, and scaling to multiple ions is possible in the linear trap. The frequency

https://doi.org/10.7795/110.20260227

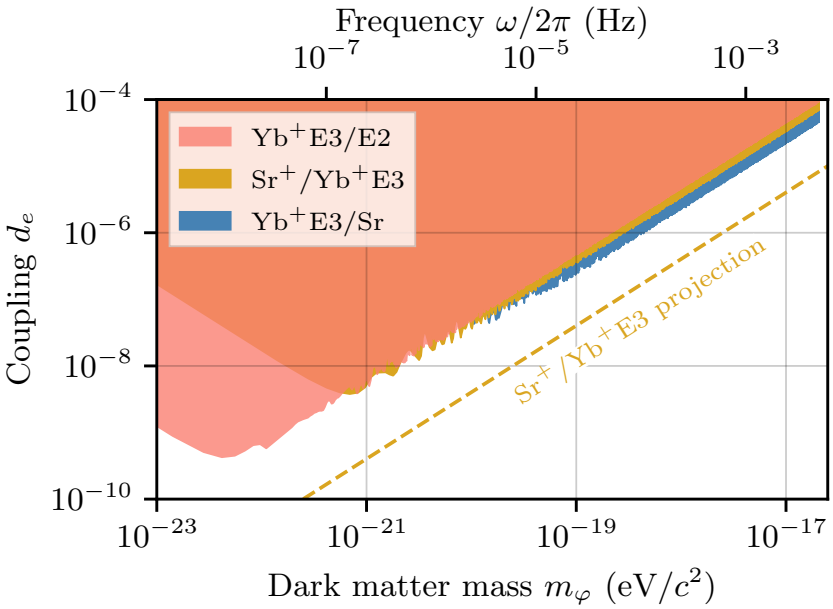

Figure 6.1: Comparison of limits on the scalar UDM coupling d_e, obtained from measurements of the frequency ratio ν_{E3}/ν_{E2} (235 days of data), the frequency ratio ν_{E3}/ν_{Sr} (14 days of data), and the frequency ratio ν_{Sr^+}/ν_{E3} (11 days of data, obtained with 8 to 10 $^{88}Sr^+$ ions). The dashed line indicates the expected reach for 235 days of ν_{Sr^+}/ν_{E3} measurement data with a $1.0 \times 10^{-15}/\sqrt{\tau(s)}$ instability.

ratio realized in this fashion will then not only offer common-mode suppression of certain external perturbations such as temperature fluctuations, but also feature an instability at or below the $1 \times 10^{-15}/\sqrt{\tau(s)}$ level, limited by the $^{88}Sr^+$ multi-ion clock. The achieved and expected experimental progress thus makes it plausible for the frequency ratio ν_{Sr^+}/ν_{E3} to yield the best searches for variations of the fine-structure constant within the near future. In this context, the investigation of fast variations with dynamical decoupling techniques [109, 167, 215] seems particularly promising.

Of course the results in this work represent only one contribution to the rapidly evolving field of high-precision frequency comparisons and their application to searches for variations of fundamental constants. Significant advances are reported across a wide range of systems, such as highly-charged ions, neutral atoms in optical lattices or tweezers, and the thorium nuclear transition. As the performance of optical clocks is improved, and new platforms with enhanced sensitivities to variations of fundamental constants are developed, these systems will continue providing significant contributions to tests of fundamental physics.

https://doi.org/10.7795/110.20260227

References

[1] S. Weinberg, H. B. Nielsen, and J. G. Taylor. "Overview of Theoretical Prospects for Understanding the Values of Fundamental Constants [and Discussion]". In: *Philosophical Transactions of the Royal Society of London. Series A, Mathematical and Physical Sciences* 310.1512 (1983), pp. 249–252 (cit. on p. 1).

[2] J. Uzan. "The stability of fundamental constants". In: *Comptes Rendus Phys.* 16.5 (2015), pp. 576–585. DOI: 10.1016/j.crhy.2015.03.007 (cit. on p. 1).

[3] J. Uzan. "Varying constants, gravitation and cosmology". In: *Living Rev. Relativ.* 14.2 (2011). DOI: 10.12942/lrr-2011-2 (cit. on p. 1).

[4] G. Aad et al. "Observation of a new particle in the search for the Standard Model Higgs boson with the ATLAS detector at the LHC". In: *Physics Letters B* 716.1 (2012), pp. 1–29. DOI: https://doi.org/10.1016/j.physletb.2012.08.020 (cit. on p. 2).

[5] S. Chatrchyan et al. "Observation of a new boson at a mass of 125 GeV with the CMS experiment at the LHC". In: *Physics Letters B* 716.1 (2012), pp. 30–61. DOI: https://doi.org/10.1016/j.physletb.2012.08.021 (cit. on p. 2).

[6] B. P. Abbott et al. "Observation of Gravitational Waves from a Binary Black Hole Merger". In: *Phys. Rev. Lett.* 116 (061102 Feb. 2016). DOI: 10.1103/PhysRevLett.116.061102 (cit. on p. 2).

[7] P. Touboul et al. "MICROSCOPE Mission: First Results of a Space Test of the Equivalence Principle". In: *Phys. Rev. Lett.* 119.231101 (2017). DOI: 10.1103/PhysRevLett.119.231101 (cit. on pp. 2, 51).

[8] S. Fray, C. A. Diez, T. W. Hänsch, and M. Weitz. "Atomic interferometer with amplitude gratings of light and its applications to atom based tests of the equivalence principle". In: *Phys. Rev. Lett.* 93.240404 (2004). DOI: 10.1103/PhysRevLett.93.240404 (cit. on p. 2).

https://doi.org/10.7795/110.20260227

[9] T. Damour and J. F. Donoghue. "Equivalence principle violations and couplings of a light dilaton". In: *Phys. Rev. D* 82.084033 (2010). DOI: 10.1103/PhysRevD.82.084033 (cit. on pp. 2, 24, 26, 47).

[10] A. Derevianko and M. Pospelov. "Hunting for topological dark matter with atomic clocks". In: *Nat. Phys.* 10.12 (2014), pp. 933–936. DOI: 10.1038/nphys3137 (cit. on pp. 2, 51).

[11] M. Fierz. "Über die physikalische Deutung der erweiterten Gravitationstheorie P. Jordans". In: *Helv. Phys. Acta* 29.II (1956) (cit. on p. 2).

[12] J. Uzan. "The fundamental constants and their variation: Observational and theoretical status". In: *Rev. Mod. Phys.* 75.2 (2003), pp. 403–455. DOI: 10.1103/RevModPhys.75.403 (cit. on p. 2).

[13] E. Peik. "Fundamental constants and units and the search for temporal variations". In: *Nucl. Phys. B - Proc. Suppl.* 203-204 (2010), pp. 18–32. DOI: 10.1016/j.nuclphysbps.2010.08.003 (cit. on p. 2).

[14] J. C. Berengut and V. V. Flambaum. "Astronomical and Laboratory searches for space-time variation of fundamental constants". In: *J. Phys. Conf. Ser.* 264.1 (2011). DOI: 10.1088/1742-6596/264/1/012010 (cit. on p. 2).

[15] M. S. Safronova, D. Budker, D. Demille, Derek F.Jackson Kimball, A. Derevianko, and Charles W. Clark. "Search for new physics with atoms and molecules". In: *Rev. Mod. Phys.* 90.2 (2018), p. 25008. DOI: 10.1103/RevModPhys.90.025008 (cit. on p. 2).

[16] M. S. Safronova. "The Search for Variation of Fundamental Constants with Clocks". In: *Ann. Phys.* 531.1800364 (2019). DOI: 10.1002/andp.201800364 (cit. on p. 2).

[17] A. Aeppli, K. Kim, W. Warfield, M. S. Safronova, and J. Ye. "A clock with 8×10^{-19} systematic uncertainty". In: *Phys. Rev. Lett.* 133.023401 (2024) (cit. on p. 2).

[18] S. M. Brewer, J. S. Chen, A. M. Hankin, E. R. Clements, C. W. Chou, D. J. Wineland, D. B. Hume, and D. R. Leibrandt. "$^{27}Al^{+}$ Quantum-Logic Clock with a Systematic Uncertainty below 10^{-18}". In: *Phys. Rev. Lett.* 123.33201 (2019). DOI: 10.1103/PhysRevLett.123.033201 (cit. on p. 2).

[19] W. F. McGrew et al. "Atomic clock performance enabling geodesy below the centimetre level". In: *Nature* 564 (2018), pp. 87–90. DOI: 10.1038/s41586-018-0738-2 (cit. on pp. 2, 118).

https://doi.org/10.7795/110.20260227

[20] A. Tofful et al. "$^{171}Yb^{+}$ optical clock with 2.2×10^{-18} systematic uncertainty and absolute frequency measurements". In: *Metrologia* 61.045001 (2024). DOI: 10.1088/1681-7575/ad53cd (cit. on p. 2).

[21] H. N. Hausser et al. "$^{115}In^{+}$ - $^{172}Yb^{+}$ Coulomb Crystal Clock with 2.5×10^{-18} Systematic Uncertainty". In: *Phys. Rev. Lett.* 134.23201 (2025). DOI: 10.1103/PhysRevLett.134.023201 (cit. on pp. 2, 13, 36, 87, 120).

[22] N. Huntemann, C. Sanner, B. Lipphardt, Chr. Tamm, and E. Peik. "Single-Ion Atomic Clock with 3×10^{-18} Systematic Uncertainty". In: *Phys. Rev. Lett.* 116.063001 (2016). DOI: 10.1103/PhysRevLett.116.063001 (cit. on pp. 2, 13, 57).

[23] M. C. Marshall et al. "High-Stability Single-Ion Clock with 5.5×10^{-19} Systematic Uncertainty". In: *Phys. Rev. Lett.* 135.33201 (2025). DOI: 10.1103/hb3c-dk28 (cit. on pp. 2, 117).

[24] B. Zhang et al. *A Liquid-Nitrogen-Cooled $^{40}Ca^{+}$ Ion Optical Clock with a Systematic Uncertainty of* 4.6×10^{-19}. 2025. arXiv: 2506.17423 (cit. on pp. 2, 117).

[25] J.D. Prestage, R.L. Tjoelker, and L. Maleki. "Atomic Clocks and Variations of the Fine Structure Constant". In: *Phys. Rev. Lett.* 74.18 (1995), pp. 3511–3514. DOI: 10.4324/9780429349812-27 (cit. on p. 3).

[26] V. A. Dzuba, V. V. Flambaum, and J. K. Webb. "Space-time variation of physical constants and relativistic corrections in atoms". In: *Phys. Rev. Lett.* 82.5 (1999), pp. 888–891. DOI: 10.1103/PhysRevLett.82.888 (cit. on p. 3).

[27] V. V. Flambaum and V. A. Dzuba. "Search for variation of the fundamental constants in atomic, molecular, and nuclear spectra". In: *Can. J. Phys.* 87.1 (2009), pp. 25–33. DOI: 10.1139/p08-072 (cit. on pp. 3, 11, 12, 30, 35, 58, 125).

[28] T. Fortier and E. Baumann. "20 Years of Developments in Optical Frequency Comb Technology and Applications". In: *Commun. Phys.* 2.153 (2019), pp. 1–16. DOI: 10.1038/s42005-019-0249-y (cit. on p. 4).

[29] S. A. Diddams, K. Vahala, and T. Udem. "Optical frequency combs: Coherently uniting the electromagnetic spectrum". In: *Science* 369.6501 (2020), eaay3676. DOI: 10.1126/science.aay3676 (cit. on p. 4).

https://doi.org/10.7795/110.20260227

[30] R. Lange. "High-Precision Frequency Comparisons and Searches for New Physics with Yb^+ Optical Clocks". PhD Thesis. Universität Hannover, 2021 (cit. on pp. 4, 11, 57).

[31] A. D. Ludlow, M. M. Boyd, J. Ye, E. Peik, and P. O. Schmidt. "Optical atomic clocks". In: *Rev. Mod. Phys.* 87.2 (2015), pp. 637–701. DOI: 10.1103/RevModPhys.87.637 (cit. on p. 5).

[32] S. Weyers, V. Gerginov, M. Kazda, J. Rahm, B. Lipphardt, G. Dobrev, and K. Gibble. "Advances in the accuracy, stability, and reliability of the PTB primary fountain clocks". In: *Metrologia* 55.6 (2018). DOI: 10.1088/1681-7575/aae008 (cit. on p. 5).

[33] S. Beattie, B. Jian, C. Marceau, K. Gibble, and M. Gertsvolf. "Advancements in the NRC-FCs2 primary frequency standards". In: *Metrologia* 62.035003 (2025). DOI: 10.1088/1681-7575/adcd7b (cit. on p. 5).

[34] C. Marceau, S. Beattie, K. Kato, B. Jian, M. Gertsvolf, and P. Dubé. "Absolute frequency measurement of a $^{88}Sr^+$ clock by direct comparison to a primary frequency standard". In: *Metrologia* 62.045001 (2025). DOI: 10.1088/1681-7575/ade4d1 (cit. on p. 5).

[35] N. Dimarcq et al. "Roadmap towards the redefinition of the second". In: *Metrologia* 61.012001 (2024). DOI: 10.1088/1681-7575/ad17d2 (cit. on pp. 5, 120).

[36] D.W. Allan. "Statistics of Atomic Frequency Standards". In: *Proc. IEEE* 54.2 (1966), pp. 431–453. DOI: 10.1109/PROC.1966.4634 (cit. on p. 5).

[37] D. J. Wineland, C. Monroe, W. M. Itano, D. Leibfried, B. E. King, and D. M. Meekhof. "Experimental Issues in Coherent Quantum-State Manipulation of Trapped Atomic Ions". In: *J. Res. Natl. Inst. Stand. Technol.* 103.3 (1998), pp. 259–328. DOI: 10.6028/jres.103.019 (cit. on pp. 6, 92).

[38] D. Leibfried, R. Blatt, C. Monroe, and D. Wineland. "Quantum dynamics of single trapped ions". In: *Rev. Mod. Phys.* 75.1 (2003), pp. 281–324. DOI: 10.1103/RevModPhys.75.281 (cit. on p. 6).

[39] E. Peik, T. Schneider, and Chr. Tamm. "Laser frequency stabilization to a single ion". In: *J. Phys. B At. Mol. Opt. Phys.* 39.1 (2006), pp. 145–158. DOI: 10.1088/0953-4075/39/1/012 (cit. on pp. 6, 114).

[40] M. Filzinger, S. Dörscher, R. Lange, J. Klose, M. Steinel, E. Benkler, E. Peik, C. Lisdat, and N. Huntemann. "Improved Limits on the Coupling of Ultralight Bosonic Dark Matter to Photons from Optical Atomic Clock Comparisons". In: *Phys. Rev. Lett.* 130.253001 (2023). DOI: 10.1103/PhysRevLett.130.253001 (cit. on pp. 7, 50, 52).

[41] A. Banerjee, Gi. Perez, M. Safronova, I. Savoray, and A. Shalit. "The phenomenology of quadratically coupled ultra light dark matter". In: *J. High Energy Phys.* 10 (2023), p. 042. DOI: 10.1007/JHEP10(2023)042 (cit. on pp. 7, 29).

[42] M. Filzinger, A. R. Caddell, D. Jani, M. Steinel, L. Giani, N. Huntemann, and B. M. Roberts. "Ultralight Dark Matter Search with Space-Time Separated Atomic Clocks and Cavities". In: *Phys. Rev. Lett.* 134.031001 (2025). DOI: 10.1103/PhysRevLett.134.031001 (cit. on p. 8).

[43] M. Steinel, H. Shao, M. Filzinger, B. Lipphardt, M. Brinkmann, A. Didier, T. E. Mehlstäubler, T. Lindvall, E. Peik, and N. Huntemann. "Evaluation of a $^{88}Sr^{+}$ Optical Clock with a Direct Measurement of the Blackbody Radiation Shift and Determination of the Clock Frequency". In: *Phys. Rev. Lett.* 131.8 (2023), p. 83002. DOI: 10.1103/PhysRevLett.131.083002 (cit. on pp. 8, 59, 87, 88, 90, 105, 120).

[44] R. Blatt, H. Schnatz, and G. Werth. "Ultrahigh-Resolution Microwave Spectroscopy on Trapped $^{171}Yb^{+}$ Ions". In: *Phys. Rev. Lett.* 48.23 (1982), pp. 1601–1603. DOI: 10.1103/PhysRevLett.48.1601 (cit. on p. 9).

[45] Chr. Tamm, D. Schnier, and A. Bauch. "Radio-frequency laser double-resonance spectroscopy of trapped ^{171}Yb ions and determination of line shifts of the ground-state hyperfine resonance". In: *Appl. Phys. B Laser Opt.* 60.1 (1995), pp. 19–29. DOI: 10.1007/BF01082068 (cit. on p. 9).

[46] P. T.H. Fisk. "Trapped-ion and trapped-atom microwave frequency standards". In: *Reports Prog. Phys.* 60.8 (1997), pp. 761–817. DOI: 10.1088/0034-4885/60/8/001 (cit. on p. 9).

[47] A. S. Bell, P. Gill, H. A. Klein, A. P. Levick, Chr Tamm, and D. Schnier. "Laser cooling of trapped ytterbium ions using a four-level optical-excitation scheme". In: *Phys. Rev. A* 44.1 (1991), pp. 3–6. DOI: 10.1103/PhysRevA.44.R20 (cit. on p. 9).

https://doi.org/10.7795/110.20260227

[48] M. Roberts, P. Taylor, G. P. Barwood, P. Gill, H. A. Klein, and W. R.C. Rowley. "Observation of an electric octupole transition in a single ion". In: *Phys. Rev. Lett.* 78.10 (1997), pp. 1876–1879. DOI: 10.1103/PhysRevLett.78.1876 (cit. on p. 9).

[49] D. Hayes, S. Olmschenk, D. N. Matsukevich, P. Maunz, D. L. Moehring, K. C. Younge, and C. Monroe. "Measurement of the lifetime of the $6p^2P^o_{1/2}$ level of Yb^+". In: *Phys. Rev. A* 80.022502 (2009). DOI: 10.1103/PhysRevA.80.022502 (cit. on p. 10).

[50] S. Ejtemaee, R. Thomas, and P. C. Haljan. "Optimization of Yb^+ fluorescence and hyperfine-qubit detection". In: *Phys. Rev. A* 82.6 (2010), pp. 1–18. DOI: 10.1103/PhysRevA.82.063419 (cit. on pp. 10, 73).

[51] N. Yu and L. Maleki. "Lifetime measurements of the $4f^{14}5d$ metastable states in single ytterbium ions". In: *Phys. Rev. A* 61.022507 (2000). DOI: 10.1103/PhysRevA.61.022507 (cit. on pp. 11, 13, 58).

[52] R. Lange, A. A. Peshkov, N. Huntemann, Chr. Tamm, A. Surzhykov, and E. Peik. "Lifetime of the $^2F_{7/2}$ level in Yb^+ for spontaneous emission of electric octupole radiation". In: *Phys. Rev. Lett.* 127.213001 (2021). DOI: 10.1103/physrevlett.127.213001 (cit. on p. 11).

[53] N. Huntemann, B. Lipphardt, M. Okhapkin, Chr Tamm, E. Peik, A. V. Taichenachev, and V. I. Yudin. "Generalized Ramsey excitation scheme with suppressed light shift". In: *Phys. Rev. Lett.* 109.213002 (2012) (cit. on p. 11).

[54] C. Sanner, N. Huntemann, Ri. Lange, Chr. Tamm, and E. Peik. "Autobalanced Ramsey Spectroscopy". In: *Phys. Rev. Lett.* 120.053602 (2018). DOI: 10.1103/PhysRevLett.120.053602 (cit. on p. 11).

[55] R. Lange, N. Huntemann, A. A. Peshkov, A. Surzhykov, and E. Peik. "Excitation of an Electric Octupole Transition by Twisted Light". In: *Phys. Rev. Lett.* 129.25 (2022), p. 253901. DOI: 10.1103/PhysRevLett.129.253901 (cit. on p. 11).

[56] R. Lange, N. Huntemann, C. Sanner, H. Shao, B. Lipphardt, Chr. Tamm, and E. Peik. "Coherent Suppression of Tensor Frequency Shifts through Magnetic Field Rotation". In: *Phys. Rev. Lett.* 125.143201 (2020). DOI: 10.1103/PhysRevLett.125.143201 (cit. on pp. 11, 15).

https://doi.org/10.7795/110.20260227

[57] Chr. Tamm, N. Huntemann, B. Lipphardt, V. Gerginov, N. Nemitz, M. Kazda, S. Weyers, and E. Peik. "Cs-based optical frequency measurement using cross-linked optical and microwave oscillators". In: *Phys. Rev. A* 89.023820 (2014). DOI: 10.1103/PhysRevA.89.023820 (cit. on pp. 11, 14).

[58] Z. M. Tang, Y. M. Yu, B. K. Sahoo, C. Z. Dong, Y. Yang, and Y. Zou. "Simultaneous magic trapping conditions for three additional clock transitions in Yb to search for variation of the fine-structure constant". In: *Phys. Rev. A* 107.53111 (2023). DOI: 10.1103/PhysRevA.107.053111 (cit. on pp. 12, 41, 54).

[59] M. Door et al. "Probing New Bosons and Nuclear Structure with Ytterbium Isotope Shifts". In: *Phys. Rev. Lett.* 134.63002 (2025). DOI: 10.1103/PhysRevLett.134.063002 (cit. on pp. 13, 42).

[60] A. Wilzewski et al. "Nonlinear Calcium King Plot Constrains New Bosons and Nuclear Properties". In: *Phys. Rev. Lett.* 134.233002 (2025). DOI: 10.1103/PhysRevLett.134.233002 (cit. on p. 13).

[61] L. J. Spieß et al. "Excited-State Magnetic Properties of Carbon-like Ca^{14+}". In: *Phys. Rev. Lett.* 135.4 (2025), pp. 1–7. DOI: 10.1103/p88p-brnx (cit. on p. 13).

[62] T. Lindvall et al. "Coordinated international comparisons between optical clocks connected via fiber and satellite links". In: *Optica* 12.6 (2025), p. 843. DOI: 10.1364/optica.561754 (cit. on p. 13).

[63] C. Sanner, N Huntemann, R. Lange, Chr. Tamm, E. Peik, M. S. Safronova, and S. G. Porsev. "Optical clock comparison for Lorentz symmetry testing". In: *Nature* 567.7747 (2019), pp. 204–208. DOI: 10.1038/s41586-019-0972-2 (cit. on pp. 13, 118).

[64] R. Lange, N. Huntemann, J. M. Rahm, C. Sanner, H. Shao, B. Lipphardt, Chr Tamm, S. Weyers, and E. Peik. "Improved Limits for Violations of Local Position Invariance from Atomic Clock Comparisons". In: *Phys. Rev. Lett.* 126.11102 (2021). DOI: 10.1103/PhysRevLett.126.011102 (cit. on pp. 13–15, 17, 18).

[65] D. G. Matei et al. "1.5 μm Lasers with Sub-10 mHz Linewidth". In: *Phys. Rev. Lett.* 118.263202 (2017). DOI: 10.1103/PhysRevLett.118.263202 (cit. on pp. 14, 114, 119).

https://doi.org/10.7795/110.20260227

[66] E. Benkler, B. Lipphardt, T. Puppe, R. Wilk, F. Rohde, and U. Sterr. "End-to-end topology for fiber comb based optical frequency transfer at the 10^{-21} level". In: *Opt. Express* 27.25 (2019), p. 36886. DOI: 10.1364/oe.27.036886 (cit. on pp. 14, 119).

[67] W. M. Itano. "External-Field Shifts of the ^{199} Hg^+ Optical Frequency Standard". In: *J. Res. Natl. Inst. Stand. Technol.* 105 (2000), pp. 829–837. DOI: 10.6028/jres.105.065 (cit. on pp. 14, 99, 106).

[68] S. Dörscher, N. Huntemann, R. Schwarz, R. Lange, E. Benkler, B. Lipphardt, U. Sterr, E. Peik, and C. Lisdat. "Optical frequency ratio of a $^{171}Yb^+$ single-ion clock and a ^{87}Sr lattice clock". In: *Metrologia* 58.015005 (2021). DOI: 10.1088/1681-7575/abc86f (cit. on pp. 16, 35, 118).

[69] C. M. Will. "The Confrontation Between General Relativity and Experiment". In: *Living Rev. Relativ.* 9.3 (2006). DOI: 10.1111/j.1749-6632.1980.tb15940.x (cit. on p. 16).

[70] P. Gorenstein and W. Tucker. "Astronomical signatures of dark matter". In: *Adv. High Energy Phys.* 878203 (2014). DOI: 10.1155/2014/878203 (cit. on p. 19).

[71] L. Hui, J. P. Ostriker, S. Tremaine, and E. Witten. "Ultralight scalars as cosmological dark matter". In: *Phys. Rev. D* 95.043541 (2017). DOI: 10.1103/PhysRevD.95.043541 (cit. on p. 19).

[72] D. F. J. Kimball and K. van Bibber, eds. *The Search for Ultralight Bosonic Dark Matter*. Springer, 2023. ISBN: 9783030958510. DOI: 10.1007/978-3-030-95852-7 (cit. on pp. 19, 22, 23).

[73] D. Antypas et al. *New Horizons: Scalar and Vector Ultralight Dark Matter*. 2022 (cit. on p. 19).

[74] L Badurina. "Ultralight Dark Matter Phenomenology at Atom Interferometers". PhD thesis. King's Collee London, 2023 (cit. on p. 19).

[75] J. Gué. "Exploration of new experimental strategies for the detection of ultralight dark matter: laboratory searches on ground and in space". PhD thesis. PSL Université Paris, 2024 (cit. on p. 19).

[76] V. C. Rubin and W. K. Ford Jr. "Rotation of the Andromeda Nebula from a Spectroscopic Suvey of Emission Regions". In: *Astrophys. J.* 159 (1970), pp. 379–400. DOI: 10.1086/150317 (cit. on p. 20).

[77] Y. Sofue and V. Rubin. “Rotation Curves of Spiral Galaxies”. In: *Annu. Rev. Astron. Astrophys.* 39 (2001), pp. 137–74. DOI: 10.1146/annurev.astro.39.1.137 (cit. on p. 20).

[78] M. Milgrom. “MOND - A pedagogical review”. In: *ACTA Phys. Pol. B* 32.11 (2001), pp. 3613–3627. DOI: 10.48550/arXiv.astro-ph/0112069 (cit. on p. 20).

[79] D. Clowe, M. Bradač, A.H. Gonzalez, M. Markevitch, S. W. Randall, C. Jones, and D. Zaritsky. “A Direct Empirical Proof of the Existence of Dark Matter”. In: *Astrophys. J.* 648.2 (2006), pp. L109–L113. DOI: 10.1086/508162 (cit. on p. 21).

[80] M. Bartelmann. “Gravitational lensing”. In: *Class. Quantum Gravity* 27.23 (2010). DOI: 10.1088/0264-9381/27/23/233001 (cit. on p. 20).

[81] D. Harvey, R. Massey, T. Kitching, A. Taylor, and E. Tittley. “The nongravitational interactions of dark matter in colliding galaxy clusters”. In: *Science (80-.).* 347.6229 (2015), pp. 1462–1465. DOI: 10.1126/science.1261381 (cit. on p. 21).

[82] L. Randall, J. Scholtz, and J. Unwin. “Cores in dwarf galaxies from Fermi repulsion”. In: *Mon. Not. R. Astron. Soc.* 467.2 (2017), pp. 1515–1525. DOI: 10.1093/mnras/stx161 (cit. on p. 22).

[83] T. Zimmermann, J. Alvey, D.J. E. Marsh, M. Fairbairn, and J. I. Read. “Dwarf galaxies imply dark matter is heavier than 2.2×10^{-21} eV”. In: *Phys. Rev. Lett.* 134.151001 (2024). DOI: 10.1103/PhysRevLett.134.151001 (cit. on p. 22).

[84] J. Dubinski and R.G. Carlberg. “The Structure of Cold Dark Matter Halos”. In: *Astrophys. J.* 378 (1991), pp. 496–503 (cit. on p. 22).

[85] N. Bozorgnia, F. Calore, M. Schaller, M. Lovell, G. Bertone, C. S. Frenk, R.A. Crain, J. F. Navarro, J. Schaye, and T. Theuns. “Simulated Milky Way analogues: Implications for dark matter direct searches”. In: *J. Cosmol. Astropart. Phys.* 05.024 (2016). DOI: 10.1088/1475-7516/2016/05/024 (cit. on p. 22).

[86] M. Weber and W. De Boer. “Determination of the local dark matter density in our galaxy”. In: *Astron. Astrophys.* 509.1 (2010). DOI: 10.1051/0004-6361/200913381 (cit. on p. 23).

https://doi.org/10.7795/110.20260227

[87] C. F. Martins, F. Nesti, and P. Salucci. "The local dark matter density". In: *Proc. Sci.* 161 (2012) (cit. on p. 23).

[88] J. Bovy and S. Tremaine. "On the local dark matter density". In: *Astrophys. J.* 756.1 (2012), pp. 4–9. DOI: 10.1088/0004-637X/756/1/89 (cit. on p. 23).

[89] J. I. Read. "The local dark matter density". In: *J. Phys. G Nucl. Part. Phys.* 41.6 (2014). DOI: 10.1088/0954-3899/41/6/063101 (cit. on p. 23).

[90] A. Banerjee, D. Budker, J. Eby, V. Flambaum, H. Kim, Ol. Matsedonskyi, and G. Perez. "Searching for Earth/Solar axion halos". In: *J. High Energy Phys.* 09.004 (2020). DOI: 10.1007/JHEP09(2020)004 (cit. on p. 23).

[91] A. Banerjee, D. Budker, J. Eby, H. Kim, and G. Perez. "Relaxion stars and their detection via atomic physics". In: *Commun. Phys.* 3.1 (2020), pp. 1–8. DOI: 10.1038/s42005-019-0260-3 (cit. on p. 23).

[92] Y. Tsai, J. Eby, and M. S. Safronova. "Direct Detection of Ultralight Dark Matter bound to the Sun with Space Quantum Sensors". In: *Nat. Astron.* 7 (2023), pp. 113–121. DOI: 10.1038/s41550-022-01833-6 (cit. on pp. 23, 52).

[93] A. Hees, J. Guéna, M. Abgrall, S. Bize, and P. Wolf. "Searching for an Oscillating Massive Scalar Field as a Dark Matter Candidate Using Atomic Hyperfine Frequency Comparisons". In: *Phys. Rev. Lett.* 117.061301 (2016). DOI: 10.1103/PhysRevLett.117.061301 (cit. on pp. 24, 31, 34, 40, 42, 44, 45, 52).

[94] J.W. Foster, N. L. Rodd, and B. R. Safdi. "Revealing the dark matter halo with axion direct detection". In: *Phys. Rev. D* 97.123006 (2018). DOI: 10.1103/PhysRevD.97.123006 (cit. on p. 25).

[95] G. P. Centers et al. "Stochastic fluctuations of bosonic dark matter". In: *Nat. Commun.* 12.7321 (2021). DOI: 10.1038/s41467-021-27632-7 (cit. on pp. 25, 51).

[96] A. Hees, O. Minazzoli, E. Savalle, Y. V. Stadnik, and P. Wolf. "Violation of the equivalence principle from light scalar dark matter". In: *Phys. Rev. D* 98.064051 (2018). DOI: 10.1103/PhysRevD.98.064051 (cit. on p. 26).

[97] M.G. Kozlov and D. Budker. "Comment on Sensitivity Coefficients to Variation of Fundamental Constants". In: *Ann. Phys.* 531.5 (2019), pp. 2018–2020. DOI: 10.1002/andp.201800254 (cit. on pp. 27, 47).

[98] V. V. Flambaum and A. F. Tedesco. “Dependence of nuclear magnetic moments on quark masses and limits on temporal variation of fundamental constants from atomic clock experiments”. In: *Phys. Rev. C - Nucl. Phys.* 73.5 (2006). DOI: 10.1103/PhysRevC.73.055501 (cit. on pp. 28, 47).

[99] V. V. Flambaum, D. B. Leinweber, A. W. Thomas, and R. D. Young. “Limits on variations of the quark masses, QCD scale, and fine structure constant”. In: *Phys. Rev. D - Part. Fields, Gravit. Cosmol.* 69.11 (2004), pp. 1–8. DOI: 10.1103/PhysRevD.69.115006 (cit. on pp. 28, 47).

[100] Y. V. Stadnik and V. V. Flambaum. “Searching for dark matter and variation of fundamental constants with laser and maser interferometry”. In: *Phys. Rev. Lett.* 114.161301 (2015). DOI: 10.1103/PhysRevLett.114.161301 (cit. on p. 28).

[101] A. A. Geraci, C. Bradley, D. Gao, J. Weinstein, and A. Derevianko. “Searching for Ultralight Dark Matter with Optical Cavities”. In: *Phys. Rev. Lett.* 123.31304 (2019). DOI: 10.1103/PhysRevLett.123.031304 (cit. on pp. 28, 47).

[102] H. Kim, A. Lenoci, G. Perez, and W. Ratzinger. “Probing an ultralight QCD axion with electromagnetic quadratic interaction”. In: *Phys. Rev. D* 109.15030 (2024). DOI: 10.1103/PhysRevD.109.015030 (cit. on p. 29).

[103] V. V. Flambaum and I. B. Samsonov. “Fluctuations of atomic energy levels due to axion dark matter”. In: *Phys. Rev. D* 108.75022 (2023). DOI: 10.1103/PhysRevD.108.075022 (cit. on p. 29).

[104] K. Van Tilburg, N. Leefer, L. Bougas, and D. Budker. “Search for Ultralight Scalar Dark Matter with Atomic Spectroscopy”. In: *Phys. Rev. Lett.* 115.011802 (2015). DOI: 10.1103/PhysRevLett.115.011802 (cit. on pp. 31, 34, 40).

[105] J.D. Scargle. “Studies in astronomical time series analysis. II. Statistical aspects of spectral analysis of unevenly spaced data”. In: *Astrophys. J.* 263 (1982), pp. 835–853 (cit. on pp. 31, 33).

[106] J. T. VanderPlas. “Understanding the Lomb–Scargle Periodogram”. In: *Astrophys. J. Suppl. Ser.* 236.16 (2018), 28pp. DOI: 10.3847/1538-4365/aab766 (cit. on p. 31).

[107] J.T. Vanderplas and Ž. Ivezić. “Periodograms for multiband astronomical time series”. In: *Astrophys. J.* 812.18 (2015), 15pp. DOI: 10.1088/0004-637X/812/1/18 (cit. on p. 31).

https://doi.org/10.7795/110.20260227

[108] A. Hees, J. Guéna, M. Abgrall, S. Bize, and P. Wolf. "Searching for an oscillating massive scalar field as a dark matter candidate using atomic hyperfine frequency comparisons – Supplemental material". In: *Phys. Rev. Lett.* 117.061301 (2016) (cit. on p. 33).

[109] C. J. Kennedy, E. Oelker, J. M. Robinson, T. Bothwell, D. Kedar, W. R. Milner, G. E. Marti, A. Derevianko, and J. Ye. "Precision Metrology Meets Cosmology: Improved Constraints on Ultralight Dark Matter from Atom-Cavity Frequency Comparisons". In: *Phys. Rev. Lett.* 125 (2020), p. 201302. DOI: 10.1103/PhysRevLett.125.201302 (cit. on pp. 34, 40, 42, 44, 45, 51, 52, 54, 126).

[110] R. Schwarz. "A cryogenic Strontium lattice clock". PhD thesis. Universität Hannover, 2022 (cit. on p. 35).

[111] E. Gross and O. Vitells. "Trial factors for the look elsewhere effect in high energy physics". In: *Eur. Phys. J. C* 70.1 (2010), pp. 525–530. DOI: 10.1140/epjc/s10052-010-1470-8 (cit. on p. 37).

[112] G. Cowan, K. Cranmer, E. Gross, and O. Vitells. "Asymptotic formulae for likelihood-based tests of new physics". In: *Eur. Phys. J. C* 71.1554 (2011). DOI: 10.1140/epjc/s10052-011-1554-0Special (cit. on p. 37).

[113] F. Beaujean, A. Caldwell, and O. Reimann. "Is the bump significant? An axion-search example". In: *Eur. Phys. J. C* 78.793 (2018). DOI: 10.1140/epjc/s10052-018-6217-y (cit. on p. 37).

[114] J. Bergé, P. Brax, G. Métris, M. Pernot-Borràs, P. Touboul, and J. P. Uzan. "MICROSCOPE Mission: First Constraints on the Violation of the Weak Equivalence Principle by a Light Scalar Dilaton". In: *Phys. Rev. Lett.* 120.14 (2018), pp. 1–6. DOI: 10.1103/PhysRevLett.120.141101 (cit. on pp. 40, 45, 51).

[115] P. Touboul et al. "MICROSCOPE Mission: Final Results of the Test of the Equivalence Principle". In: *Phys. Rev. Lett.* 129.121102 (2022). DOI: 10.1088/1361-6382/ab4707 (cit. on pp. 40, 45, 51).

[116] K. Beloy et al. "Frequency ratio measurements at 18-digit accuracy using an optical clock network". In: *Nature* 591.7851 (2021), pp. 564–569. DOI: 10.1038/s41586-021-03253-4 (cit. on p. 40).

[117] T. Kobayashi et al. “Search for Ultralight Dark Matter from Long-Term Frequency Comparisons of Optical and Microwave Atomic Clocks”. In: *Phys. Rev. Lett.* 129.241301 (2022). DOI: 10.1103/PhysRevLett.129.241301 (cit. on pp. 40, 42, 44, 45, 50–52).

[118] V. V. Flambaum. “Enhanced effect of temporal variation of the fine structure constant and the strong interaction in ^{229}Th”. In: *Phys. Rev. Lett.* 97.092502 (2006). DOI: 10.1103/PhysRevLett.97.092502 (cit. on pp. 41, 54).

[119] E. Peik, T. Schumm, M. S. Safronova, A. Pálffy, J. Weitenberg, and P. G. Thirolf. “Nuclear clocks for testing fundamental physics”. In: *Quantum Sci. Technol.* 6.034002 (2021). DOI: 10.1088/2058-9565/abe9c2 (cit. on pp. 41, 54).

[120] J. C. Berengut, V. A. Dzuba, and V. V. Flambaum. “Enhanced laboratory sensitivity to variation of the fine-structure constant using highly charged ions”. In: *Phys. Rev. Lett.* 105.120801 (2010). DOI: 10.1103/PhysRevLett.105.120801 (cit. on pp. 41, 54).

[121] M. S. Safronova, V. A. Dzuba, V. V. Flambaum, U. I. Safronova, S. G. Porsev, and M. G. Kozlov. “Highly charged ions for atomic clocks, quantum information, and search for α variation”. In: *Phys. Rev. Lett.* 113.030801 (2014). DOI: 10.1103/PhysRevLett.113.030801 (cit. on pp. 41, 54).

[122] X. Zhang, A. Banerjee, M. Leyser, G. Perez, S. Schiller, D. Budker, and D. Antypas. “Search for Ultralight Dark Matter with Spectroscopy of Radio-Frequency Atomic Transitions”. In: *Phys. Rev. Lett.* 130.251002 (2023). DOI: 10.1103/physrevlett.130.251002 (cit. on pp. 42, 50–52).

[123] R. Oswald et al. “Search for Dark-Matter-Induced Oscillations of Fundamental Constants Using Molecular Spectroscopy”. In: *Phys. Rev. Lett.* 129.31302 (2022). DOI: 10.1103/PhysRevLett.129.031302 (cit. on p. 42).

[124] F. Gebert, Y. Wan, F. Wolf, C. N. Angstmann, J. C. Berengut, and P. O. Schmidt. “Precision Isotope Shift Measurements in Calcium Ions Using Quantum Logic Detection Schemes”. In: *Phys. Rev. Lett.* 115.053003 (2015). DOI: 10.1103/PhysRevLett.115.053003 (cit. on p. 42).

[125] C. Solaro, S. Meyer, K. Fisher, J. C. Berengut, E. Fuchs, and M. Drewsen. “Improved isotope-shift-based bounds on bosons beyond the standard model through measurements of the $^2D_{3/2} - {}^2D_{5/2}$ interval in Ca^+”. In: *Phys. Rev. Lett.* 125.123003 (2020). DOI: 10.1103/PhysRevLett.125.123003 (cit. on p. 42).

https://doi.org/10.7795/110.20260227

[126] I. Counts, J. Hur, D.P.L. Aude Craik, H. Jeon, C. Leung, J. C. Berengut, A. Geddes, A. Kawasaki, W. Jhe, and V. Vuletić. "Evidence for nonlinear isotope shift in Yb^+ search for new boson". In: *Phys. Rev. Lett.* 125.123002 (2020). DOI: 10.1103/PhysRevLett.125.123002 (cit. on p. 42).

[127] J. Hur et al. "Evidence of Two-Source King Plot Nonlinearity in Spectroscopic Search for New Boson". In: *Phys. Rev. Lett.* 128.163201 (2022). DOI: 10.1103/PhysRevLett.128.163201 (cit. on p. 42).

[128] A. Kawasaki, T. Kobayashi, A. Nishiyama, T. Tanabe, and M. Yasuda. "Isotope-shift analysis with the $4f^{14}6s^2\,{}^1S_0 - 4f^{13}5d6s^2(J=2)$ transition in ytterbium". In: *Phys. Rev. A* 109.062806 (2024). DOI: 10.1103/PhysRevA.109.062806 (cit. on p. 42).

[129] A. Banerjee, D. Budker, M. Filzinger, N. Huntemann, G. Paz, G. Perez, S. Porsev, and M. Safronova. *Oscillating nuclear charge radii as sensors for ultralight dark matter*. 2023. arXiv: 2301.10784 (cit. on p. 42).

[130] W.H. King. *Isotope Shifts in Atomic Spectra*. Physics of Atoms and Molecules. Springer US, 2013. ISBN: 9781489917867. DOI: 10.1007/978-1-4899-1786-7 (cit. on p. 43).

[131] I. Angeli and K.P. Marinova. "Table of experimental nuclear ground state charge radii: An update". In: *Atomic Data and Nuclear Data Tables* 99.1 (2013), pp. 69–95. DOI: 10.1016/j.adt.2011.12.006 (cit. on p. 43).

[132] J. L. Friar and J. W. Negele. "Theoretical and Experimental Determination of Nuclear Charge Distributions". In: *Advances in Nuclear Physics: Volume 8*. Ed. by M. Baranger and E. Vogt. Boston, MA: Springer US, 1975, pp. 219–376. ISBN: 978-1-4757-4398-2. DOI: 10.1007/978-1-4757-4398-2_3 (cit. on p. 44).

[133] J. Simonis, S. R. Stroberg, K. Hebeler, J. D. Holt, and A. Schwenk. "Saturation with chiral interactions and consequences for finite nuclei". In: *Phys. Rev. C* 96.014303 (2017). DOI: 10.1103/PhysRevC.96.014303 (cit. on p. 44).

[134] L. Ubaldi. "Effects of theta on the deuteron binding energy and the triple-alpha process". In: *Phys. Rev. D* 81.025011 (2010). DOI: 10.1103/PhysRevD.81.025011 (cit. on p. 44).

[135] E. Fischbach and C. Talmadge. "Ten years of the fifth force". In: *31st Rencontres de Moriond: Dark Matter and Cosmology, Quantum Measurements and Experimental Gravitation*. 1996, pp. 443–451. DOI: 10.48550/arXiv.hep-ph/9606249 (cit. on p. 45).

[136] V. V. Flambaum and A. J. Mansour. "Variation of the quadrupole hyperfine structure and nuclear radius due to an interaction with scalar and axion dark matter". In: *Phys. Rev. Lett.* 131.113004 (2023). DOI: 10.1103/PhysRevLett.131.113004 (cit. on pp. 44, 46).

[137] J. Guéna, M. Abgrall, D. Rovera, P. Rosenbusch, M. E. Tobar, Ph Laurent, A. Clairon, and S. Bize. "Improved tests of local position invariance using ^{87}Rb and ^{133}Cs fountains". In: *Phys. Rev. Lett.* 109.080801 (2012). DOI: 10.1103/PhysRevLett.109.080801 (cit. on p. 46).

[138] E. Savalle, A. Hees, F. Frank, E. Cantin, P. E. Pottie, B. M. Roberts, L. Cros, B. T. McAllister, and P. Wolf. "Searching for Dark Matter with an Optical Cavity and an Unequal-Delay Interferometer". In: *Phys. Rev. Lett.* 126.051301 (2021). DOI: 10.1103/PhysRevLett.126.051301 (cit. on pp. 47, 49).

[139] D. Antypas, D. Budker, V. Flambaum, M.G. Kozlov, G. Perez, and J. Ye. "Fast Apparent Oscillations of Fundamental Constants". In: *Ann. Phys.* 532.4 (2020). DOI: 10.1002/andp.201900566 (cit. on p. 47).

[140] O. Lopez, A. Haboucha, B. CHanteau, C. Chardonnet, A. Amy-Klein, and G. Santarelli. "Ultra-stable long distance optical frequency distribution using the internet network". In: *Opt. Express* 20.21 (2012), p. 23519. DOI: 10.1364/fio.2013.fth3b.1 (cit. on p. 48).

[141] S. M.F. Raupach, A. Koczwara, and G. Grosche. "Brillouin amplification supports 1×10^{-20} uncertainty in optical frequency transfer over 1400 km of underground fiber". In: *Phys. Rev. A* 92.021801(R) (2015). DOI: 10.1103/PhysRevA.92.021801 (cit. on p. 48).

[142] N. Chiodo, N. Quintin, F. Stefani, F. Wiotte, E. Camisard, C. Chardonnet, G. Santarelli, A. Amy-Klein, P.-E. Pottie, and O. Lopez. "Cascaded optical fiber link using the internet network for remote clocks comparison". In: *Opt. Express* 23.26 (2015), p. 33927. DOI: 10.1364/oe.23.033927 (cit. on p. 48).

[143] C. Lisdat et al. "A clock network for geodesy and fundamental science". In: *Nat. Commun.* 7 (2016), pp. 1–7. DOI: 10.1038/ncomms12443 (cit. on p. 48).

[144] S. Koke, A. Kuhl, T. Waterholter, S. M.F. Raupach, O. Lopez, E. Cantin, N. Quintin, A. Amy-Klein, P.E. Pottie, and G. Grosche. "Combining fiber Brillouin amplification with a repeater laser station for fiber-based optical frequency dissemination over 1400 km". In: *New J. Phys.* 21.12 (2019), pp. 0–11. DOI: 10.1088/1367-2630/ab5d95 (cit. on p. 48).

https://doi.org/10.7795/110.20260227

[145] C. Clivati et al. “Coherent Optical-Fiber Link Across Italy and France”. In: *Phys. Rev. Appl.* 18.5 (2022), p. 1. DOI: 10.1103/PhysRevApplied.18.054009 (cit. on p. 48).

[146] M. Schioppo et al. “Comparing ultrastable lasers at 7×10^{-17} fractional frequency instability through a 2220 km optical fibre network”. In: *Nat. Commun.* 13.1 (2022), pp. 1–11. DOI: 10.1038/s41467-021-27884-3 (cit. on pp. 48, 49).

[147] P. Delva et al. “Test of Special Relativity Using a Fiber Network of Optical Clocks”. In: *Phys. Rev. Lett.* 118.221102 (2017). DOI: 10.1103/PhysRevLett.118.221102 (cit. on p. 48).

[148] B. M. Roberts et al. “Search for transient variations of the fine structure constant and dark matter using fiber-linked optical atomic clocks”. In: *New J. Phys.* 22.9 (2020). DOI: 10.1088/1367-2630/abaace (cit. on p. 48).

[149] M. Schioppo et al. *Data for “Comparing ultrastable lasers at 7×10^{-17} fractional frequency instability through a 2220 km optical fibre network” [zenodo.org/record/5717953]*. 2021. DOI: 10.5281/ZENODO.5717953. (Visited on 11/20/2023) (cit. on pp. 48–50).

[150] M. Hirsch. *Pymap3d: 3D Coordinate Conversions for Geospace, 10.5281/zenodo.213676*. 2016. DOI: 10.5281/zenodo.213676 (cit. on p. 49).

[151] B. M. Roberts, A. R. Caddell, and M. Filzinger. *GPS analysis*. 2024. URL: https://github.com/benroberts999/gps-analysis (cit. on pp. 49, 52).

[152] K. Beloy et al. “Frequency ratio measurements at 18-digit accuracy using an optical clock network”. In: *Nature* 591.7851 (2021), pp. 564–569. DOI: 10.1038/s41586-021-03253-4 (cit. on pp. 50, 52).

[153] N. Sherrill et al. “Analysis of atomic-clock data to constrain variations of fundamental constants”. In: *New J. Phys.* 25.093012 (2023) (cit. on pp. 50, 52).

[154] W. M. Campbell, B.T. McAllister, M. Goryachev, E. N. Ivanov, and M. E. Tobar. “Searching for Scalar Dark Matter via Coupling to Fundamental Constants with Photonic, Atomic, and Mechanical Oscillators”. In: *Phys. Rev. Lett.* 126.71301 (2021). DOI: 10.1103/PhysRevLett.126.071301 (cit. on pp. 51, 52).

[155] B. M. Roberts, G. Blewitt, C. Dailey, M. Murphy, M. Pospelov, Alex Rollings, J. Sherman, W. Williams, and A. Derevianko. "Search for domain wall dark matter with atomic clocks on board global positioning system satellites". In: *Nat. Commun.* 8.1195 (2017). DOI: 10.1038/s41467-017-01440-4 (cit. on p. 51).

[156] Y. Li, R. Liu, C. Dailey, and N. Afshordi. "Detecting cosmological scalar fields using orbital networks of quantum sensors". In: *Phys. Rev. D* 110.043028 (2024). DOI: 10.1103/PhysRevD.110.043028 (cit. on p. 51).

[157] D. Murphy et al. *JPL Analysis Center Technical Report 2015 (in IGS Technical Report 2015)*. 2015 (cit. on p. 51).

[158] Jet Propulsion Laboratory. *https://sideshow.jpl.nasa.gov/pub/jpligsac/* (cit. on p. 51).

[159] G. Blewitt. *GPS and Space-Based Geodetic Methods*. Oxford: Elsevier, 2015, pp. 307–338. DOI: 10.1016/B978-0-444-53802-4.00060-9 (cit. on p. 52).

[160] P. Delva, A. Hees, and P. Wolf. "Clocks in Space for Tests of Fundamental Physics". In: *Space Sci. Rev.* 212.3-4 (2017), pp. 1385–1421. DOI: 10.1007/s11214-017-0361-9 (cit. on p. 52).

[161] Y. A. El-Neaj et al. "AEDGE: Atomic Experiment for Dark Matter and Gravity Exploration in Space". In: *EPJ Quantum Technol.* 7.1 (2020). DOI: 10.1140/epjqt/s40507-020-0080-0 (cit. on p. 52).

[162] A. Derevianko, K. Gibble, L. Hollberg, N. R. Newbury, C. Oates, M. S. Safronova, L. C. Sinclair, and N. Yu. "Fundamental physics with a state-of-the-art optical clock in space". In: *Quantum Sci. Technol.* 7.044002 (2022). DOI: 10.1088/2058-9565/ac7df9 (cit. on p. 52).

[163] V. Schkolnik et al. "Optical atomic clock aboard an Earth-orbiting space station (OACESS): enhancing searches for physics beyond the standard model in space". In: *Quantum Sci. Technol.* 8.1 (2023). DOI: 10.1088/2058-9565/ac9f2b (cit. on p. 52).

[164] K. Beeks et al. *Fine-structure constant sensitivity of the Th-229 nuclear clock transition*. 2024. arXiv: 2407.17300 (cit. on p. 54).

[165] E. Fuchs, F. Kirk, E. Madge, C. Paranjape, E. Peik, G. Perez, W. Ratzinger, and J. Tiedau. "Searching for Dark Matter with the Th 229 Nuclear Lineshape from Laser Spectroscopy". In: *Phys. Rev. X* 15.021055 (2025). DOI: 10.1103/PhysRevX.15.021055 (cit. on p. 54).

https://doi.org/10.7795/110.20260227

[166] S. Aharony, N. Akerman, R. Ozeri, G. Perez, I. Savoray, and R. Shaniv. "Constraining rapidly oscillating scalar dark matter using dynamic decoupling". In: *Phys. Rev. D* 103.75017 (2021). DOI: 10.1103/PhysRevD.103.075017 (cit. on p. 54).

[167] M. H. Zaheer, N. J. Matjelo, D. B. Hume, M. S. Safronova, and D. R. Leibrandt. "Quantum metrology algorithms for dark matter searches with clocks". In: *Phys. Rev. A* 111.012601 (2025). DOI: 10.1103/PhysRevA.111.012601 (cit. on pp. 54, 126).

[168] P. Dubé, A. A. Madej, M. Tibbo, and J. E. Bernard. "High-Accuracy Measurement of the Differential Scalar Polarizability of a $^{88}Sr^{+}$ Clock Using the Time-Dilation Effect". In: *Phys. Rev. Lett.* 112.173002 (2014). DOI: 10.1103/PhysRevLett.112.173002 (cit. on pp. 57, 86, 106, 107, 110).

[169] T. Lindvall, K. J. Hanhijärvi, T. Fordell, and A. E. Wallin. "Measurement of the Differential Static Scalar Polarizability of the $^{88}Sr^{+}$ Clock Transition". In: *Phys. Rev. Lett.* 135.043402 (2025). DOI: 10.1103/52by-28mr (cit. on pp. 57, 106, 110).

[170] P. Dubé, A. A. Madej, A. Shiner, and B. Jian. "$^{88}Sr^{+}$ single-ion optical clock with a stability approaching the quantum projection noise limit". In: *Phys. Rev. A* 92.042119 (2015). DOI: 10.1103/PhysRevA.92.042119 (cit. on pp. 58, 87).

[171] V. Letchumanan, M. A. Wilson, P. Gill, and A. G. Sinclair. "Lifetime measurement of the metastable state in using a single trapped ion". In: *Phys. Rev. A* 72.012509 (2005). DOI: 10.1103/PhysRevA.72.012509 (cit. on pp. 59, 90).

[172] A. M. Hankin, E. R. Clements, Y. Huang, S. M. Brewer, J. S. Chen, C. W. Chou, D. B. Hume, and D. R. Leibrandt. "Systematic uncertainty due to background-gas collisions in trapped-ion optical clocks". In: *Phys. Rev. A* 100.33419 (2019). DOI: 10.1103/PhysRevA.100.033419 (cit. on pp. 62, 111).

[173] H. Fürst. "Trapped ions in a bath of ultracold atoms". PhD Thesis. University of Amsterdam, 2019 (cit. on p. 62).

[174] J. Keller, T. Burgermeister, D. Kalincev, A. Didier, A. P. Kulosa, T. Nordmann, J. Kiethe, and T. E. Mehlstäubler. "Controlling systematic frequency uncertainties at the 10-19 level in linear Coulomb crystals". In: *Phys. Rev. A* 99.013405 (2019). DOI: 10.1103/PhysRevA.99.013405 (cit. on pp. 63, 76, 79, 100).

[175] T. Burgermeister. “Development and characterization of a linear ion trap for an improved optical clock performance”. PhD Thesis. Universität Hannover, 2019 (cit. on pp. 63, 76, 108).

[176] D. R. Leibrandt, R. J. Clark, J. Labaziewicz, P. Antohi, W. Bakr, K. R. Brown, and I. L. Chuang. “Laser ablation loading of a surface-electrode ion trap”. In: *Phys. Rev. A* 76.055403 (2007). DOI: 10.1103/PhysRevA.76.055403 (cit. on p. 64).

[177] D Szwer. “High Fidelity Readout and Protection of a $^{43}Ca^{+}$ Trapped Ion Qubit”. PhD Thesis. Oxford, 2009 (cit. on p. 72).

[178] P. Dubé, A.A. Madej, J.E. Bernard, G. Humphrey, M. Vainio, J. Jiang, and D.J. Jones. “Recent progress on the NRC $^{88}Sr^{+}$ single-ion optical frequency standard”. In: *2010 IEEE Int. Freq. Control Symp.* (2010), pp. 65–70. DOI: 10.1109/FREQ.2010.5556371 (cit. on p. 72).

[179] M. Abdel-Hafiz et al. *Guidelines for developing optical clocks with* 10^{-18} *fractional frequency uncertainty*. 2019. DOI: 10.15488/5553. arXiv: 1906.11495 (cit. on p. 75).

[180] N. Herschbach, K. Pyka, J. Kelle, and T. E. Mehlstäubler. “Linear Paul trap design for an optical clock with Coulomb crystals”. In: *Appl. Phys. B Lasers Opt.* 107.4 (2012), pp. 891–906. DOI: 10.1007/s00340-011-4790-y (cit. on p. 76).

[181] K. Pyka, N. Herschbach, J. Keller, and T. E. Mehlstäubler. “A high-precision segmented Paul trap with minimized micromotion for an optical multiple-ion clock”. In: *Appl. Phys. B Lasers Opt.* 114.1-2 (2014), pp. 231–241. DOI: 10.1007/s00340-013-5580-5 (cit. on p. 76).

[182] T. Nordmann, A. Didier, M. Doležal, P. Balling, T. Burgermeister, and T . E. Mehlstäubler. “Sub-kelvin temperature management in ion traps for optical clocks”. In: *Rev. Sci. Instrum.* 91.111301 (2020). DOI: 10.1063/5.0024693 (cit. on pp. 76, 83, 85).

[183] K. Pyka. “High-precision ion trap for spectroscopy of Coulomb crystals”. PhD Thesis. Hannover University, 2013 (cit. on p. 76).

[184] T. Nordmann. “Setup and operation of a multi-ion clock based on linear In^{+} /Yb^{+} crystals”. PhD Thesis. Hannover University, 2023 (cit. on pp. 76, 79, 92).

[185] T. Lindvall, K. J. Hanhijärvi, T. Fordell, and A. E. Wallin. "High-accuracy determination of Paul-trap stability parameters for electric-quadrupole-shift prediction". In: *J. Appl. Phys.* 132.12 (2022). DOI: 10.1063/5.0106633 (cit. on p. 77).

[186] J. Keller, H. L. Partner, T. Burgermeister, and T. E. Mehlstäubler. "Precise determination of micromotion for trapped-ion optical clocks". In: *J. Appl. Phys.* 118.10 (2015). DOI: 10.1063/1.4930037 (cit. on pp. 77, 110).

[187] Q. A. Turchette et al. "Heating of trapped ions from the quantum ground state". In: *Phys. Rev. A* 61.6 (2000), p. 8. DOI: 10.1103/PhysRevA.61.063418 (cit. on p. 78).

[188] J. Keller. "Spectroscopic characterization of ion motion for an optical clock based on Coulomb crystals". PhD Thesis. Universität Hannover, 2015 (cit. on p. 79).

[189] Z. Meir, T. Sikorsky, R. Ben-shlomi, N. Akerman, M. Pinkas, Y. Dallal, and R. Ozeri. "Experimental apparatus for overlapping a ground-state cooled ion with ultracold atoms". In: *J. Mod. Opt.* 65.5-6 (2018), pp. 501–519. DOI: 10.1080/09500340.2017.1397217 (cit. on p. 79).

[190] H. C. J. Gan, G. Maslennikov, K. W. Tseng, T. R. Tan, R. Kaewuam, K. J. Arnold, D. Matsukevich, and M. D. Barrett. "Oscillating-magnetic-field effects in high-precision metrology". In: *Phys. Rev. A* 98.032514 (2018). DOI: 10.1103/PhysRevA.98.032514 (cit. on pp. 79, 82).

[191] M. K. Joshi, M. Guevara-Bertsch, F. Kranzl, R. Blatt, and C. F. Roos. "Characterization of ion-trap-induced ac magnetic fields". In: *Phys. Rev. A* 110.063101 (2024). DOI: 10.1103/PhysRevA.110.063101 (cit. on p. 79).

[192] K. G. Johnson, J. D. Wong-Campos, A. Restelli, K. A. Landsman, B. Neyenhuis, J. Mizrahi, and C. Monroe. "Active stabilization of ion trap radiofrequency potentials". In: *Rev. Sci. Instrum.* 87.5 (2016). DOI: 10.1063/1.4948734 (cit. on p. 81).

[193] C. F. A. Baynham et al. *Measurement of differential polarizabilities at a mid-infrared wavelength in* $^{171}Yb^{+}$. 2018. arXiv: 1801.10134 (cit. on p. 86).

[194] P. Dubé, A. A. Madej, Z. Zhou, and J. E. Bernard. "Evaluation of systematic shifts of the $^{88}Sr^{+}$ single-ion optical frequency standard at the 10^{-17} level". In: *Phys. Rev. A* 87.023806 (2013). DOI: 10.1103/PhysRevA.87.023806 (cit. on pp. 90, 105, 110, 112).

[195] D. F.V. James. “Quantum dynamics of cold trapped ions with application to quantum computation”. In: *Appl. Phys. B Lasers Opt.* 66.2 (1998), pp. 181–190. DOI: 10.1007/s003400050373 (cit. on pp. 91, 101).

[196] G. Morigi and H. Walther. “Two-species Coulomb chains for quantum information”. In: *Eur. Phys. J. D* 13.2 (2001), pp. 261–269. DOI: 10.1007/s100530170275 (cit. on p. 91).

[197] C. Roos. “Controlling the quantum state of trapped ions”. PhD Thesis. Innsbruck University, 2000, p. 145 (cit. on pp. 92, 93, 108).

[198] U. Poschinger, A. Walther, M. Hettrich, F. Ziesel, and F. Schmidt-Kaler. “Interaction of a laser with a qubit in thermal motion and its application to robust and efficient readout”. In: *Appl. Phys. B Lasers Opt.* 107.4 (2012), pp. 1159–1165. DOI: 10.1007/s00340-012-4882-3 (cit. on p. 93).

[199] Daniel Adam Steck. *Quantum and Atom Optics*. Oregon, 2007 (cit. on p. 98).

[200] G. P. Barwood, H. S. Margolis, G. Huang, P. Gill, and H. A. Klein. “Measurement of the electric quadrupole moment of the $4d^2D_{5/2}$ level in $^{88}Sr^+$”. In: *Phys. Rev. Lett.* 93.133001 (2004). DOI: 10.1103/PhysRevLett.93.133001 (cit. on p. 99).

[201] K. Beloy, D. R. Leibrandt, and W. M. Itano. “Hyperfine-mediated electric quadrupole shifts in Al^+ and In^+ ion clocks”. In: *Phys. Rev. A* 95.043405 (2017). DOI: 10.1103/PhysRevA.95.043405 (cit. on p. 100).

[202] N. Aharon, N. Spethmann, I. D. Leroux, P. O. Schmidt, and A. Retzker. “Robust optical clock transitions in trapped ions using dynamical decoupling”. In: *New J. Phys.* 21.083040 (2019). DOI: 10.1088/1367-2630/ab3871 (cit. on p. 100).

[203] V. Devanathan. *Angular Momentum Techniques in Quantum Mechanics*. Dordrecht, Boston, London: Springer Dordrecht, 2002. DOI: 10.1007/0-306-47123-X (cit. on p. 101).

[204] Dansha Jiang, Bindiya Arora, M. S. Safronova, and Charles W. Clark. “Blackbody-radiation shift in a $^{88}Sr^+$ ion optical frequency standard”. In: *J. Phys. B At. Mol. Opt. Phys.* 42.15 (2009). DOI: 10.1088/0953-4075/42/15/154020 (cit. on p. 106).

[205] T. Rosenband et al. “Frequency Ratio of Al^+ and Hg^+ Single-Ion Optical Clocks; Metrology at the 17th Decimal Place”. In: *Science (80-.).* 319 (2008), pp. 1808–1812 (cit. on p. 111).

https://doi.org/10.7795/110.20260227

[206] Wayne M Itano, L L Lewis, and D J Wineland. "Shift of S∼/2 hyperfine splittinas due to blackbody radiation". In: *Phys. Rev. A* 25.2 (1982), pp. 1233–1235 (cit. on p. 113).

[207] Z. M. Tang, Y. F. Wei, B. K. Sahoo, C. B. Li, Y. Yang, Y- Zou, and X. R. Huang. "Blackbody-radiation Zeeman shifts in optical clocks: The role of fine-structure intramanifold resonances". In: *Phys. Rev. A* 110.043108 (2024). DOI: 10.1103/PhysRevA.110.043108 (cit. on p. 113).

[208] A. A. Madej, J. E. Bernard, P. Dubé, L. Marmet, and R. S. Windeler. "Absolute frequency of the 88 Sr+ 5s 2S1/2-4d 2D5/2 reference transition at 445 THz and evaluation of systematic shifts". In: *Phys. Rev. A* 70.1 (2004), pp. 11–14. DOI: 10.1103/PhysRevA.70.012507 (cit. on p. 113).

[209] T. Lindvall, A. E. Wallin, K. J. Hanhijärvi, and T. Fordell. "Noise-induced servo errors in optical clocks utilizing Rabi interrogation". In: *Metrologia* 60.045008 (2023). DOI: 10.1088/1681-7575/acdfd4 (cit. on p. 115).

[210] T. Lindvall, A. E. Wallin, K. J. Hanhijärvi, and T. Fordell. "Noise-induced servo errors in optical clocks utilizing Rabi interrogation". In: *Metrologia* 60.045008 (2023). DOI: 10.1088/1681-7575/acdfd4 (cit. on p. 115).

[211] M. Kazda, V. Gerginov, N. Huntemann, B. Lipphardt, and S. Weyers. "Phase analysis for frequency standards in the microwave and optical domains". In: *IEEE Trans. Ultrason. Ferroelectr. Freq. Control* 63.7 (2016), pp. 970–974. DOI: 10.1109/TUFFC.2016.2515759 (cit. on pp. 115, 116).

[212] A. W. Young, W. J. Eckner, W. R. Milner, D. Kedar, M. A. Norcia, E. Oelker, N. Schine, J. Ye, and A. M. Kaufman. "Half-minute-scale atomic coherence and high relative stability in a tweezer clock". In: *Nature* 588.7838 (2020), pp. 408–413. DOI: 10.1038/s41586-020-3009-y (cit. on p. 118).

[213] T. Bothwell, C. J. Kennedy, A. Aeppli, D. Kedar, J. M. Robinson, E. Oelker, A. Staron, and J. Ye. "Resolving the gravitational redshift across a millimetre-scale atomic sample". In: *Nature* 602.7897 (2022), pp. 420–424. DOI: 10.1038/s41586-021-04349-7 (cit. on p. 118).

[214] Xi. Zheng, J. Dolde, M. C. Cambria, H.M. Lim, and S. Kolkowitz. "A lab-based test of the gravitational redshift with a miniature clock network". In: *Nat. Commun.* 14.4886 (2023). DOI: 10.1038/s41467-023-40629-8 (cit. on p. 118).

https://doi.org/10.7795/110.20260227

[215] S. Aharony, N. Akerman, R. Ozeri, G. Perez, I. Savoray, and R. Shaniv. "Constraining rapidly oscillating scalar dark matter using dynamic decoupling". In: *Phys. Rev. D* 103.7 (2021), pp. 1–11. DOI: 10.1103/PhysRevD.103.075017 (cit. on p. 126).

https://doi.org/10.7795/110.20260227

https://doi.org/10.7795/110.20260227

Acknowledgements

Spending my days in the clock hall working on the $^{171}Yb^{+}$ (and $^{88}Sr^{+}$!) ion clocks for the past 4.5 years has been a privilege and a pleasure. I have received incredible support during my PhD, and none of the things I have written about in this thesis would have been possible without the collaborative effort of many people.

Every beginning PhD student needs someone they can follow around and learn from all day. I was exceptionally lucky that this person for me was Richard Lange. He was not only extremely knowledgeable and dedicated, but also patient enough to deal with my many questions and the mess that seems to follow me in the lab. Learning about the $^{171}Yb^{+}$ single-ion clocks from you has been invaluable – thank you so much!

Martin Steinel is the $^{88}Sr^{+}$ guy in our group, since he did much of the work in getting us started with this species as a clock ion. Having him as a partner in crime in getting the new experiment running has sped up things considerably, in particular because he is an amazing programmer and I am, well, not. It has also been great to have another PhD student around that started at a similar time and shared similar types of frustrations over the years. Thank you for never being too busy to help me find a bug in my code!

Many of the mechanical components making up the new experiment would not exist without Martin Menzel. Discussing with him has always improved my designs, and somehow nothing was impossible for him. He has substantially contributed to the success of the experiment countless times, for example by developing an apparatus for aligning the trap wafers with micron precision. Vielen Dank für deine Unterstützung – ohne dich würde das Experiment heute noch nicht stehen!

The fact that our lab has no electronics labeled “broken” is largely thanks to Andreas Hoppmann, who can repair absolutely anything and has also built many of the electronic components used in the new experiment. Vielen herzlichen Dank

https://doi.org/10.7795/110.20260227

dass du dir immer wieder die Zeit genommen hast um kurzfristig Komponenten zu modifizieren oder zu reparieren!

Most people will unfortunately never know the pleasure of sharing a lab with a talented physics technician such as Nele Wendt! She has planned, set up, and aligned many of the optical breadboards that are now in use at the various experiments. During the time she spent with us, she has also made sure that the lab didn't sink into chaos, and from time to time reminded me that there is a life outside of the clock hall. Nele Wendt – vielen Dank.

Working in the clock hall with Jian Jang and Saaswath JK during the past years has been a pleasure, thank you both for your help and collaboration on the countless things that come up during a day in the lab! Jian, thank you so much for your help with Zemax for designing the imaging system.

This manuscript has benefited from the helpful comments and suggestions of our newest group member Will Eckner – thank you!

I'd also like to thank Marc Schiffer for helpful comments on this thesis!

Mikkel Rasmussen was a curious and talented intern who helped simulate, design, and test the magnetic field coils for the new experiment. Thank you for your enthusiasm and great work.

I am very grateful to Tanja Mehlstäbler's group, in particular Daniel Bennett, for sharing their extensive experience on how to build an ion trap. I am also indebted to the members of the scientific instrumentation department, who have not only manufactured the trap wafers and spacers, but have time and time again generously shared their expertise and taken the time to support my efforts. Mein besonderer Dank gilt Carsten Feist und Daniel Albrecht, die mit mir stundenlang Fallenchips unter dem Mikroskop begutachtet haben, und denen kein Detail entgangen ist und kein Kratzer zu unwichtig war.

Optical frequency comparisons depend on frequency combs. Burghard Lipphardt and Erik Benkler go above and beyond in making sure these measurements are possible every single day in the clock hall and across the PTB campus. Their work has been absolutely crucial for the results discussed here. Vielen Dank!

Our measurements benefitted immensely from the laser instability that was obtained via referencing to the ultrastable silicon cavities. Huge thanks to the team around Uwe Sterr for making this possible.

https://doi.org/10.7795/110.20260227

Any clock is only as good as the clocks it can be compared to. Luckily, there are many great optical clock experiments at PTB. I'd like to thank the highly charged ions team, the Sr lattice clock team, and the In^+ Coulomb crystal clock team for their frequent and fruitful collaboration.

Building a new experiment involves buying many, many components. I'd like to thank Martina Bäumler for making this process incredibly seamless and helping me navigate the associated bureaucracy. Herzlichen Dank Frau Bäumler! I'd also like to thank all other members of the time and frequency department for creating such a friendly and productive environment!

Learning about ultralight dark matter from scratch was extremely intimidating at first. However, I quickly discovered that the field is full of smart and kind people who were willing to answer my questions. Huge thanks goes to Abhishek Banherjee, Dima Budger, Gil Paz, Gilad Perez, and Marianna Safronova for the fruitful collaboration on the charge radius project! I'd also like to thank Ashlee Caddell and Ben Roberts for the amazing collaboration on the time delay paper. Working with all of you has been an absolute pleasure and I have learned a lot, thank you! I'd further like to thank Aurelién Hees and Peter Wolf for helpful discussions.

Even though Christian Sanner was no longer part of the $^{171}Yb^+$ team when I joined the group as a PhD student, he has had a lasting positive influence on the atmosphere in the clock hall and has offered many helpful pieces of advice over the years – Danke und ahoi!

Nils Huntemann has been an exceptional mentor. He is not just dedicated to advancing the physics and solving technical problems, but equally to providing the best possible working environment and learning experience to every member of the team. He often believed in my capabilities much more than I did, and guided my efforts in productive directions. Thank you for never being too busy to discuss or come to the lab and get involved in the details of the experiment when needed.

I'd like to thank Ekkehard Peik for the many opportunities and the freedom I have enjoyed as part of the time and frequency department. Thank you for taking me on as a student, and for your ongoing support throughout the years.

Lastly, I'd like to thank Piet Schmidt for his friendly and helpful support as a secondary PhD advisor, and Tracy Northup for generously agreeing to referee this thesis.

https://doi.org/10.7795/110.20260227

https://doi.org/10.7795/110.20260227

Publications

1. M. Filzinger et al.: *A multi-ion optical clock with a* 5×10^{-19} *systematic uncertainty*, manuscript in preparation.

2. J. Jiang, A. V. Viatkina, Saaswath JK, M. Steinel, M. Filzinger, E. Peik, S. G. Porsev, M. S. Safronova, A. Surzyhkov, and N. Huntemann: *High-resolution spectroscopy of* $^{173}Yb^{+}$ *ions*, in press at Phys. Rev. Lett.

3. M. Filzinger, S. Dörscher, R. Lange, J. Klose, M. Steinel, E. Benkler, E. Peik, C. Lisdat, N. Huntemann: *Searching for variations of fundamental constants and ultralight dark matter with optical atomic clocks*, Proc. Des 59th Rencontres de Moriond, Gravitation session, in press (2025).

4. L. J. Spieß, S. Chen, A. Wilzewski, M. Wehrheim, J. Gilles, A. Surzhykov, E. Benkler, M. Filzinger, M. Steinel, N. Huntemann, C. Cheung, S. G. Porsev, A. I. Bondarev, M. S. Safronova, J. R. Crespo López-Urrutia, P. O. Schmidt: *Excited-state magnetic properties of carbon-like* Ca^{14+}, Phys. Rev. Lett. **135**, 043002 (2025).

5. T. Lindvall, M. Pizzocaro, R. M. Godun, M. Abgrall, D. Akamatsu, A. Amy-Klein, E. Benkler, N. M. Bhatt, D. Calonico, E. Cantin et al.: *Coordinated international comparisons between optical clocks connected via fiber and satellite links*, Optica **12**, 6, pp. 843-852 (2025).

6. H. N. Hausser, J. Keller, T. Nordmann, N. M. Bhatt, J. Kiethe, H. Liu, I. M. Richter, M. von Boehn, J. Rahm, S. Weyers, E. Benkler, B. Lipphardt, S. Doerscher, K. Stahl, J. Klose, C. Lisdat, M. Filzinger, N. Huntemann, E. Peik, T. E. Mehlstäubler: *An* $^{115}In^{+}$-$^{172}Yb^{+}$ *Coulomb crystal clock with* 2.5×10^{-18} *systematic uncertainty*, Phys. Rev. Lett. **134**, 023201 (2025).

7. M. Filzinger, A. R. Caddell, D. Jani, M. Steinel, L. Giani, N. Huntemann, B. M. Roberts: *Ultralight dark matter search with space-time separated atomic clocks and cavities*, Phys. Rev. Lett. **134**, 031001 (2025).

https://doi.org/10.7795/110.20260227

8. A. Wilzewski, L. I. Huber, M. Door, J. Richter, A. Mariotti, L. J. Spieß, M. Wehrheim, S. Chen, S. A. King, P. Micke, M. Filzinger, M. R. Steinel, N. Huntemann, E. Benkler, P. O. Schmidt, J. Flannery, R. Matt, M. Stadler, R. Oswald, F. Schmid, D. Kienzler, J. Home, D. P. L. Aude Craik, S. Eliseev, P. Filianin, J. Herkenhoff, K. Kromer, K. Blaum, V. A. Yerokhin, I. A. Valuev, N. S. Oreshkina, C. Lyu, S. Banerjee, C. H. Keitel, Z. Harman, J. C. Berengut, A. Viatkina, J. Gilles, A. Surzhykov, M. K. Rosner, J. R. Crespo López-Urrutia, E. Fuchs: *Nonlinear calcium King plot constrains new bosons and nuclear properties*, Phys. Rev. Lett. **134**, 233002 (2025).

9. M. Door, Ch. Yeh, M. Heinz, F. Kirk, C. Lyu, T. Miyagi, J. C. Berengut, J. Bieroń, K. Blaum, L. S. Dreissen, S. Eliseev, P. Filianin, M. Filzinger, E. Fuchs, H. A. Fürst, G. Gaigalas, Z. Harman, J. Herkenhoff, N. Huntemann, C. H. Keitel, K. Kromer, D. Lange, A. Rischka, C. Schweiger, A. Schwenk, N. Shimizu, T. E. Mehlstäubler: *Search for new bosons with ytterbium isotope shifts*, Phys. Rev. Lett. **134**, 063002 (2025).

10. A. Banerjee, D. Budker, M. Filzinger, N. Huntemann, G. Paz, G. Perez, S. Porsev, M. Safronova: *Oscillating nuclear charge radii as sensors for ultralight dark matter*, Phys. Rev. Lett. **135**, 223001 (2025).

11. M. Filzinger, S. Dörscher, R. Lange, J. Klose, M. Steinel, E. Benkler, E. Peik, C. Lisdat, N. Huntemann: *Improved limits on the coupling of ultralight bosonic dark matter to photons from optical atomic clock comparisons*, Phys. Rev. Lett. **130**, 253001 (2023).

12. M. Steinel, H. Shao, M. Filzinger, B. Lipphardt, M. Brinkmann, A. Didier, T. E. Mehlstäubler, T. Lindvall, E. Peik, N. Huntemann: *Evaluation of a $^{88}Sr^{+}$ optical clock with a direct measurement of the blackbody radiation shift and determination of the clock frequency*, Phys. Rev. Lett. **131**, 083002 (2023).

13. Q. Wu, M. Filzinger, Y. Shi, Z. Wang, J. Zhang: *Adaptively controlled fast production of defect-free beryllium ion crystals using pulsed laser ablation*, Rev. Sci. Instr. **92**, 6 (2021).

https://doi.org/10.7795/110.20260227

Bundesministerium
für Wirtschaft
und Energie

Die Physikalisch-Technische Bundesanstalt, das nationale Metrologieinstitut, ist eine wissenschaftlich-technische Bundesoberbehörde im Geschäftsbereich des Bundesministeriums für Wirtschaft und Energie.

Physikalisch-Technische Bundesanstalt
Nationales Metrologieinstitut
ISNI: 0000 0001 2186 1887

Bundesallee 100
38116 Braunschweig

Presse- und Öffentlichkeitsarbeit

Telefon: (0531) 592-93 21
Fax: (0531) 592-30 08
E-Mail: presse@ptb.de
www.ptb.de